

AD-A234 751

AFOSR-TR. 91 0267

DEVELOPMENT AND VERIFICATION OF A THREE-DIMENSIONAL
LARGE-SCALE CLOUD MODEL

J.L. Lee
K.N. Liou
S.C. Ou

Center for Atmospheric and Remote Sounding Studies
Department of Meteorology
University of Utah
Salt Lake City, UT 84112

DTIC
ELECTE
APR 17 1991
C D

Final Report
1 July 1987 - 31 October 1990

31 January 1991

DTIC FILE COPY

91 4 16 050

Approved for public release;
distribution unlimited.

COMPLETED PROJECT SUMMARY

TITLE: Development and Verification of a Physical Cloud-Moisture Model for use in General Circulation Models

PRINCIPAL INVESTIGATOR: Professor K. N. Liou
Department of Meteorology/CARSS
University of Utah
Salt Lake City, Utah 84112

INCLUSIVE DATES: 1 July 1987 - 31 October 1990

CONTRACT/GRANT NUMBER: AFOSR 87-0294

COSTS AND FY SOURCE: \$102,030, FY87; \$105,703, FY88; \$109,931, FY89

SENIOR RESEARCH PERSONNEL: Dr. S. C. Ou

JUNIOR RESEARCH PERSONNEL: J. L. Lee B. Mitchell
S. K. Krueger Q. Zheng

PUBLICATIONS ACKNOWLEDGING AFOSR SUPPORT:

Liou, K.N., Q. Fu, and T.P. Ackerman, 1988: A simple formulation of the delta-four-stream approximation for radiative transfer parameterizations. J. Atmos. Sci., 45, 1940-1947.

Liou, K.N., and Q. Zheng, 1989: An investigation of the role of clouds/radiation in a general circulation model. In Current Problems in Atmospheric Radiation, J. Lenoble and J. Geleyn, Eds., A. Deepak Publishing, Hampton, pp. 119-122.

Zheng, Q., and K.N. Liou, 1989: The role of clouds/radiation in long-range numerical weather prediction. Acta Meteor. Sinica, 3, 603-617.

Liou, K.N., and S.C. Ou, 1989: The role of cloud microphysical processes in climate: An assessment from a one-dimensional perspective. J. Geophys. Res., 94, 8599-8607.

Liou, K.N., S.C. Ou, and G. Koenig, 1990: An investigation on the climatic effect of contrail cirrus. In Air Traffic and the Environment - Background, Tendencies and Potential Global Atmospheric Effects, U. Schumann, Ed., Lecture Notes in Engineering, Springer-Verlag, pp. 154-169.

Liou, K.N., J.L. Lee, S.C. Ou, Q. Fu, and Y. Takano, 1991: Ice cloud microphysics, radiative transfer and large-scale cloud processes. meteor. Atmos. Phys., 40, (in press).

Mitchell, B., 1991: Analysis of global radiation budget and cloud forcing using three-dimensional cloud nephelometer data bases. M.S. Thesis, Department of Meteorology, University of Utah.

Lee, J.L., 1991: Development and verification of a physically-based cloud-moisture model. Ph.D. dissertation (in preparation), Department of Meteorology, University of Utah.

ABSTRACT OF OBJECTIVES AND ACCOMPLISHMENTS:

The following three research phases were planned:

- (1) Develop the general framework of a cloud-moisture model and perform sensitivity analyses for a one-dimensional cloud model. Analyze the 3DNEPH cloud and earth radiation budget data from January and July 1979 for verification of the cloud model.
- (2) Develop a physically-based three-dimensional cloud-moisture model. Develop parameterization schemes for cloud microphysical processes, including ice phase.
- (3) Verification of the large-scale cloud model with available cloud, radiation and synoptic data. Perform numerical experiments to investigate the effects of cloud-radiation interactions and feedbacks on large-scale temperature fields, and the efforts of infrared radiative cooling and ice processes on the prediction of cloud cover and cloud liquid/ice water content.

A time-dependent, three-dimensional, large-scale cloud-moisture model has been developed for the prediction of cloud cover, cloud liquid/ice water content, precipitation, specific humidity and temperature. The wind field is prescribed using the results from a general circulation model. The model includes parameterizations of ice and water cloud microphysical processes, and solar and infrared radiative transfer involving cloud layers. The predicted cloud and radiation fields compare reasonably well with those analyzed from 3DNEPH and earth radiation budget data. Infrared cooling enhances the formation of high and middle cloud cover and increases the liquid/ice water content. The incorporation of ice processes, on the other hand, reduces the total cloud water due to the gravitational settling of cloud particles. The large-scale cloud model developed in this study should be of value to the development of general circulation and climate models.

Accession Var	
NTS	<input checked="" type="checkbox"/>
DTIC DS	<input type="checkbox"/>
Unannounced	<input type="checkbox"/>
Justification	
By	
Distribution	
Availability Codes	
Avail and/or	
Dist	Special
A-1	

DEVELOPMENT AND VERIFICATION OF A THREE-DIMENSIONAL
LARGE-SCALE CLOUD MODEL

J.L. Lee
K.N. Liou
S.C. Ou

Center for Atmospheric and Remote Sounding Studies
Department of Meteorology
University of Utah
Salt Lake City, UT 84112

Final Report
1 July 1987 - 31 October 1990

31 January 1991

Title on 1473 is correct per telecon
Cathy (AFOSR) 202/767-4960 5/6/91

UNCLASSIFIED

SECURITY CLASSIFICATION OF THIS PAGE

REPORT DOCUMENTATION PAGE

1a. REPORT SECURITY CLASSIFICATION Unclassified			1b. RESTRICTIVE MARKINGS		
2. SECURITY CLASSIFICATION AUTHORITY			3. DISTRIBUTION/AVAILABILITY OF REPORT Approved for public release; distribution unlimited		
2b. DECLASSIFICATION/DOWNGRADING SCHEDULE			4. PERFORMING ORGANIZATION REPORT NUMBER(S)		
4. PERFORMING ORGANIZATION REPORT NUMBER(S)			5. MONITORING ORGANIZATION REPORT NUMBER(S)		
6a. NAME OF PERFORMING ORGANIZATION Center for Atmospheric and Remote Sounding Studies		6b. OFFICE SYMBOL (If applicable) CARSS		7a. NAME OF MONITORING ORGANIZATION Air Force Office of Scientific Research	
6c. ADDRESS (City, State, and ZIP Code) Department of Meteorology University of Utah Salt Lake City, Utah 84112		7b. ADDRESS (City, State, and ZIP Code) Bolling Air Force Base Washington, D.C. 20332		Bcl 410	
8a. NAME OF FUNDING/SPONSORING ORGANIZATION AFOSR		8b. OFFICE SYMBOL (If applicable) NL		9. PROCUREMENT INSTRUMENT IDENTIFICATION NUMBER AFOSR-87-0294	
8c. ADDRESS (City, State, and ZIP Code) Bolling AFB, DC 20332-6448		10. SOURCE OF FUNDING NUMBERS			
		PROGRAM ELEMENT NO. 61102 F	PROJECT NO. 2310	TASK NO. A1	WORK UNIT ACCESSION NO.
11. TITLE (Include Security Classification) Development and Verification of a Physical Cloud-Moisture Model for use in General Circulation Models					
12. PERSONAL AUTHOR(S) J. L. Lee; K. N. Liou; S. C. Ou					
13a. TYPE OF REPORT Final		13b. TIME COVERED FROM 7-1-87 TO 10-31-90		14. DATE OF REPORT (Year, Month, Day) 31 January 1991	
				15. PAGE COUNT 153	
16. SUPPLEMENTARY NOTATION					
17. COSATI CODES			18. SUBJECT TERMS (Continue on reverse if necessary and identify by block number)		
FIELD	GROUP	SUB-GROUP	Cloud modeling, parameterization of microphysical processes, radiative transfer, numerical weather prediction.		
19. ABSTRACT (Continue on reverse if necessary and identify by block number) A time-dependent, three-dimensional, large-scale cloud-moisture model has been developed for the prediction of cloud cover, cloud liquid/ice water content (LWC/IWC), precipitation, specific humidity and temperature. Partial cloudiness is allowed to form when large-scale relative humidity is less than 100%. In the vertical, a 16-layer z-coordinate is adopted. The horizontal resolution is described by 48 equally-spaced longitudinal points and 38 Gaussian latitudes. The wind field is prescribed using the results from a general circulation model (GCM). Both liquid and ice phases are included in the model. The liquid phase processes consist of evaporation, condensation, autoconversion, and precipitation. The ice phase processes include heterogeneous nucleation to generate ice crystals, depositional growth to simulate Bergeron-Findeison's processes, sublimation to deplete ice crystals, and gravitational settling of ice crystals. The radiative transfer parameterization program is based on a broadband method and involves the transfer of infrared and solar radiation in clear and cloudy regions. Broadband infrared emissivity, reflectivity, and transmissivity					
20. DISTRIBUTION/AVAILABILITY OF ABSTRACT <input checked="" type="checkbox"/> UNCLASSIFIED/UNLIMITED <input type="checkbox"/> SAME AS RPT <input type="checkbox"/> DTIC USERS			21. ABSTRACT SECURITY CLASSIFICATION UNCLASSIFIED		
22a. NAME OF RESPONSIBLE INDIVIDUAL H. P. I. Stober			22b. TELEPHONE (Include Area Code) 702-767-4410		22c. OFFICE SYMBOL NL

for cirrus clouds, as well as the broadband solar absorption, reflection and transmission values for various cloud types are computed based on the LWC and IWC interactively generated by the cloud model. Clouds, through their radiative properties, may produce changes in radiative heating, which in turn feeds back to the clouds via the thermodynamic equation and modifies the cloud fields. Large amounts of satellite data, including cloud cover climatology derived from the U.S. Air Force three-dimensional nephanalysis (3DNEPH) and earth radiation budget (ERB), have been processed into formats appropriate for verification. The 96-hour model simulations of cloud cover, outgoing longwave radiation (OLR) and net solar flux at the top of the atmosphere (TOA), and cloud LWC have been verified against data analyzed from 3DNEPH, ERB and the Nimbus-7 Scanning Multi-channel Microwave Radiometer (SMMR) satellite observations, respectively. The predicted cloud IWC is compared to in-situ observations as well as to results from other studies. The predicted cloud and radiation results compare reasonably well with those analyzed from satellite data. The moisture, cloud fields and earth radiation budget are physically linked together by the cloud microphysical processes simulated in the large-scale cloud model, which further relates these cloud and radiation fields to large-scale temperature and vertical velocity. The cloud LWC in the simulation strongly depends on the vertical velocity which is essential to the condensational process, while the simulated cloud IWC appears to depend more on temperature than vertical velocity. The simulated maximum cloud IWC occurs at $\sim -15^{\circ}\text{C}$, which is the temperature for the maximum ice crystal depositional rate observed by many cloud microphysicists. Numerical experiments are carried out with and without radiation and ice phase processes in the cloud formation scheme. The inclusion of radiation produces a significant change in temperature, cloud cover and total cloud water content, while the inclusion of ice-phase processes generates a substantial change only in total cloud water content. If the cloud LWC is sufficiently large to support effective Bergeron-Findeison's processes, the total cloud water content decreases, indicating that gravitational settling is an efficient mechanism in reducing the cloud IWC.

CONTENTS

SECTIONS

1. INTRODUCTION	1
1.1 The Important Role of Clouds in the Earth-Atmosphere System .	1
1.2 A Review of Large-Scale Cloud Works	2
1.2.1 Satellite data analysis	3
1.2.2 Numerical model works	4
1.2.2.1 Diagnostic method	5
1.2.2.2 Prognostic method	7
1.3 The Uncertainty of Cloud Effects in Model Studies	9
1.4 The Importance of Cloud Liquid/Ice Water to Radiative Transfer .	11
1.5 The Present Large-Scale Cloud Study	13
2. MODEL DESCRIPTION	15
2.1 Governing Equations	15
2.2 Cloud Microphysical Processes Simulated in the Model	20
2.3 Numerical Implementation	23
2.4 Radiative Transfer Parameterization	25
3. BULK PARAMETERIZATIONS OF SOURCES AND SINKS OF MICROPHYSICAL PROCESSES	30
3.1 Liquid Phase	30
3.1.1 Condensation	30
3.1.2 Autoconversion	31
3.1.3 Evaporation of raindrops	33
3.2 Ice Phase	35
3.2.1 Homogeneous nucleation	35
3.2.2 Heterogeneous nucleation	35
3.2.3 Bergeron-Findeison's processes	36
3.2.4 Sublimation and melting of ice crystals	42
3.2.5 Gravitational settling	42
3.2.5.1 Crystal mass and terminal velocity	45
3.2.5.2 Downward ice flux	47
4. MODEL INPUT AND VERIFICATION DATASETS	50
4.1 Model Input Datasets	50
4.2 Verification Datasets	58
4.2.1 3DNEPH cloud data	58
4.2.2 Earth Radiation Budget (ERB) dataset	61
4.2.3 Scanning Multichannel Microwave Radiometer (SMMR) . .	63

5. MODEL PERFORMANCE AND VERIFICATION	68
5.1 Design of the Verification	68
5.2 Initial Data	70
5.3 Model Results and Verification	76
5.3.1 Zonal means	76
5.3.1.1 Zonal mean cloud cover	76
5.3.1.2 Zonal mean earth's radiation budget	79
5.3.1.3 Zonal mean cloud LWP	84
5.3.2 Geographical distribution of cloud simulations	86
5.3.2.1 Cloud cover	86
5.3.2.2 Earth's radiation budget	89
5.3.2.3 Liquid water path	94
5.3.2.4 Precipitation	95
5.3.3 Cloud ice content	98
5.4 Discussion	100
6. SENSITIVITY STUDIES	105
6.1 Control Run	105
6.2 Experiment on Inclusion of Radiation	111
6.3 Experiment on Ice Phase Processes	122
7. SUMMARY AND CONCLUSION	136

APPENDICES

A. DERIVATION OF PRECIPITATION EQUATION IN (2.5)	142
B. DERIVATION OF LARGE-SCALE CONDENSATION	144
C. PARAMETERIZATION OF RAINDROPS EVAPORATION	145
REFERENCES	147

Section 1

INTRODUCTION

1.1 The Important Role of Clouds in the Earth-Atmosphere System

Understanding the role of clouds in the earth's radiation and heat budgets becomes one of the foremost tasks in the atmospheric sciences. Clouds may have an important influence on earth radiation budget in determining the earth's climate, on atmospheric circulation in contributing to atmospheric energetics, and on the atmospheric hydrological cycle in generating precipitation which is of economic and societal importance.

Clouds regularly occupy about 50% of the sky on a global scale and are one of the most important regulators of the earth's radiation budget, i.e., the balance between incoming solar radiation and outgoing longwave radiation at the top of the atmosphere (TOA), by which the earth's climate is determined. On the one hand, clouds reflect a large portion of incoming solar radiation producing a cooling effect, referred as the albedo effect. On the other, they trap the outgoing longwave radiation emitted from the earth resulting a warming effect, referred as the greenhouse effect. Since the greenhouse and albedo effects are different in sign as well as magnitude, the existence of clouds may have a profound impact upon the sensitivity of the climate to external perturbations such as a doubling of atmospheric carbon dioxide. In particular, cirrus clouds, which regularly cover about 20% of the globe, are optically thin and nonblack. The outcome of the

greenhouse-versus-albedo effects is intrinsically modified by the radiative effects of nonblack cirrus (Liou,1986).

Exchanges of latent heat due to the formation and dissipation of clouds directly contribute to the atmospheric energetics which drive global atmospheric circulations. More importantly but less directly, the radiative properties of clouds produce changes in radiative heating and modify the atmospheric temperature profiles, which in turn cause changes in the atmospheric dynamic structure. For instance, cloud-induced radiative heating substantially alters the equator-to-pole temperature gradient and results in changes of zonal mean winds by the virtue of the thermal wind relationship. Ramanathan et al. (1983) demonstrated that cirrus clouds exert a significant influence on the meridional gradient in upper-tropospheric radiative heating, which in turn strengthens the tropospheric jet stream. The amount of this strengthening depends on the cirrus cloud emissivity, which is a function of cloud ice content.

The presence of water and its phase transitions in clouds uniquely distinguish clouds as the most important component in the atmospheric hydrological cycle. Clouds serve as a modulator to transform water from vapor to liquid and solid phases, and cause precipitation by the virtue of gravitation. Precipitated water makes it possible for the earth to support various kinds of plant and animal life, in particular human beings.

1.2 A Review of Large-Scale Cloud Works

Recognizing the importance of clouds, numerous efforts have been directed toward determining the effects of clouds on the atmosphere in two ways. One is data analysis based on satellite observations such as earth radiation budget data and cloud nephanalysis. The other is the inclusion of a more physically based cloud parameterization scheme in atmospheric general circulation models (GCMs).

1.2.1 Satellite data analysis

Based on observed satellite radiation data, Cess (1976), Hartman and Short (1980), Ohring and Clapp (1980), Ohring et al. (1981), and Cess et al. (1982) examined the sensitivity of radiation budget to variations in cloudiness. Cess (1976), based on both annual and seasonal climatology, suggested that the albedo effect, as a result of variation in cloud amounts, is balanced by the greenhouse effect either globally or zonally. However, similar studies carried out by Ohring and Clapp (1980), Hartman and Short (1980), and Ohring et al. (1981), using the scanning radiometer observations of the National Oceanic and Atmospheric Administration (NOAA) satellites, showed that the albedo effect is much greater than the greenhouse effect from changes in cloud amounts; i.e., the net radiation at TOA is sensitive to changes in cloud amounts. In these studies, the estimations of cloud amount changes were indirectly derived from albedo changes rather than satellite observational cloud amounts.

In view of the uncertainty associated with cloud amounts in these studies, Koenig et al. (1987) employed the cloud climatology data derived from the U.S. Air Force three-dimensional nephanalysis (3DNEPH) cloud data base, as well as the broadband radiation budget data derived from the Nimbus 7 Earth Radiation Budget (ERB) measurements, to undertake a similar study on regional, zonally averaged, and hemispheric scales. They compared the changes in solar, infrared (IR), and net fluxes derived from ERB data with respect to the changes in cloud amounts deduced from 3DNEPH cloud data and found the albedo effect dominates the greenhouse effect on a regional, zonal and hemispherical basis.

Ramanathan et al. (1989) undertook a different approach to analyze the Earth Radiation Budget Experiment (ERBE) data, which were derived from the observations of three satellites in different orbits to include diurnal variations. A cloud forcing, the difference between clear-sky and cloudy-sky fluxes at TOA, was defined

to assess the radiative effects of clouds on climate. Ramanathan et al., based on the data, suggested that the maximum short-wave cloud forcing, with some of the values over 100 W/m^2 , occurred in the mid- to high-latitude oceanic regions coinciding with regions of stratus and the storm tracks of mid-latitude cyclones. The longwave cloud forcing had peak values of 50 to 100 W/m^2 over tropical regions and decreased toward the poles. In the tropics, the longwave and shortwave forcing terms nearly cancelled each other out with the net forcing within $\pm 10 \text{ W/m}^2$. However, it was also suggested that the longwave forcing (heating) happens primarily in the troposphere, while the shortwave forcing (cooling) takes place largely at the earth's surface. Thus, strong vertical radiative heating/cooling gradients may be generated by the clouds in the tropics. In the global case, the shortwave cloud forcing (-44.5 W/m^2) due to the enhancement of planetary albedo, exceeded in magnitude the longwave cloud forcing (31.3 W/m^2) resulting from the greenhouse effect of clouds. They concluded that clouds have a net cooling effect on the earth.

In summary, the above data analysis based on satellite observations indicates that the solar albedo effect is larger than the IR greenhouse effect at TOA due to variations in cloud cover.

1.2.2 Numerical model works

Satellite and *in situ* observations over the past two decades have greatly increased our knowledge of cloud radiative effects on the climate, but a real understanding of how clouds feed back to various processes of the earth-atmosphere system remains unknown to us and requires efforts in improving the cloud scheme in numerical models. The formation of clouds in GCMs may be separated into the diagnostic and prognostic methods. The former is an empirical approach in which cloud cover and cloud liquid water content (LWC) are generated empirically from other model variables (see, e.g., Slingo 1980). The latter is a prognostic approach with an

additional water budget equation(s) for prognostic cloud water content (see, e.g., Sundqvist, 1978), providing a more direct link(s) among the radiative, dynamical, and hydrological processes within models.

1.2.2.1 Diagnostic method

In early model works, the formation of clouds was very crude and lacked physical foundation. An arbitrary fractional amount of cloud was assigned to a given layer where large-scale condensation occurs. All the excessive water vapor was condensed and immediately precipitated onto the ground. As a result, there was no cloud LWC or cloud ice remaining in the clouds. These two elements are necessary for the calculation of cloud radiative effects. In climatic perturbation studies, Shukla and Sud (1981) suggested that cloud cover, through cloud radiation interaction, can produce changes in the hydrological cycle, which in turn results in substantial changes in thermal forcing and dynamical circulations.

Wetherald and Manabe (1980) assigned a cloud amount of 80% to condensation so that the model atmosphere would equilibrate at a realistic temperature. They demonstrated that the greenhouse and albedo effects induced by cloud cover variations compensated for each other. Therefore, they concluded that cloud feedback processes are unimportant to the sensitivity of climate to a forcing such as a change in solar constant or atmospheric carbon dioxide. Nevertheless, in their subsequent studies with realistic geography, Wetherald and Manabe (1986, 1988) found that cloud feedback processes enhance the sensitivity of the model climate to an increase in atmospheric carbon dioxide. This conclusion is in agreement with that drawn by Hansen et al. (1983). In addition, the features of cloud cover change obtained in these two studies, as well as in that of Washington and Meehl (1984), are qualitatively similar.

More recently, increasing efforts have been placed on improving either the radiative properties of clouds or cloud parameterization schemes in GCMs to show the importance of cloud-radiation interaction to the simulation of atmospheric circulation. Ramanathan et al. (1983) demonstrated that refinement in radiative properties of nonblack high cirrus emissivity significantly improves the model simulation of atmospheric temperatures as well as zonal mean winds. Substantial increases in temperature of about 10° K and 2° K in the upper troposphere at the winter and summer polar regions, respectively, and a decrease in temperature about 2° to 3° K in the tropical upper troposphere were found when the high cloud emissivities were arbitrarily taken as values less than 1. These changes, by virtue of the thermal wind relationship, brought the magnitudes of their simulated tropospheric jets into much closer agreement with those observed in the atmosphere. Slingo and Slingo (1988) reached the same conclusion in their study of cloud longwave radiative forcing. Following the cloud scheme proposed by Geleyn (1981) in a simple quadratic form, Liou and Zheng (1984) employed a GCM designed for medium range weather prediction and showed the importance of cloud and radiative processes to the maintenance of the Hadley circulation.

To improve the cloud cover scheme in GCMs, Slingo (1980, 1987) derived an empirical cloud parameterization scheme from the studies of the GARP (Global Atmospheric Research Program) Atlantic Tropical Experiment (GATE) data. She empirically related the model cloudiness to the large-scale model variables such as relative humidity, atmospheric stability, convective activity and temperature lapse rate. In her works, the predicted cloudiness was verified against that derived from Nimbus 7 and showed an improvement in forecasting tropical and extra-tropical cloudiness. Slingo also suggested that a cloud parameterization can be at least as important as that of radiative transfer.

1.2.2.2 Prognostic method

The prognostic method which requires the additional prognostic equation(s) for cloud LWC and/or cloud ice water content (IWC), can interactively provide cloud LWC and IWC to be used in the calculation of cloud optical properties. However, the formation of clouds and their radiative properties depend on many microphysical processes that can not be determined in large-scale models. Nor is it possible in a large-scale model to resolve these microphysical processes for each individual cloud particle. It also is not easy to empirically relate these microphysical properties, i.e., cloud LWC and IWC, to GCM variables such as relative humidity, wind, temperature and static stability. We have to rely on the bulk quantities which represent the various source and sink terms in the water budget equation(s).

Sundqvist (1978) made the first attempt to develop a physically based prognostic large-scale cloud scheme for use in a GCM. In his approach, the cloud LWC is a prognostic variable determined by various source and sink terms which are parameterized in terms of associated bulk quantities. Also partial cloudiness is allowed to form when a large-scale relative humidity is less than 100%.

Sundqvist (1981) incorporated the proposed cloud scheme into the European Center for Medium Range Weather Forecasts (ECMWF) GCM and carried out a 5-day integration. The forecast cloud amounts were compared with satellite photographs, which showed that the cloud patterns are reasonably well-simulated; the predicted cloud LWC were within an observational range. Since then, there is an increasing effort to include the prognostic cloud LWC into GCMs. For example, Sundqvist's cloud scheme has been adopted in the Goddard Institute for Space Studies (GISS) GCM. (see, Geno, 1990).

Mitchell et al. (1989) conducted a study of cloud feedback in the UK Meteorological Office atmospheric general circulation model which is gridded by 11 vertical levels and a $5^\circ \times 7^\circ$ (latitude \times longitude) horizontal spacing, with an inclusion

of 50-m ocean mixed layer. A cloud liquid water budget equation was included in the model. Furthermore, water cloud was smoothly converted into ice cloud with its ice crystal bulk terminal velocity arbitrarily assumed to be 1 m/s. According to their results, which were averaged over five years after the simulations reached equilibrium, the global surface warming due to doubled carbon dioxide was reduced from about 5.2° to 2.7° K as the prognostic water was included. When the cloud radiative properties, which were calculated based on the schemes developed by Liou and Wittman (1979) for short-wave albedo and transmittances and Stephens (1978) for long-wave flux emittance, were allowed to depend on the cloud water content, the surface warming dropped further, to only 1.9° K. They concluded that clouds exert a substantial negative feedback on the climate. This conclusion is clearly contradictory to that obtained by Roeckner (1988).

Roeckner (1988) performed a 30-year simulation using the Meteorological Institute/University of Hamburg GCM, with coupled mixed-layer ocean and sea-ice models to investigate cloud feedback effects with response to a 2% increase in the solar constant – roughly equivalent to a CO₂ doubling. He separated high (non-black) clouds from low and middle (black) clouds and calculated cloud radiative properties in the GCM. Roeckner concluded, based on his results, that the net cloud feedback is positive for the atmosphere and for the whole planet but negative for the surface. He indicated that the positive feedback of the cloud optical depth is largely contributed by the increase of high cloud infrared opacity, especially in the tropics.

Liou et al. (1990) investigated the sensitivity of cloud microphysics and radiative transfer parameterizations to large-scale cloud processes using the 3-D global cloud model developed by Lee et al. (1990). In the cloud model, cloud IWC was a prognostic variable based on the cloud ice water budget equation. Liou et al. explored the means by which cloud microphysics and radiative transfer associated with cirrus

clouds were physically parameterized in terms of the mean effective size (D_e) and ice water path (IWP). The IWP was given by the IWC and model thickness; the D_e could be related to the IWC through their dependence on the maximum dimension of ice crystals. These two quantities, D_e and IWP, were used to parameterize the optical depth of cirrus. With the prognostics of IWC, the radiative properties of cirrus clouds, namely solar reflectivity and absorptivity and IR emissivity, were interactively calculated based on the developed parameterizations.

They found a strong dependence of cirrus radiative properties on the D_e . For a given IWP, smaller D_e reflected more solar radiation, emitted more IR radiation and enhanced net radiative heating/cooling at the cloud top and bottom than larger sizes. It was also indicated that cirrus clouds are largely controlled by IR heating/cooling. They demonstrated in a 24-hour simulation that a variation in the D_e from 50 to 75 μm leads to an increase of high cloud cover in some latitudes by as much as 4% and, at the same time, a decrease of middle cloud cover by 3-4% in latitudes between 60° S and 60° N.

1.3 The Uncertainty of Cloud Effects in Model Studies

Predictions of climate change, natural and/or human-induced, are deeply degraded by unfaithful simulations of cloud effects in numerical models. Indeed, it has been debated for years whether clouds cool or warm the climate. For example, in his climatic perturbation study in a GCM, Smagorinsky(1978) suggested that the increase in CO_2 will enhance evaporation from the earth's surface and increase the amount of low clouds, thus exerting a cooling effect on climate. On the other hand, studies by Road (1978) and Schneider et al. (1978) indicated that cloud variations may have a positive feedback effect on the sensitivity of the global mean climate due to decreasing cloud cover in the models as the sea surface temperature increased.

More recently, two GCMs with explicit cloud water budgets produced conflicting results as they were applied to climate sensitivity simulations. Mitchell et al. (1989)

found that changes in the relative amounts of ice and liquid clouds were sufficient to reduce the equilibrium surface warming by half, and a further reduction of 0.8° K in surface warming was contributed by the negative cloud optical feedbacks. They concluded the cloud feedback to climate change is negative.

On the other hand, Roeckner (1988) drew the conclusion that the net cloud feedback is positive for the whole planet. In his simulation, low and middle clouds decrease at low latitudes but increase at high latitudes in response to a 2% rise in the solar constant. He decomposed the planetary radiation budget into surface and atmosphere components due to changes in cloud cover and cloud water, separately for high (non-black) clouds, and for low and middle (black) clouds. Roeckner found that the increase of cloud LWC produced a substantial surface cooling which overcompensated for the cloud cover effect so that the net cloud feedback was negative at the surface. However, the atmosphere was heated substantially by the increase of high cloud LWC and the associated rise in IR flux emissivity, especially in the tropics. He suggested that changes of cloud cover and LWC in low and middle clouds are only of minor importance for the atmosphere. The planetary radiation change is obviously dominated by cloud LWC and the associated IR emissivity for high cirrus clouds.

In view the significant differences in cloud effects simulated by current GCMs, Cess et al. (1989) made an intercomparison of cloud feedback in 14 GCMs and found a wide range of disagreement that varied from modest negative to strong positive feedback. Most of this disagreement arises from inconsistency in representing cloud effects among the models. They defined climate and clear-sky sensitivity parameters to assess a climate change in the cloudy and clear sky conditions, respectively. In the intercomparison of the sensitivity parameters derived from the GCMs, they found that there are big differences among the global climate sensitivity parameters, but excellent agreement in the clear-sky sensitivity parameter. Their results clearly

indicated that the inconsistency in cloud feedback may be one of the largest sources of the wide range of disagreement in the climatic sensitivity studies.

1.4 The Importance of Cloud Liquid/Ice Water to Radiative Transfer

While it is difficult to accurately quantify the effects of clouds on the climate, atmospheric scientists generally agree that the parameterizations of cloud water/ice content and cloud radiative properties are essential to the differences in the predictions of climate change. Until recently, clouds in most GCM studies have been accounted for by cloud cover only, and the optical properties of clouds have had to be calculated separately based on the prescribed values of cloud liquid/ice water content. Cloud-radiation feedbacks in GCM have only resulted from changes in cloud cover. Thus, the cloud optical feedback, produced by shortwave albedo or IR emissivity, has been missing.

To return this missing feedback is the prime objective to for including cloud LWC and IWC as additional prognostic variables in models. For instance, it may be expected that an increase in cloud liquid water as a result of climate warming could enhance cloud albedo to produce a negative cloud feedback. Somerville and Remer (1984) employed the temperature dependence of cloud optical thickness in a radiative-convective model and showed that a significant negative feedback arises from the albedo effect of cloud liquid water. In their study, they made no distinction of high thin cirrus which may result in a positive feedback due to the nonblack emissivity of high clouds. Roeckner (1988), on the other hand, separated high (non-black) clouds from low and middle (black) clouds and found cloud radiative properties generated a positive feedback due to the increased infrared opacity of high cirrus clouds. As he neglected ice phase in his study, Roeckner's conclusion was vulnerable. Since cirrus clouds are dominated by ice crystals, the ice phase must

be included in the model physics in order to accurately calculate cirrus infrared opacity.

Liou et al. (1990) proposed a new link between the radiative properties of cirrus clouds and climate change, showing how variations in the D_e of cirrus contribute to changes in middle and high clouds. Due to differences in cirrus radiative properties for different D_e , high cirrus clouds that are composed of smaller D_e would produce more cooling and heating above and below the cloud region, respectively, than larger D_e . They showed that more high cloud and less middle cloud are simulated as the D_e increased from 50 to 75 μm . This may lead to the strength of the greenhouse effect, since high and middle clouds are dominated by the greenhouse and albedo effects, respectively. However, it depends on how the D_e responds to climate warming to determine whether the contribution of D_e to cloud feedback on climate change is positive or negative.

Based on Heymsfield and Platt (1984), ice crystal sizes and the consequence of D_e are strongly dependent on the temperature, in that the higher the temperature, the larger the ice crystals and D_e . Following this relation, one may expect the size of D_e in cirrus increases in response to climate warming and results in the decrease and increase of high and middle clouds, respectively. This may lead to a reduction in the greenhouse effect and, at the same time, an enhancement of the albedo effect. As a result, climate warming may be neutralized due to the effects of D_e on the radiative properties of cirrus clouds.

According to the preceding literature reviews, it is clear that the effects of clouds on the earth's climate depend not only on cloud cover but also on the cloud optical properties determined by cloud LWC as well as cloud IWC. In particular, it is well-known that the radiative effects of cirrus clouds, which consist of nonspherical ice crystals, are a potentially important component of weather and climate systems (Liou, 1986). In order to include cloud effects faithfully in the GCM studies, not

only the cloud cover but cloud LWC and IWC need to be explicitly included in the model physics.

1.5 The Present Large-Scale Cloud Study

The objective of this study is to develop and to verify a prognostic large-scale stratiform cloud model. In addition to cloud cover, the model predicts cloud LWC and IWC to provide two more physical elements for the calculation of cloud radiative properties, such as shortwave albedo or IR flux emissivity. The model, consisting of liquid and ice water substances budget equations, is based on the laws of mass conservation and thermodynamics. The ice phase (cloud IWC), which is physically included for the first time in a large-scale cloud model, is used to account for cirrus clouds. Various source and sink terms are parameterized in terms of so-called bulk quantities. The ice crystals bulk terminal velocity is directly related to cloud IWC and is interactive in the cloud model. The bulk parameterizations generally follow Kessler (1969), and Sundqvist (1978, 1988) for the liquid phase and Koenig and Murray (1976), Symmsfield and Platt(1984), and Starr and Cox (1985) for the ice phase.

An assessment of the validity of any new parameterization scheme is at least as important as that of the development of the scheme. In addition to conventional meteorological elements such as temperature and precipitation, the model predicted cloud cover, cloud LWC and IWC, as well as the radiation budget, need to be carefully verified against observations. Cloud cover observational data can either be compiled from conventional surface observations or deduced from satellite remote-sensing data. Ground based cloud cover observations have been recorded for centuries. The cloud cover climatology compiled by London (1957) based on surface observations is a widely used cloud climatology.

Aware of the importance of satellite data for climatic studies, a number of satellite observational programs had been undertaken, e.g., the International Satellite

Cloud Climatology Project (ISCCP, 1985), the First ISCCP Regional Experiment (FIRE, 1985), and the Earth Radiation Budget Experiment (ERBE, 1984). In addition, earth radiation budget (ERB) data was recorded by the Nimbus-7 satellite (Kyle et al., 1985). The U.S. Air Force three-dimensional nephelometer (3DNEPH) program is the only operational, high resolution cloud analysis based on both satellite and conventional cloud observations. The ERB and 3DNEPH data are used as verification data in this study and will be further described in Section 4.

Compared to cloud cover, data on cloud LWC are very limited. The widely used cloud LWC data are those derived from the Nimbus 7 Scanning Multi-Channel Microwave Radiometer (SMMR). The SMMR data consist of vertically integrated liquid water content in clouds and rain over the oceans equatorward of 60° latitude. The vertically integrated liquid water content is referred as the liquid water path (LWP). So far, there is no observational cloud IWC data that can be utilized as verification data on the global basis. Aircraft *in situ* measurements of cirrus cloud properties such as cloud IWC were reported by Heymsfield (1975, 1977). These data may be used to qualitatively assess the model-predicted cloud IWC. The examination of verification data based on satellite observation will be described in some detail in Section 4.

Section 2

MODEL DESCRIPTION

2.1 Governing Equations

We have developed a time-dependent, three-dimensional cloud-moisture model for the prediction of water vapor, cloud LWC, cloud IWC, precipitation and temperature. The first four variables are governed by the law of mass conservation. The latent heat exchanges during the phase transitions of water substances are ruled by the first law of thermodynamics through the temperature field. The governing equations may be written as follow:

$$\begin{aligned} & \frac{\partial}{\partial t}(\bar{\rho}\bar{T}) + \frac{1}{a\cos\phi} \left[\frac{\partial}{\partial \lambda}(\bar{\rho}\bar{T}\bar{u}) + \frac{\partial}{\partial \phi}(\bar{\rho}\bar{T}\bar{v}\cos\phi) \right] + \frac{\partial}{\partial z}(\bar{\rho}\bar{T}\bar{w}) + \bar{\rho}\Gamma_d\bar{w} \\ &= \bar{\rho}(\eta\bar{Q}_c + \bar{Q}_R) - \frac{L_c}{C_p}(1-\eta)\bar{E}_r + \frac{L_f}{C_p}\eta\bar{S}_{BF} - \frac{L_d}{C_p}(1-\eta)\bar{S}_s + F_H^T + F_V^T, \end{aligned} \quad (2.1)$$

$$\begin{aligned} & \frac{\partial}{\partial t}(\bar{\rho}\bar{q}_v) + \frac{1}{a\cos\phi} \left[\frac{\partial}{\partial \lambda}(\bar{\rho}\bar{q}_v\bar{u}) + \frac{\partial}{\partial \phi}(\bar{\rho}\bar{q}_v\bar{v}\cos\phi) \right] + \frac{\partial}{\partial z}(\bar{\rho}\bar{q}_v\bar{w}) \\ &= -\frac{C_p}{L_c}\bar{\rho}\eta\bar{Q}_c + \bar{\rho}(1-\eta)\bar{E}_r + (1-\eta)\bar{S}_s + F_H^{qv} + F_V^{qv}, \end{aligned} \quad (2.2)$$

$$\begin{aligned} & \frac{\partial}{\partial t}(\bar{\rho}\bar{q}_l) + \frac{1}{a\cos\phi} \left[\frac{\partial}{\partial \lambda}(\bar{\rho}\bar{q}_l\bar{u}) + \frac{\partial}{\partial \phi}(\bar{\rho}\bar{q}_l\bar{v}\cos\phi) \right] + \frac{\partial}{\partial z}[\bar{\rho}\bar{q}_l(\bar{w} - \bar{w}_l)] \\ &= \frac{C_p}{L_c}\bar{\rho}\eta\bar{Q}_c - \bar{\rho}\eta\bar{P} - \eta\bar{S}_{BF} + F_H^{ql} + F_V^{ql}, \end{aligned} \quad (2.3)$$

$$\begin{aligned} & \frac{\partial}{\partial t}(\bar{\rho}\bar{q}_i) + \frac{1}{a\cos\phi} \left[\frac{\partial}{\partial \lambda}(\bar{\rho}\bar{q}_i\bar{u}) + \frac{\partial}{\partial \phi}(\bar{\rho}\bar{q}_i\bar{v}\cos\phi) \right] + \frac{\partial}{\partial z}[\bar{\rho}\bar{q}_i(\bar{w} - \bar{V}_T)] \\ &= \frac{C_p}{L_d} \bar{\rho}\eta\bar{Q}_i + \eta\bar{S}_{BF} - (1-\eta)\bar{S}_s + F_H^{qi} + F_V^{qi} \quad , \end{aligned} \quad (2.4)$$

$$- \frac{\partial}{\partial z}(\bar{P}) = \bar{\rho}\eta\bar{P} - (1-\eta)\bar{\rho}\bar{E}_r \quad , \quad (2.5)$$

Equation (2.5) is derived from the rain water budget equation based on the consideration of scaling parameters. The derivation is shown in Appendix A. In these equations, an overbar denotes the average of a variable over a grid space. The variables \bar{u} , \bar{v} , and \bar{w} are wind fields and are obtained from a GCM; λ and ϕ are horizontal coordinate in the longitudinal and latitudinal direction, respectively; $\bar{\rho}$ is the air density, \bar{T} the temperature, η the cloud fraction, C_p the specific heat at constant pressure, Γ_d the adiabatic lapse rate, \bar{P} the precipitation flux, \bar{q}_v , \bar{q}_l , \bar{q}_i the mixing ratios for water vapor, cloud water, and cloud ice, respectively, and L_c , L_d and L_f the latent heat of condensation, sublimation, and melting, respectively. Also in these equations, \bar{Q}_c , \bar{Q}_i and \bar{Q}_R represent the condensational heating rates for cloud water, cloud ice, and the radiative heating rate, respectively, \bar{P} is the rate of autoconversion from cloud droplets to raindrops, \bar{E}_r is the evaporation of rain water, \bar{S}_{BF} and \bar{S}_s are the rates of change of the mass of ice particles due to the Bergeron-Findeison's processes and sublimation, respectively, and \bar{w}_l and \bar{V}_T are the bulk terminal velocities for cloud water and ice particles, respectively. In addition the vertical eddy flux and horizontal diffusion terms have been denoted by F_V^χ and F_H^χ , respectively, where χ can be \bar{T} , \bar{q}_v , \bar{q}_l or \bar{q}_i .

Because the radiative heating term (Q_R) appears only in the thermodynamic equation (2.1), radiative heating affects cloud fields through the temperature field. It is noted that the precipitation in Equation (2.5) is neither advected nor accumulated, since we have assumed all of the rain water which is converted from

the cloud LWC is precipitated out of the grid box immediately. The variables to be solved from the Equations (2.1)-(2.5) are \bar{T} , \bar{q}_v , \bar{q}_l , \bar{q}_i , \bar{P} and η . Thus, one more equation for the cloud cover, η , is needed to close the model equations.

The cloud cover, η , is derived based on an average of the specific humidities over clear and cloudy regions in the form

$$\bar{q} = \eta q_c + (1 - \eta) q_0 \quad ,$$

where q_c and q_0 are, respectively, the specific humidity in the cloudy and clear regions. After rearranging terms, the cloud cover is given by

$$\eta = \frac{\bar{q}_v/\bar{q}_s - q_0/\bar{q}_s}{q_c/\bar{q}_s - q_0/\bar{q}_s} \quad .$$

Here, we have introduced the grid-averaged saturation specific humidity, $\bar{q}_s(\bar{T})$, which is a function of the grid-averaged temperature, \bar{T} . For a stratiform cloud, the temperature within the cloud is approximately equal to the grid-averaged temperature, i.e., $q_c \cong \bar{q}_s(\bar{T})$. Thus,

$$\eta \cong \frac{(\bar{h} - h_0)}{(1 - h_0)} \quad , \quad (2.6)$$

where $\bar{h} = \bar{q}_v/\bar{q}_s$ and $h_0 = q_0/\bar{q}_s$ are the relative humidity in the grid average and in the clear region, respectively. The h_0 , threshold relative humidity, is a parameter to be prescribed to close the model equations.

The cloud cover in Equation (2.6) shows a linear relation between the relative humidity and cloud cover. A similar relation was found in the empirical expression proposed by Smagorinsky (1960) for use in GCM, as well as the results derived by Krueger et al. (1989) in meso-scale modeling studies (Figure 2.1). The values of the threshold relative humidity in Smagorinsky (1960) are adopted in this study.

With the introduction of the threshold relative humidity ($h_0 < 1$), partial cloudiness in the grid box is allowed when the large-scale relative humidity is less

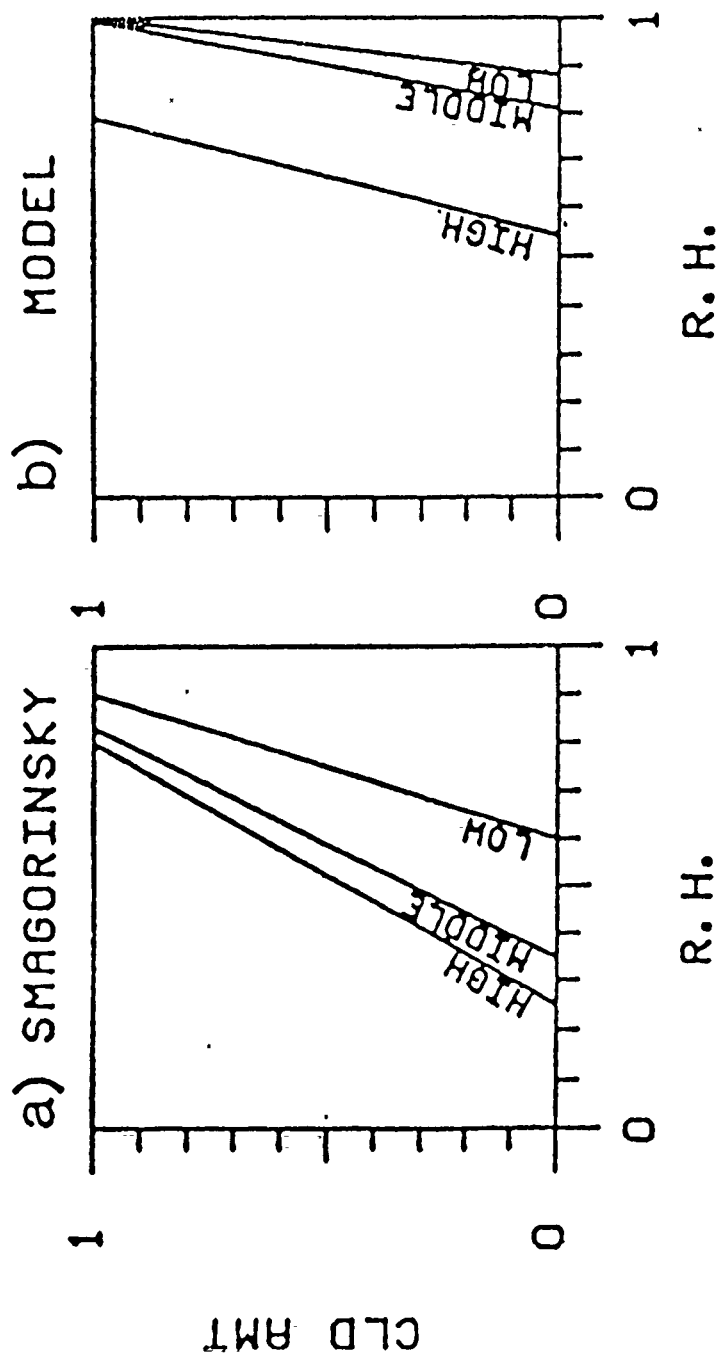


Figure 2.1. Linear relationship between cloud cover and relative humidity.

than 100% . The cloudy area and clear region in a grid box are denoted by η and $(1 - \eta)$, respectively. Condensation occurs in the cloudy area; evaporation takes place in the clear region. The raindrops formed in a given grid box are not subjected to evaporation within that box. Instead, the drops that fall through this layer from higher clouds may evaporate in the clear region of the box. Since the averaged terminal velocity of cloud droplets is on the order of 1 cm/s, which is close to the large scale vertical velocity, it would be expected that the terminal velocity of cloud droplets and vertical air motion roughly cancel each other in stratiform clouds. Therefore, vertical advection of cloud LWC in Equation (2.3) is omitted in the model calculations.

The vertical eddy terms are denoted as F_V^x , where x can be \bar{T} , \bar{q}_v , \bar{q}_l or \bar{q}_i . The F_V^x may be parameterized in terms of the Reynold stress, τ , as

$$F_V^x = \frac{\partial \tau_V^x}{\partial z} ,$$

where the Reynold stress is further expressed by

$$\tau_V^x = \bar{\rho} K_V^x \frac{\partial \bar{x}}{\partial z} ,$$

Here K_V^x denotes the vertical eddy diffusion coefficients for the element of x .

Following Washington and Williamson (1977), $K_V^x = K_V$ is assumed and given by

$$K_V = \begin{cases} 10^5 + 10^6 \{1 - \exp[1.2 \times 10^5 (\frac{\partial \bar{\theta}}{\partial z} - \gamma_c)]\} & \text{if } \frac{\partial \bar{\theta}}{\partial z} < \gamma_c \\ \frac{10^5}{1 + 40 \times R_i} + 10^3 & \text{if } \frac{\partial \bar{\theta}}{\partial z} > \gamma_c \end{cases} \quad (2.7)$$

where the countergradient lapse rate, γ_c , is taken to be 10^{-5} °K/cm, and $\bar{\theta}$ is a potential temperature and given by

$$\bar{\theta} = \bar{T} (P_0/P)^{\frac{R}{C_p}} ,$$

where P is air pressure and P_0 is a reference pressure at 1000 mb. The Richardson number, R_i , in Equation (2.7) is defined by

$$R_i = \frac{g}{T} \left[\left(\frac{\partial \bar{\theta}}{\partial z} \right) - \gamma_c \right] / \left[\left(\frac{\partial \bar{u}}{\partial z} \right)^2 + \left(\frac{\partial \bar{v}}{\partial z} \right)^2 + 10^{-12} \right] .$$

The horizontal diffusion term, F_H^χ , is defined as follows :

$$F_H^\chi = \frac{1}{a^2 \cos \phi} \left[\frac{1}{\cos \phi} \frac{\partial}{\partial \lambda} (\bar{\rho} K_H^\chi \frac{\partial \bar{\chi}}{\partial \lambda}) + \frac{\partial}{\partial \phi} (\bar{\rho} K_H^\chi \cos \phi \frac{\partial \bar{\chi}}{\partial \phi}) \right] ,$$

where K_H^χ is the horizontal diffusivity of the element of χ . The horizontal diffusivity is taken to be equal to the horizontal momentum diffusion coefficient, K_H .

According to Washington and Williamson (1977), the horizontal diffusion coefficient is given by

$$K_H = 2k_0^2 l^2 D ,$$

where k_0 is a proportionality constant determined empirically, l is equal to the horizontal grid size, and D is the deformation of flow which is given by

$$D = (D_T^2 + D_S^2)^{1/2} ,$$

where

$$D_T = \frac{1}{a \cos \phi} \left[\frac{\partial \bar{u}}{\partial \lambda} - \frac{\partial}{\partial \phi} (\bar{v} \cos \phi) \right] ,$$

$$D_S = \frac{1}{a \cos \phi} \left[\frac{\partial \bar{v}}{\partial \lambda} + \frac{\partial}{\partial \phi} (\bar{u} \cos \phi) \right] .$$

2.2 Cloud Microphysical Processes Simulated in the Model

The cloud microphysical processes simulated in the model are illustrated in Figure 2.2. Both the liquid and ice phase processes are included with the liquid phase on the left hand side and ice phase on the right hand side of the diagram. The liquid phase processes consist of condensation of water vapor into cloud liquid

water at temperatures warmer than -40°C , conversion of cloud liquid water into rain water by means of autoconversion, and precipitation of rain water onto the ground. The evaporation of cloud and rain water increases the water vapor. The parameterization of autoconversion rates follows the method that was first proposed by Sundqvist (1978) to combine the coalescence and accretion processes into a simple exponential form.

The ice phase processes include homogeneous nucleation of water condensate to cloud ice at temperatures colder than -40°C , and conversion of cloud ice to precipitating ice by the virtue of gravitational settling, which is a method of calculating the downward ice flux by integrating the mass and falling velocity of an individual ice crystal over the whole spectrum of ice crystals. The sublimation of cloud ice increases the water vapor. At temperatures above the freezing point, cloud ice melts into cloud water by the melting process.

An important link between the liquid and ice phases is so-called Bergeron-Findeison's processes. They are based on the fact that the saturation vapor pressure over ice is less than that over water. As a result, the ice crystals in a supercooled cloud grow by vapor diffusion at the expense of the supercooled liquid cloud droplets. Once generated by ice nucleation, ice crystals grow by deposition due to Bergeron-Findeison's processes and are depleted by sublimation as well as the gravitational settling. Above the freezing point, clouds consist of cloud water and contain no cloud ice. In the region 0° to -40°C , cloud water and cloud ice may coexist. At temperatures below -40°C , cloud ice dominates because of homogeneous nucleation.

Formation of rimed crystals, such as graupel and hail, is not considered in this model since it occurs in a small spatial scale. Furthermore, graupel and hailstone are observed more frequently in convective clouds than in large-scale stratiform clouds. The parameterizations of source and sink terms in the microphysical processes are

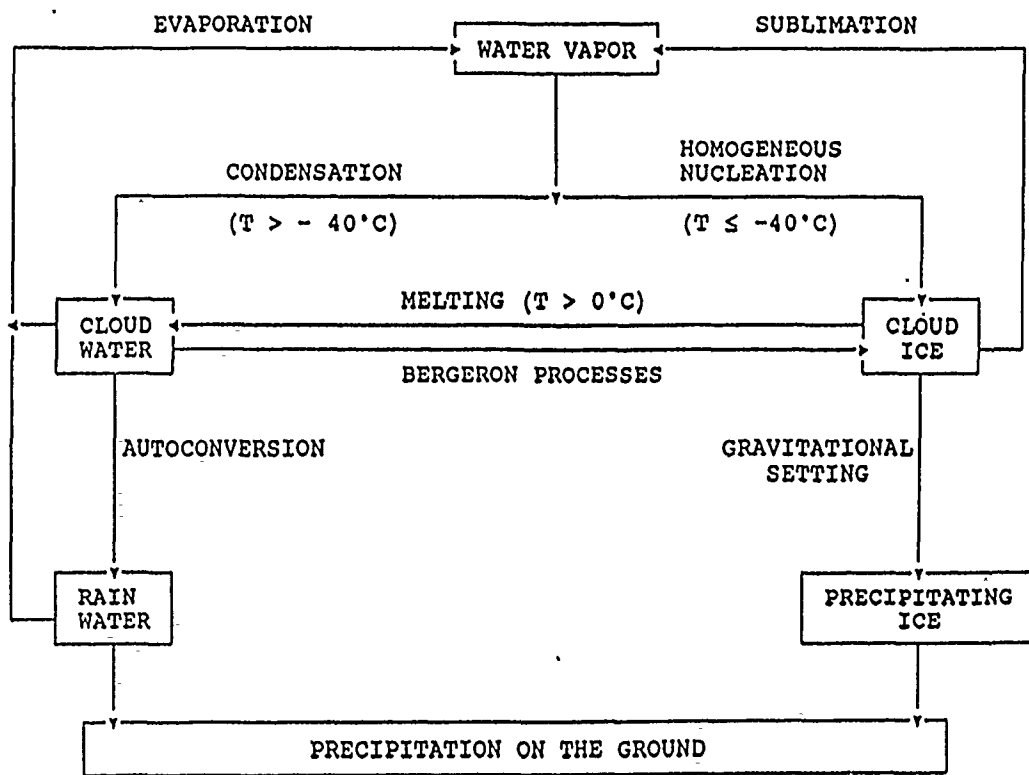


Figure 2.2. Cloud microphysical processes simulated in the model.

presented at greater length in Section 3.

2.3 Numerical Implementation

In the vertical, a 16-layer stretch z -coordinate is used in the cloud model. It has fine resolution in the lower levels, where clouds start to form, and coarse resolution in the upper levels of the model. The vertical grid structure and the distribution of variables are shown in Figure 2.3. In the figure, a dashed line denotes a layer; the interfaces between layers are referred to as levels. The values of \bar{w} , K_V^X , and \tilde{P} are placed at levels while the rest of variables are located at layers.

In the horizontal, the grid point space is characterized by 48 equally-spaced longitudinal points and 38 Gaussian latitudes, which is the same as the horizontal grid structure used in the Air Force Geophysics Laboratory (AFGL) GCM, and which provides the cloud model with initial data. As a result, the data interpolations in the horizontal between the two model are unnecessary. The horizontal grid space in the model is modified near the poles to maintain a nearly constant geographical distance between the grid points. This is achieved by decreasing the number of points around the latitude circles polarward of 60° so that the distance between points is close to that at 60° latitude.

The upstream scheme, a first order approximation in time and space, is utilized for numerically differencing the horizontal and vertical advection terms. The scheme is conditionally stable and its stability criterion follows the Courant-Friedrichs-Levy (CFL) condition, i.e., $C_{max}\Delta t / \Delta S$, where C_{max} is the maximum velocity in the computational domain, Δt is the time step and ΔS is the grid size. This criterion is easily satisfied in large scale models. For example, in the vertical, $\bar{w}_{max} \sim 10^0 \text{ cm/s}$, $\Delta t \sim 10^3 \text{ second}$, and $\Delta S \sim 10^4 \text{ cm}$, the criterion is much less than 1. The time step used in this study is 30 minutes. The radiation calculations are updated every 3 hours, i.e., the radiative heatings are calculated every 3 hours at every horizontal grid point and these values are used at each time step in the following 3-hour period.

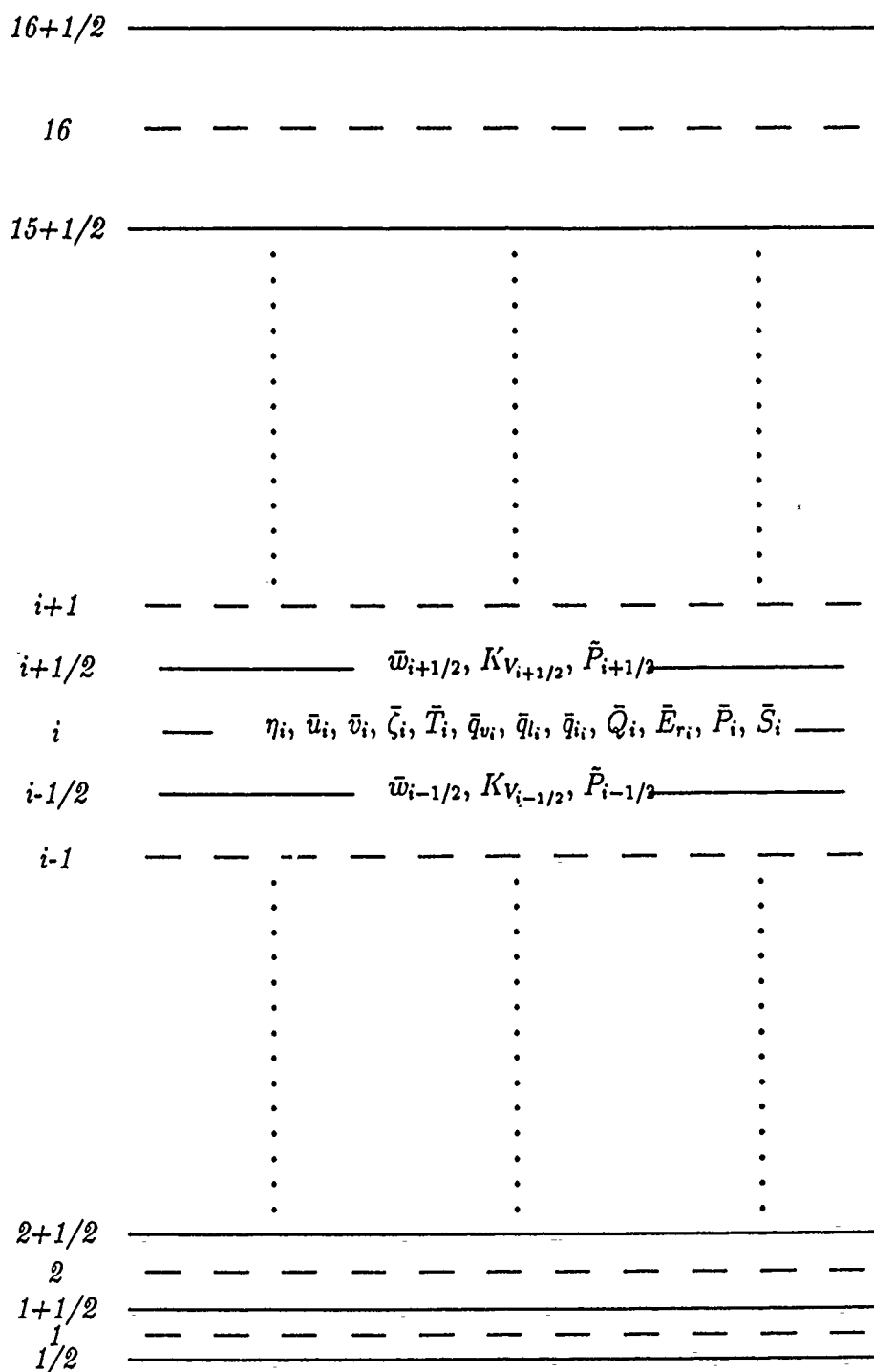


Figure 2.3. Cloud model vertical grid structure in Z-coordinate.

Advantages of the upstream scheme are to preserve the positive definiteness of the initial values and produce no dispersive ripples. These numerical ripples are inevitable in a higher-order accuracy scheme and may eventually lead to the instability of the whole scheme. In addition, the upstream scheme is less time consuming than high-order schemes. However, the upstream scheme is known to suffer from strong numerical diffusion. To overcome this problem, Smolarkiewicz (1983, 1984) introduced the 'antidiffusion velocity' into the basis of the upstream scheme and developed a positive definite advection scheme with small numerical diffusion. The developed scheme, sharing the same finite difference form as the upstream scheme, is second- or higher-order-accurate in space depending upon the implementation of the antidiffusion velocity as well as the number of iterations in the corrective steps. We plan to update the upstream scheme with the antidiffusion velocity included in the model in the future.

2.4 Radiative Transfer Parameterization

The radiative transfer parameterization program used in this study follows that developed at the University of Utah. It is based on a broadband method and involves the transfer of thermal IR and solar radiation in clear and cloudy regions. In a clear atmosphere, the entire IR spectrum is divided into five bands: three for H₂O, one for CO₂, and one for O₃ absorption. The parameterizations of these broadband IR emissivities were developed by Liou and Ou(1981), and Ou and Liou(1983). The solar spectrum consists of 25 bands: six for H₂O, one for CO₂, which overlaps the H₂O 2.7 μ m band, and 18 for O₃. Parameterizations of the broadband solar absorptivities for these absorbers were documented in Liou-etal. (1984).

In a cloudy atmosphere, low and middle clouds are treated as blackbodies in the IR radiative transfer calculation. The broadband IR emissivity, reflectivity, and transmissivity for high clouds as well as the broadband solar absorption, reflection,

and transmission values for various cloud types are computed based on the cloud LWC and IWC interactively generated by the cloud model. The cloud radiative properties are calculated based on the parameterizations developed by Liou and Wittman (1979). Accuracy of all the aforementioned parameterizations was verified via more comprehensive and exact radiative transfer calculations described in the report by Ou and Liou (1988).

A total cloud cover is used to obtain linearly weighted radiative fluxes between the clear and cloudy regions. By interactively providing the cloud cover, cloud LWC and IWC to the radiative transfer calculation, clouds can alter the radiative heating profiles, which in turn feed back to the clouds through the thermodynamic equation. Thus, cloud-radiation interaction through the medium of the cloud cover, cloud LWC and IWC is accomplished.

The radiative heating rate at level z is related to the divergence of the net fluxes and is given by

$$\frac{\partial T}{\partial t} = \frac{1}{\rho C_p} (\Delta F / \Delta z) \quad .$$

where Δz and ΔF are the model layer thickness and the net radiative flux difference between the layer top and bottom, respectively. This equation applies to both IR and solar heating rate calculations with downward solar flux and upward IR flux defined as positive. For the solar radiation in a cloud layer, the net flux density decreases from the the cloud top to the bottom because of cloud absorption. The absorbed radiate energy heats the cloud layer. Thus, solar radiative heating increases the atmospheric temperature. For a black cloud (a low or middle cloud), the IR radiative flux is proportional to the fourth power of the absolute temperature of the cloud. Since the atmospheric temperature usually decreases with height, the downward solar flux emitted from the atmosphere above a black cloud top is much smaller than that emitted upward by the black cloud. As a result, the net flux

near the cloud top is greater than zero and leads to strong IR cooling in the region. Similarly, there is IR heating near the cloud bottom. For a nonblack high cloud, the intracloud flux profile is determined by exponential interpolation between the cloud top and base fluxes.

Specification of the overlap that occurs between clouds layers is required for the calculation of radiative transfer in a radiation model, since only a cloud fraction for each model layer is determined by the cloud model. In this study, the model-generated clouds are strapped into three cloud decks. The parameterization of radiative flux exchanges in the three-deck cloudy atmosphere has been documented in Ou and Liou (1988).

For the AFGL GCM, low, middle, and high clouds fill, respectively, layers (4, 5, 6), layers (7, 8), and layers (9, 10), as indicated in Figure 2.4. Each deck of clouds is the respective averaged cloud cover of the model layers. For example,

$$\begin{aligned}\eta_l &= \frac{1}{3}(\eta_4 + \eta_5 + \eta_6) , \\ \eta_m &= \frac{1}{2}(\eta_7 + \eta_8) , \\ \eta_h &= \frac{1}{2}(\eta_9 + \eta_{10}) .\end{aligned}$$

Where η_l , η_m and η_h denote deck cloud cover for low, middle, and high clouds, respectively.

To determine the total cloud amount, we have assumed that clouds overlap each other in a statistically random manner, which is consistent with the model statistically diagnostic cloud cover scheme (Equation 2.6). Thus the total cloud cover may be given by

$$\eta_t = 1 - (1 - \eta_l)(1 - \eta_m)(1 - \eta_h) .$$

Where η_t is the total cloud fraction over a grid area.

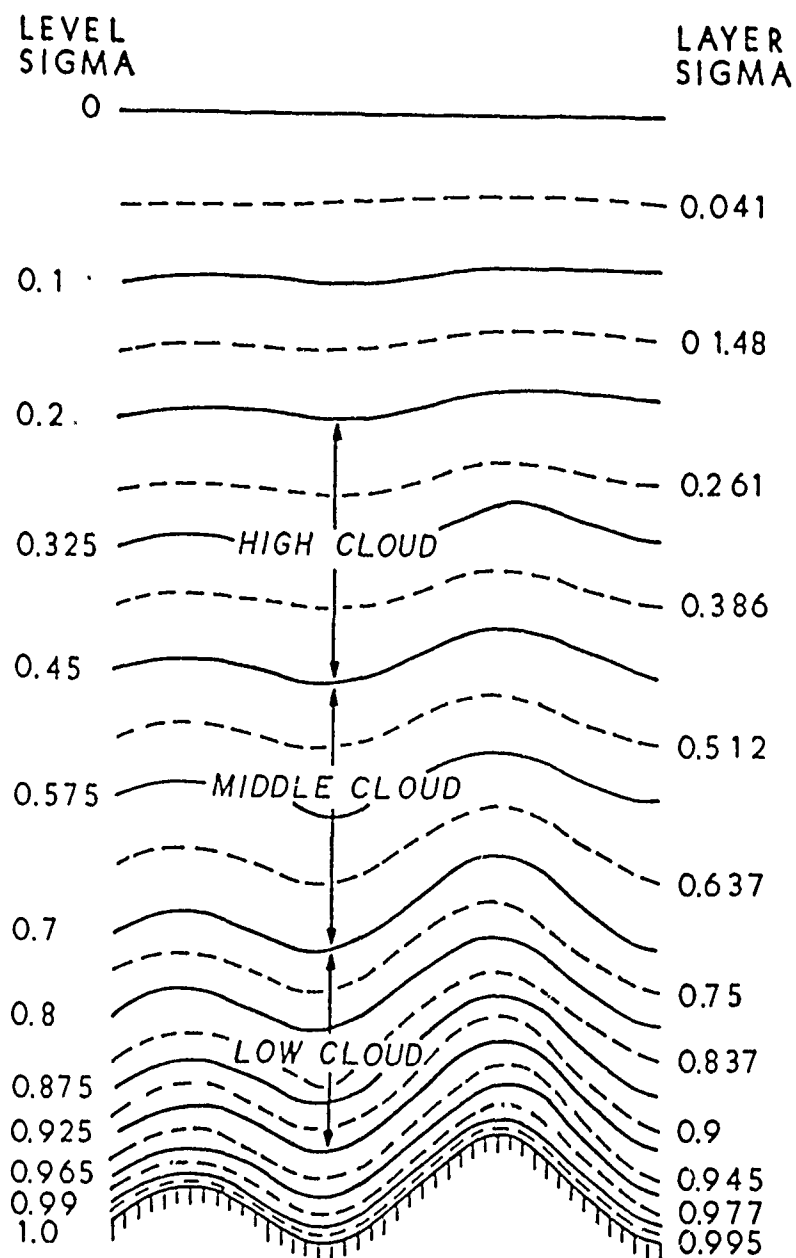


Figure 2.4. Definition of the σ -layers in the AFGL GCM.

For partly cloudy conditions, the radiative heating/cooling rate at each model layer is obtained by linearly weighting the percentages of the total cloud cover, η_t , and clear portion, $(1 - \eta_t)$, in the form

$$\left(\frac{\partial \bar{T}}{\partial t} \right)^{pc} = \eta_t \left(\frac{\partial \bar{T}}{\partial t} \right)^c + (1 - \eta_t) \left(\frac{\partial \bar{T}}{\partial t} \right)^{nc} ,$$

where the superscripts pc , c , and nc represent partly cloudy, cloudy, and clear conditions, respectively. This equation applies to both IR and solar heating rate calculations.

Section 3

BULK PARAMETERIZATIONS OF SOURCES AND SINKS OF MICROPHYSICAL PROCESSES

Since it is not practical in a large-scale cloud model to simulate detailed microphysical processes for each individual cloud particle, we have to relate these processes to bulk quantities, which represent the various sources and sinks for cloud water substances. In this study, the parameterizations of these bulk quantities generally follow Kessler (1969) and Sundqvist (1978) for the liquid phase and Starr and Cox (1985), Koenig and Murray (1976), and Heymsfield and Platt (1984) for the ice phase.

3.1 Liquid Phase

3.1.1 Condensation

Condensation transforms water vapor into cloud droplets. The condensation occurs as a result of saturated expanding air and may be related to the time rate of change of the saturation vapor pressure. Consequently, the condensational heating rate may be derived from the first law of thermodynamics, the Clausius-Clapeyron equation and the hydrostatic approximation as follow:

$$Q_c = \Gamma_d \frac{\bar{q}_s(\bar{T})}{R_a} \left[\frac{LR_a - C_p R_v \bar{T}}{C_p R_v \bar{T}^2 + \bar{q}_s L^2} \right] \bar{w} \quad .$$

The detailed derivation can be found in Appendix B. The condensation is strongly dependent on the vertical velocity, \bar{w} . As saturated air rises, i.e., $\bar{w} > 0$, condensation takes places and cloud forms, while depletion of clouds occurs with descending

saturated air. As one can see from Equation (2.1), condensation is allowed to take place at a relative humidity less than 100% but greater than the critical relative humidity. Otherwise, cloud cover becomes zero and no condensation occurs.

3.1.2 Autoconversion

Autoconversion is a process through which small cloud droplets merge into large raindrops. The parameterization of autoconversion follows the simple exponential form invented by Sundqvist (1978), as follows :

$$P = C_0 q_l \{1 - \exp[-(q_l/(\eta q_{lr}))^2]\} , \quad (3.1)$$

where C_0 and q_{lr} are parameters denoting, respectively, the typical time of conversion of droplets to raindrops, and a reference value of cloud LWC above which the conversion from cloud droplets to raindrops increases rapidly. These two values act a way similar to the rate of conversion and the parameterization of accretion discussed in Kessler (1969).

Kessler proposed two separate expressions for autoconversion due to coalescence and accretion of cloud water by raindrops, given as follows:

$$P_1 = K_1(q_l - a_1) , \quad (3.2)$$

$$P_2 = K_2(q_l q_r^{\frac{7}{8}}) , \quad (3.3)$$

where q_r and a_1 , respectively, are the rain water content and the threshold liquid water content below which there is too little cloud water to produce rain. Figure 3.1 demonstrates a comparison of the autoconversion rate used in the model with that proposed by Kessler(1969), i.e., Equations (3.2) and (3.3). In this comparison, we take $K_1 = C_0 = 10^{-3}\text{sec}^{-1}$, $a_1 = 10^{-3}$, $K_2 = 2.19$, and $q_r = 5 \times 10^{-5}$ ($\sim 2\text{mm/day}$). As shown in Figure 3.1, the two parameterizations give similar results. Apparently Sundqvist (1978) has adequately combined the above two equations for coalescence

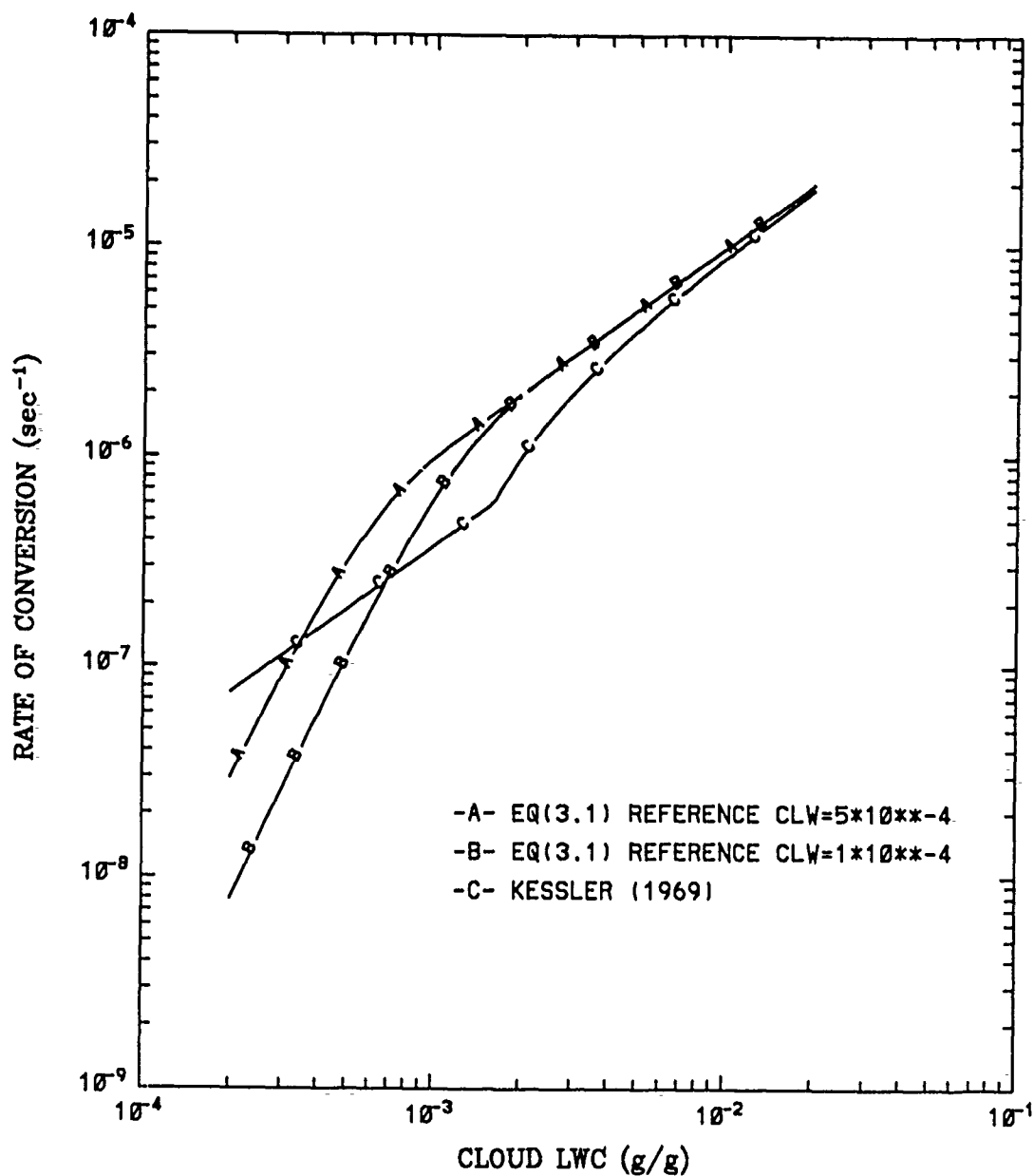


Figure 3.1. Comparison of the present parameterization of the autoconversion rate defined in Eq. (3.1) as a function of the liquid water content with that of Kessler(1969).

and accretion into a simple exponential form. This form has been successfully incorporated into the GCMs by Sundqvist (1981) , and Zheng and Liou (1986).

3.1.3 Evaporation of raindrops

The evaporation of raindrops may be derived from the combination of the Fick's law of the mass diffusion and the Marshall-Palmer raindrop size distribution. The size distribution is assumed to stay the same throughout the whole process of evaporation. The detailed derivation of raindrop evaporation is shown in Appendix C, and the formulation is given by

$$E_r = K_e(1 - h_0)(\tilde{P})^{0.42} , \quad (3.4)$$

where the evaporation rate constant is

$$K_e = 5.95 \times 10^{-3} q_s f .$$

It is noted that the ventilation coefficient, f , is included in the calculation.

Kessler (1969) followed the same rules but used a different approach to incorporate the ventilation effect. He derived the following form for the evaporation of rain:

$$E_r = 5.54 \times 10^{-4} \bar{q}_l (\bar{\rho} \bar{q}_r)^{0.65} \bar{\rho}^{-1} , \quad (3.5)$$

where the units for $\bar{\rho}$ and \bar{q}_l are in gm/m^3 . For the purpose of comparison, the raindrop evaporation in Equation (3.5) is further related to the precipitation flux as follows:

$$E_r = K'_e(1 - h_0)(\tilde{P})^{0.55} , \quad (3.6)$$

Where the evaporation rate constant is

$$K'_e = 7.84 \times 10^{-2} q_s ,$$

Figure 3.2 shows a comparison of the raindrop evaporation rates in Equations (3.6)

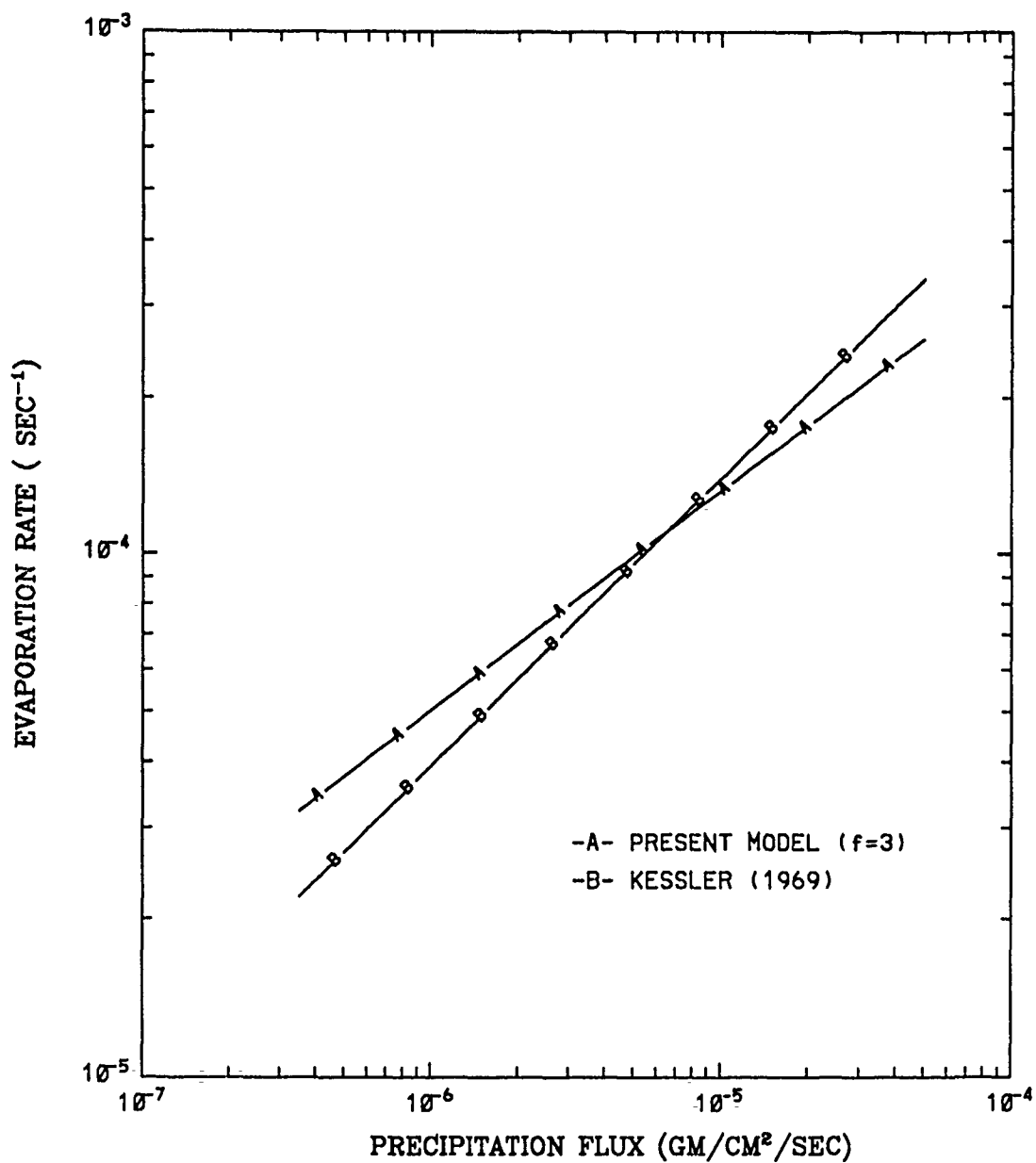


Figure 3.2. Comparison of the present parameterization of the evaporation rate, $E_r/q_s/(1 - h_0)$, based on Eq. (3.4) with that of Kessler (1969). The value of the ventilation factor used in the present parameterization is 3.

and (3.4) for $f=3$. The differences between the two curves are quite small for $\tilde{P}(z)$ between the normal range of large-scale precipitation of 10^{-2} and 10^{-1} gm/m²/sec.

3.2 Ice phase

The ice phase parameterizations include homogeneous/heterogeneous nucleation to generate ice crystals, depositional growth to simulate the Bergeron-Findeison's processes, sublimation and melting of ice crystals, and gravitational settling to deplete the ice crystals. The Bergeron-Findeison's processes occur primarily at temperatures between 0° and -40° C, while homogeneous nucleation dominates below -40° C. The parameterizations of these source and sink terms in the ice phase are described as follows.

3.2.1 Homogeneous nucleation

Homogeneous nucleation takes place whenever the condensation occurs at temperatures below -40° C. Homogeneous nucleation is analogous to the liquid water condensation process, and may be written in the form

$$Q_i = \Gamma_d \frac{\bar{q}_s(\bar{T})}{R_a} \left[\frac{LR_a - C_p R_v \bar{T}}{C_p R_v \bar{T}^2 + \bar{q}_s L^2} \right] \bar{w} \quad .$$

The homogeneous nucleation rate is a function of temperature and vertical velocity.

3.2.2 Heterogeneous nucleation

Heterogeneous nucleation forms ice crystals on active ice nuclei primarily at temperatures between 0° and -40° C. Based on the experimental work of Mason (1971), Mason and van der Heuvel (1959), and Koenig and Murray (1976), it is

assumed that the active ice-forming nuclei (IN) concentration may be expressed in terms of temperature as follow:

$$N = A_1 \exp\left\{-\frac{\ln(10)}{A_2} \max[(T - T_0), T^*]\right\} ,$$

where $A_1 = 1$, $A_2 = 4$, $T^* = 0^\circ \text{C}$, and T_0 is a threshold temperature, which is taken to be $em - 20^\circ \text{C}$. Here, it is assumed that when the saturated air temperature is lower than the T_0 , i.e., -20°C , the total number of IN remains the same as that at $T = -20^\circ \text{C}$, as shown in Figure 3.3.

The heterogeneous nucleation rate of ice crystals, S_h , may be given by

$$S_h = m_0 \frac{dN}{dt}$$

where m_0 is the mass of a newly nucleated ice crystal, prescribed as 10^{-11} gram, which is equivalent to an ice sphere with a diameter of $2.77 \mu m$ (Koenig and Murray, 1976), and

$$\frac{dN}{dt} = \begin{cases} \frac{N_{t+\Delta t} - N_t}{\Delta t} & \text{if } T \geq -20^\circ \text{C} \\ 0 & \text{if } T < -20^\circ \text{C} \end{cases}$$

Here, $N_{t+\Delta t}$ and N_t are the IN concentrations at consecutive time steps of $t + \Delta t$ and t , respectively.

3.2.3 Bergeron-Findeison's processes

The Bergeron-Findeison's processes transform cloud water into cloud ice at temperatures between 0° and -40°C . They are based on the depositional growth of cloud ice at the expense of cloud water. The depositional rate of ice crystals follows that developed by Koenig (1971).

For a single ice crystal, Koenig (1971) derived an equation for the depositional growth of ice based on the mass diffusion law and the electrostatic analogy (Hallett,

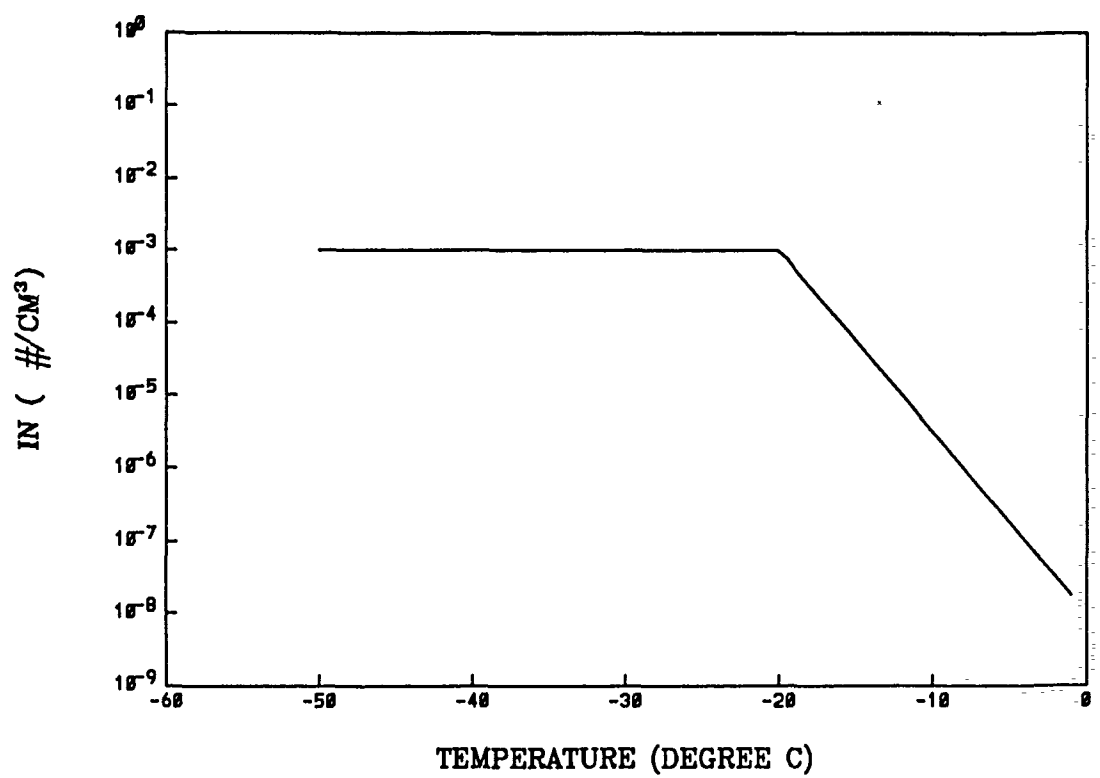


Figure 3.3. Dependence of ice nucleus (IN) concentration on temperature.

1965). The growth rate is a function of temperature because of the strong temperature dependence of saturation vapor pressure over water and ice. Koenig showed that the deposition rate of ice crystals as a function of temperature has two maxima at -5° and -15° C. This result agrees qualitatively with experimental values derived by Byers (1965).

To simplify the complicated vapor diffusion equation, Koenig (1971) developed a simple equation using two temperature-dependent parameters to describe the crystal vapor diffusion growth rate as a function of mass. The equation is written as follows:

$$\frac{dm}{dt} = a_3 m^{a_4} \quad , \quad (3.7)$$

where a_3 and a_4 are temperature-dependent parameters listed in Table (3.1), and m is the mass of the crystal in grams. Figure 3.4 illustrates the curves of a_3 and a_4 as functions of temperature. The maxima at -5° and -15° C, noted previously, are also present on these curves.

The bulk quantity of the ice crystal depositional rate, denoted as S_d , may be derived from Equation (3.7) by multiplying both sides by N , as follows:

$$\begin{cases} \frac{d}{dt}(\bar{\rho}\bar{q}_i) = f_l N^{1-a_4} a_3 (\bar{\rho}\bar{q}_i)^{a_4} \\ f_l = \bar{q}_l / (\bar{q}_l + \bar{q}_i) \end{cases} \quad (3.8)$$

where f_l is the cloud liquid fraction serving as an adjustment factor, which allows for more cloud water resulting in higher ice crystals growth rates. In addition, growth is stopped if there is no cloud water to supply water vapor. Figure 3.5 illustrates the ice crystal depositional rate as a function of temperature for different values of cloud IWC($\bar{\rho}\bar{q}_i$). It is noted that the maximum depositional rate occurs at -15° C, and the local maximum is at -5° C, and the local minimum is at -8° C. As a matter of fact, the maximum growth occurred at -15° C is due to a large vapor pressure difference and a large capacitance value at this temperature. This maximum ice growth at -15° C is evident in our numerical results shown in Section 5.

Table 3.1. Values of parameters a_3 and a_4 as functions of temperature.

[After Koenig (1972)]

Temperature	a_3	a_4
0°	0	0
-1°	0.7939×10^{-7}	0.4006
-2°	0.7841×10^{-6}	0.4831
-3°	0.3369×10^{-5}	0.5320
-4°	0.4336×10^{-5}	0.5307
-5°	0.5285×10^{-5}	0.5319
-6°	0.3728×10^{-5}	0.5249
-7°	0.1852×10^{-5}	0.4888
-8°	0.2991×10^{-6}	0.3894
-9°	0.4248×10^{-6}	0.4047
-10°	0.7434×10^{-6}	0.4318
-11°	0.1812×10^{-5}	0.4771
-12°	0.4394×10^{-5}	0.5183
-13°	0.9145×10^{-5}	0.5463
-14°	0.1725×10^{-4}	0.5651
-15°	0.3348×10^{-4}	0.5813
-16°	0.1725×10^{-4}	0.5655
-17°	0.9175×10^{-5}	0.5478
-18°	0.4412×10^{-5}	0.5203
-19°	0.2252×10^{-5}	0.4906
-20°	0.9115×10^{-6}	0.4447
-21°	0.4876×10^{-6}	0.4126
-22°	0.3473×10^{-6}	0.3960
-23°	0.4758×10^{-6}	0.4149
-24°	0.6306×10^{-6}	0.4320
-25°	0.8573×10^{-6}	0.4506
-26°	0.7868×10^{-6}	0.4483
-27°	0.7192×10^{-6}	0.4460
-28°	0.6513×10^{-6}	0.4433
-29°	0.5956×10^{-6}	0.4413
-30°	0.5333×10^{-6}	0.4382
-31°	0.4834×10^{-6}	0.4361

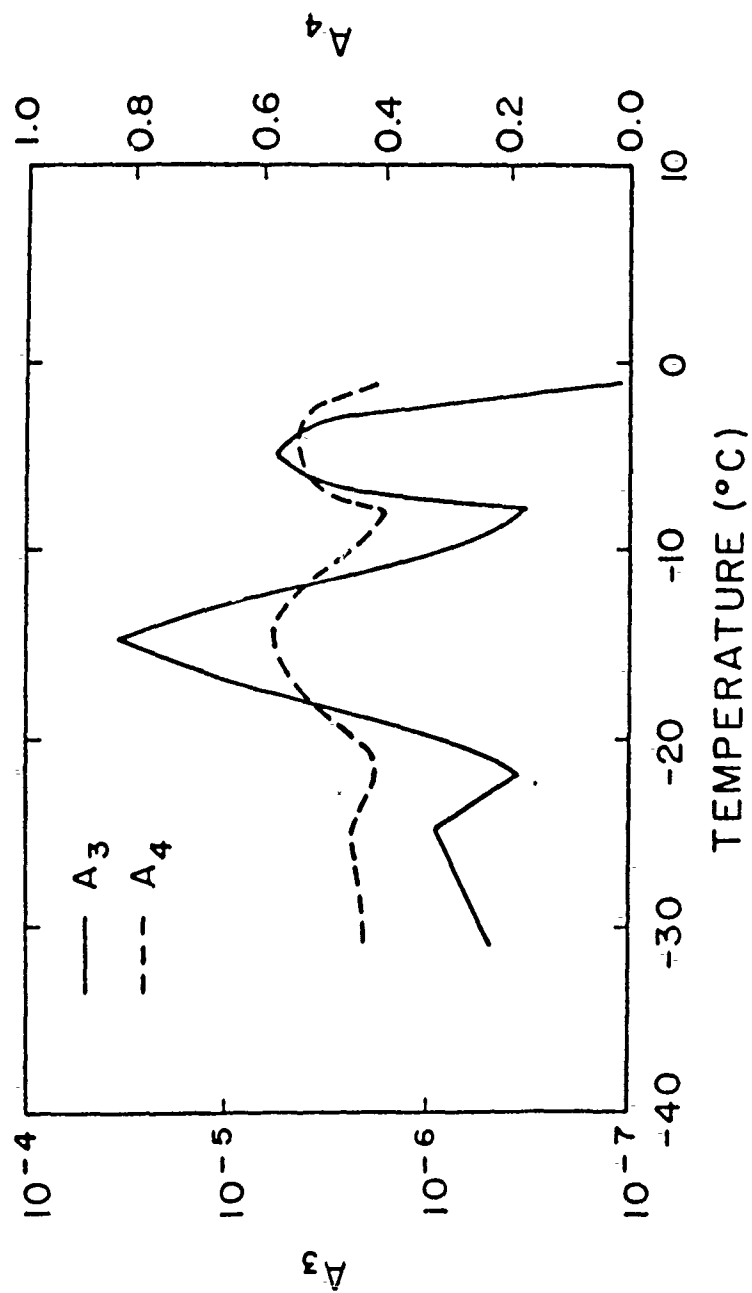


Figure 3.4. Temperature dependence of coefficients a_3 and a_4 defined in Eq. (3.7).

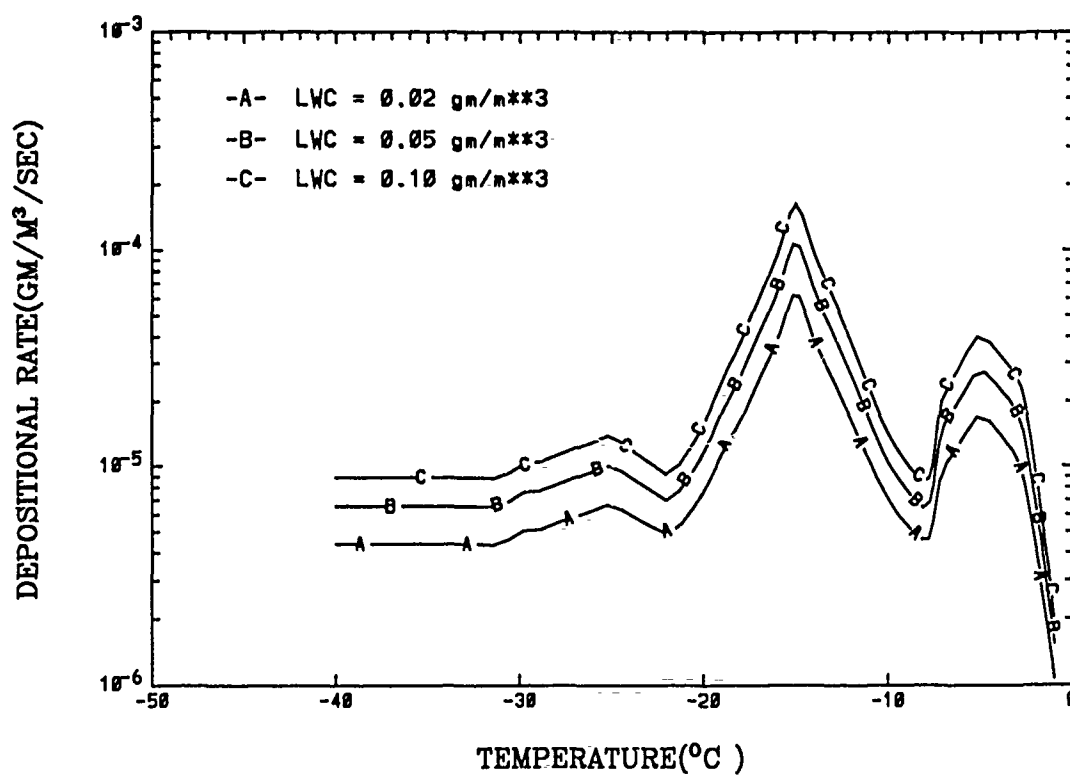


Figure 3.5. Ice crystal depositional rate as a function of temperature for three different cloud IWCs.

3.2.4 Sublimation and melting of ice crystals

The parameterization of the rate of sublimation is based on the work proposed by Koenig and Murray (1976) in the form

$$\bar{S}_s = 0.1037 (\bar{\rho} \bar{q}_s) (1 - h_0) (\bar{\rho} \bar{q}_i)^{0.65} . \quad (3.9)$$

This expression is similar to the expression for the evaporation of rains denoted in Equation (3.4). Figure 3.6 demonstrates the ice crystal sublimation rate as a function of cloud IWC($\bar{\rho} \bar{q}_i$) for three different temperatures with $h_0 = 0.85$.

At temperatures above 0°C, cloud ice crystals are assumed to melt instantaneously back to cloud water.

3.2.5 Gravitational settling

Gravitational settling is an important sink for cloud IWC. Therefore, it is desirable to have a representative (mean-volume-weighted) downward flux of ice water. Following Starr and Cox (1985), the downward ice flux may be expressed as

$$\bar{V}_T(\bar{\rho} \bar{q}_i) = \int_{L_{min}}^{L_{max}} n m v dL , \quad (3.10)$$

where n , m , and v are the ice crystal size distribution, mass and terminal velocity of an ice crystal, respectively, and L is the maximum dimension of an ice crystal. L_{min} and L_{max} are the minimum and maximum sizes of the crystals present. The cloud IWC may be further related to n and m as

$$\bar{\rho} \bar{q}_i = \int_{L_{min}}^{L_{max}} n m dL . \quad (3.11)$$

In order to calculate the downward ice flux, the size distribution(n), mass(m), and terminal velocity(v) for the precipitating ice crystals need to be specifically expressed in terms of the maximum dimension of the ice crystals, i.e., L .

The size distributions of ice crystals in mid-latitude cirrus clouds were measured and documented by Heymsfield (1977) using an optical probe. Based on those

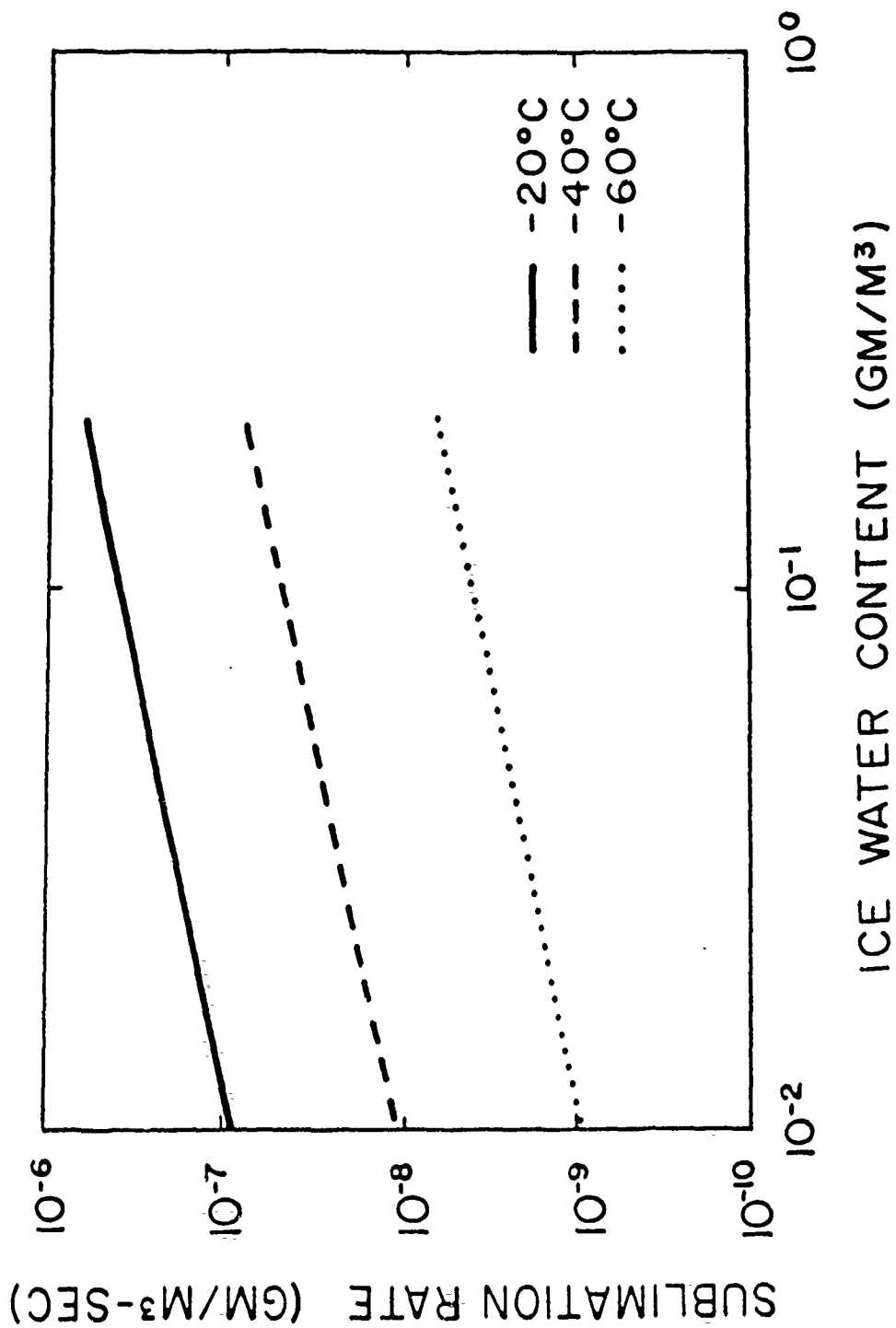


Figure 3.6. Ice crystal sublimation rate as a function of cloud IWC for three different temperatures.

Table 3.2. Parameterized coefficients for cirrus particle size distribution.

[After Heymsfield and Platt (1984)]

Temperature range	a_n	b_n	Mean IWC
$-20^\circ \sim -25^\circ$	1.40×10^2	-2.56	0.027 g/m^3
$-25^\circ \sim -30^\circ$	1.75×10^2	-2.51	0.025 g/m^3
$-30^\circ \sim -35^\circ$	1.30×10^2	-2.21	0.0175 g/m^3
$-35^\circ \sim -40^\circ$	2.50×10^2	-2.29	0.0126 g/m^3
$-40^\circ \sim -45^\circ$	2.55×10^1	-3.23	0.0034 g/m^3
$-45^\circ \sim -50^\circ$	1.40×10^1	-3.15	0.0025 g/m^3
$-50^\circ \sim -55^\circ$	7.00×10^0	-3.83	0.0018 g/m^3
$-55^\circ \sim -60^\circ$	5.02×10^0	-3.85	0.0009 g/m^3

data, Heymsfield and Platt (1984) further averaged all spectra of crystals within every 5°C temperature interval ranging from -20°C to -60°C . Therefore, the ice crystal size distributions in terms of the maximum dimension of ice crystals were parameterized for different temperature ranges.

The size distributions are written in the form

$$n = a_n L^{b_n} , \quad (3.12)$$

where n is the number concentration ($\text{m}^{-3} \mu\text{m}^{-1}$) and L is the particle dimension (μm). The a_n and b_n are the intercept parameter and the slope, respectively, which are temperature dependent and given in Table (3.2). As a first step, the parameters a_n and b_n are obtained from the temperature range of $-30^\circ\text{C} \sim -35^\circ\text{C}$, since the size distributions remained rather similar in the temperature range -20°C to -40°C .

The minimum length that the optical probe can measure is about $20 \mu\text{m}$. Small ice crystals less than $20 \mu\text{m}$ sizes could be missed by the measurement technique. Consequently, small ice crystal data were excluded from the analysis by Heymsfield and Platt (1984). For this reason, $20 \mu\text{m}$ is taken as the minimum length of ice crystals, L_{\min} , which is needed in the calculation of Equations (3.10) and (3.11).

Table 3.3. Parameterized coefficients for mass of an ice crystal.

[After Heymsfield (1972)]

Particle habit	a_m	b_m
Columns	1.35×10^{-10}	1.7
Bullet rosettes	4.4×10^{-14}	3.0
Plates	8.22×10^{-13}	2.5

3.2.5.1 Crystal mass and terminal velocity

Heymsfield (1972) has derived empirical expressions relating the maximum dimension of an ice crystal (L) to its corresponding mass and terminal velocity. Starr and Cox (1985) successfully incorporated these expressions into the calculation of downward ice flux due to gravitational settling in the cirrus cloud model, the purpose of which was partly to develop cirrus clouds parameterizations for use in large-scale cloud models. In this study, the parameterizations of a crystal mass and terminal velocity follow those used in Starr and Cox (1985).

The individual ice crystal mass, m , may be parameterized in terms of the maximum dimension of an ice crystal, L , as follows

$$m = a_m L^{b_m} , \quad (3.13)$$

where m and L are in units of grams and μm , respectively. The constants a_m and b_m associated with various ice crystal habits are given in Table (3.3).

The terminal velocity v in ms^{-1} of an ice crystal of maximum dimension L in μm is given by

$$v = a_v L^{b_v} . \quad (3.14)$$

The constants a_v and b_v are dependent on the ice crystal habit and size as given in Table (3.4). These coefficients were derived at an ambient pressure of 400 mb. For

Table 3.4. Parameterized coefficients for terminal velocity of an ice crystal.

[After Starr and Cox (1985)]

Size range (μm)	<i>Columns</i>	
	a_v	b_v
0-200	8.114×10^{-5}	1.585
200-400	4.995×10^{-3}	0.807
400-600	2.223×10^{-2}	0.558
600-800	4.352×10^{-2}	0.453
800-5000	3.833×10^{-2}	0.472
Size range (μm)	<i>Bullets</i>	
	a_v	b_v
0-200	5.666×10^{-5}	1.663
200-400	3.197×10^{-3}	0.902
400-600	2.977×10^{-2}	0.529
600-800	2.144×10^{-2}	0.581
800-5000	3.948×10^{-2}	0.489
Size range (μm)	<i>Plates</i>	
	a_v	b_v
0-200	1.0×10^{-3}	1.000
200-400	1.480×10^{-3}	0.926
400-600	9.500×10^{-4}	1.000
600-800	3.161×10^{-3}	0.812
800-5000	7.109×10^{-3}	0.691

an ice crystal at a given pressure p , Beard and Pruppacher (1969) suggested that its terminal velocity, $v(p)$, may be given by

$$v(p) = v(p^*) (p^*/p)^{\frac{1}{3}}$$

where p^* denotes a reference pressure level, and $v(p^*)$ is the terminal velocity of a crystal at the reference level. To obtain the terminal velocity at any given pressure, we simply apply the pressure adjustment to that derived from Equation (3.14).

3.2.5.2 Downward ice flux

Since the parameterizations of the ice crystals size distribution (n), ice crystal mass (m), and terminal velocity (v) are all parameterized in terms of the maximum dimension (L), the downward ice flux may be obtained by analytically integrating Equation (3.10), provided that the size of the largest crystals, L_{max} , is known. Since the lower limit, L_{min} , is set to be $20 \mu m$, as stated previously, the upper limit (L_{max}) may be determined from Equation (3.11) in the following way. Once $\bar{\rho}\bar{q}_i$ for the n -th time step is obtained, Equations (3.12) and (3.13) are substituted into Equation (3.11) to calculate L_{max} . Having determined L_{max} , the downward ice flux can be computed from Equation (3.10) as follows:

$$\bar{V}_T(\bar{\rho}\bar{q}_i) = \frac{a_n a_m a_v}{b_n + b_m + b_v + 1} [L_{max}^{(b_n+b_m+b_v+1)} - L_{min}^{(b_n+b_m+b_v+1)}] \quad (3.15)$$

The downward flux is the function of L_{max} , which in turn is the function of cloud IWC ($\bar{\rho}\bar{q}_i$). Consequently, the downward ice flux may be expressed in terms of cloud IWC.

Figure 3.7 demonstrates the computed ice downward flux as a function of cloud IWC for the temperature range of $-30^\circ \sim -35^\circ$ C. In this calculation, all crystals were assumed to be columns. When cloud IWCs varies from $5 \times 10^{-2} \text{ gm/m}^3$, the ice precipitation flux increases from 2×10^{-4} to about $10^{-2} \text{ gm/m}^2/\text{sec}$, which

corresponds to about 6.3 to 310 mm/yr. Comparing these values of ice precipitation with the annual global precipitation of 1000 mm estimated by Jaeger (1983), we note that gravitational settling is a significant process in the depletion of the IWC and the production of ice precipitation.

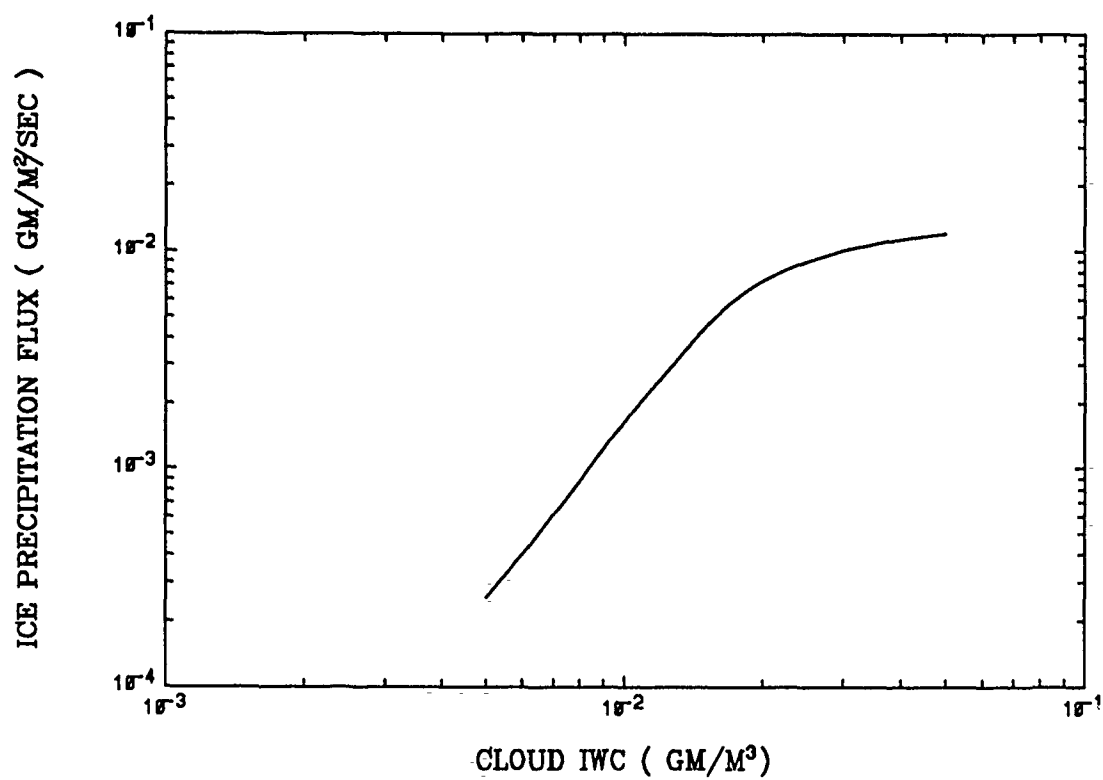


Figure 3.7. Downward ice flux as a function of cloud IWC for the temperature range of $-30^{\circ}\text{C} \sim -35^{\circ}\text{C}$.

Section 4

MODEL INPUT AND VERIFICATION DATASETS

4.1 Model input datasets

The analysis atmospheric data generated from the AFGL spectral global model at the 12Z of July 1-4, 1979, are used as input in the cloud model. These data contain temperature, specific humidity, and wind fields $(\bar{u}, \bar{v}, \bar{w})$ at all 12 σ -layers in the atmosphere plus the surface pressure and geopotential height. These analysis data were carried out at a rhomboidal 15 (R15) truncation which corresponds to a horizontal resolution of 38 and 48 grid points in the latitudinal and longitudinal, respectively.

In the vertical, since these GCM-generated input data are available at the σ -coordinate shown in Figure 2.4, it is necessary to perform vertical interpolations to obtain these values in the z -coordinate. A logarithmic interpolation was performed on the AFGL atmospheric profiles to map them from the σ levels to the height levels of the cloud model. All variables except temperature were converted in this manner. The temperatures were converted using a linear interpolation. Furthermore, the vertical velocity generated from the AFGL spectral model is in a σ -coordinate and is denoted as $\dot{\sigma}$. The conversion of $\dot{\sigma}$ to \bar{w} is accomplished based on the following relationship suggested by Kasahara(1974).

$$\bar{w} = \left(\frac{\partial \bar{z}}{\partial t}\right)_{\sigma} + \bar{V}_H \cdot \nabla_{\sigma} \bar{z} + \dot{\sigma} \frac{\partial \bar{z}}{\partial \sigma}$$

where \bar{z} is the geopotential height.

Figures 4.1 - 4.5 show the zonal mean values of temperature, specific humidity, and wind fields ($\bar{u}, \bar{v}, \bar{w}$) averaged over July 1-4, 1979. As one can see from Figure 4.1, the maximum tropospheric temperature occurs near 10° N. The tropospheric temperatures within the Antarctic Circle are much lower than those within the Arctic Circle. The mean temperature distribution in both hemispheres is characterized by an isobarically horizontal decrease poleward at all levels of the troposphere except above about 150 mb in the tropics, where the tropopause is the highest. Due to the lack of solar radiation within the Antarctic Circle in July, the overall pole-to-equator temperature contrast in the troposphere is much greater in the Southern Hemisphere than in the Northern Hemisphere. It is noted that a temperature inversion occurs in the Northern Hemisphere polar region.

Figure 4.5 shows the zonal average of vertical velocity in the z-coordinate, i.e., \bar{w} . The rising motions are associated with the equator and the middle latitudes in both hemispheres. In the vicinity of the equator, the upward motions are stronger in the Northern Hemisphere than in the Southern Hemisphere. The strongest vertical velocity occurs at the latitude near 10° N in the branch of rising motion of the Northern Hemisphere Hadley cell. The downward motions are found in the vicinities of the subtropic highs, i.e., 30° N and 20° S. The downward motions in the Southern Hemisphere are stronger than those in the Northern Hemisphere.

The radiative transfer model also requires values for the surface albedo, which is defined as the portion of the incoming solar radiation that is reflected by the earth's surface. A global dataset of surface albedo for July 1979 has been compiled by Griffin (1987) and Mitchell (1990). This dataset, shown in Figure 4.6, is used in this study. As one can see, the surface albedo can vary in value from a few percent (ocean surface) to more than 80% (snow or ice cover) with sharp changes occurring along the continental coastlines. The surface albedo is larger in the antarctic area than in the arctic region.

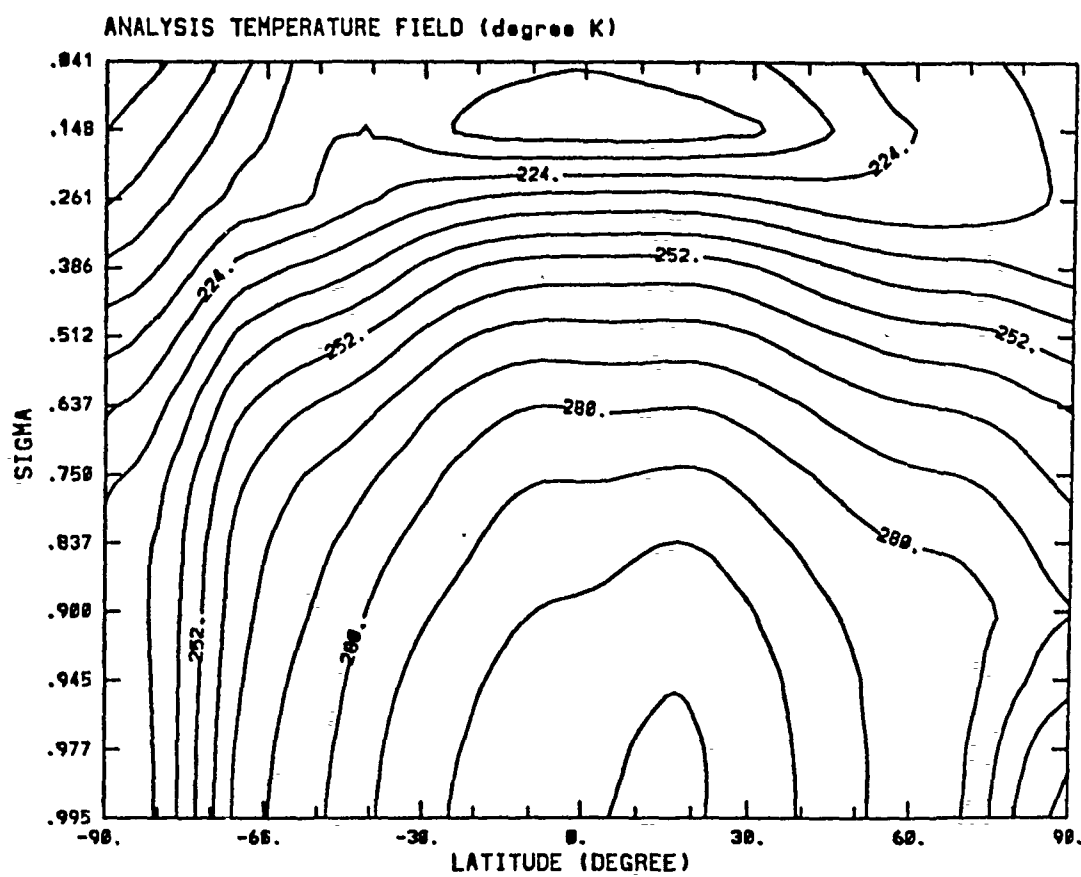


Figure 4.1. The analysis field of temperature averaged over July 1-4, 1979.

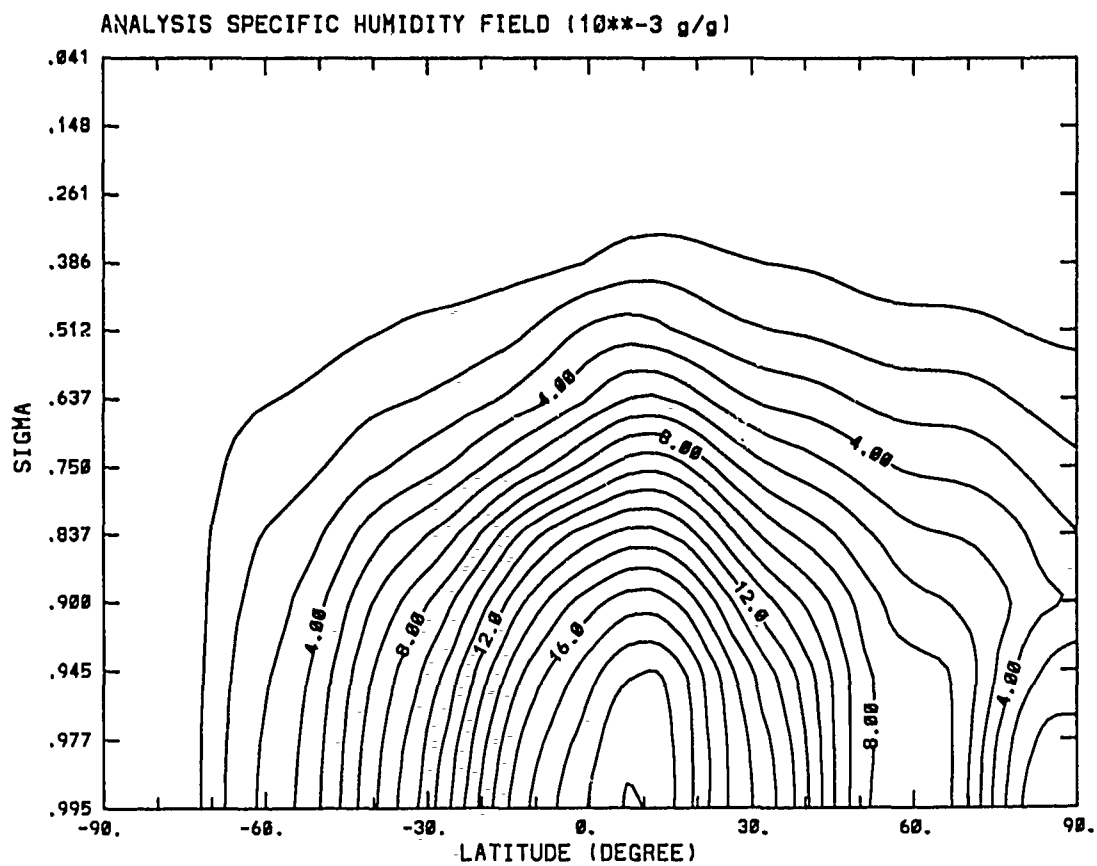


Figure 4.2. The analysis field of specific humidity averaged over July 1-4, 1979.

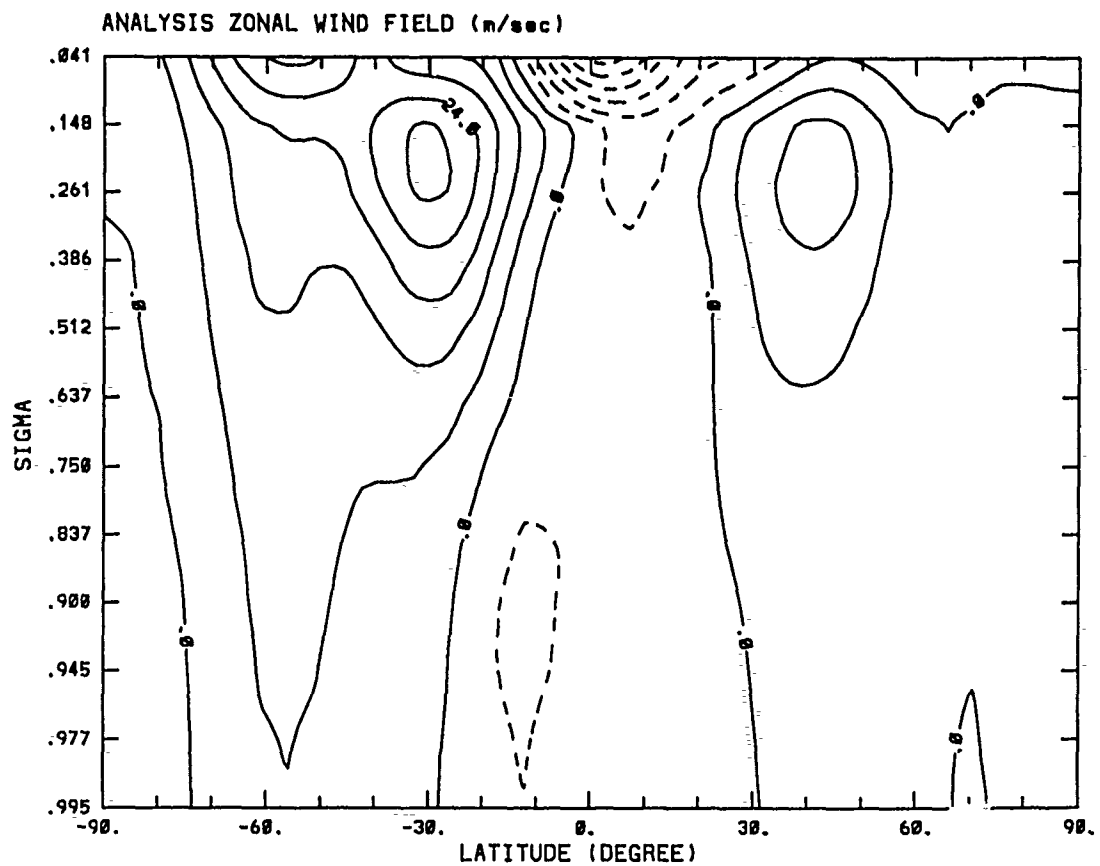


Figure 4.3. The analysis field of zonal wind averaged over July 1-4, 1979.

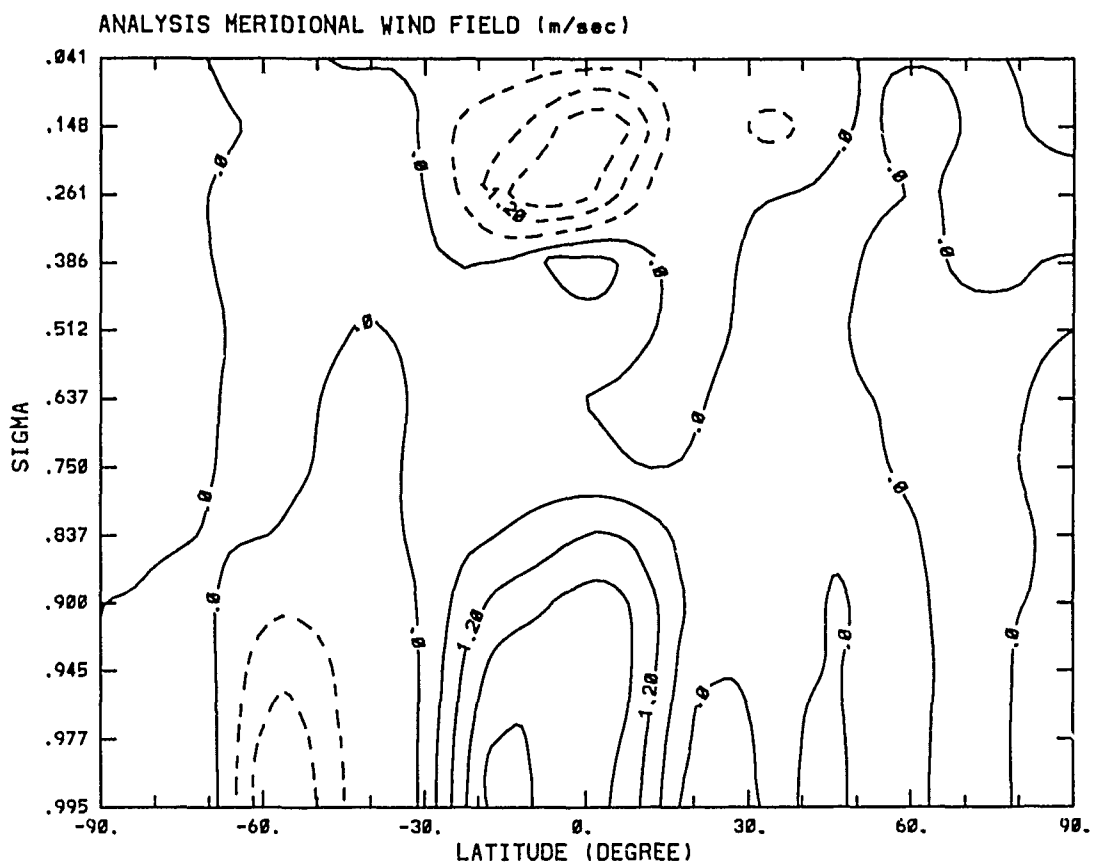


Figure 4.4. The analysis field of meridional wind averaged over July 1-4, 1979.

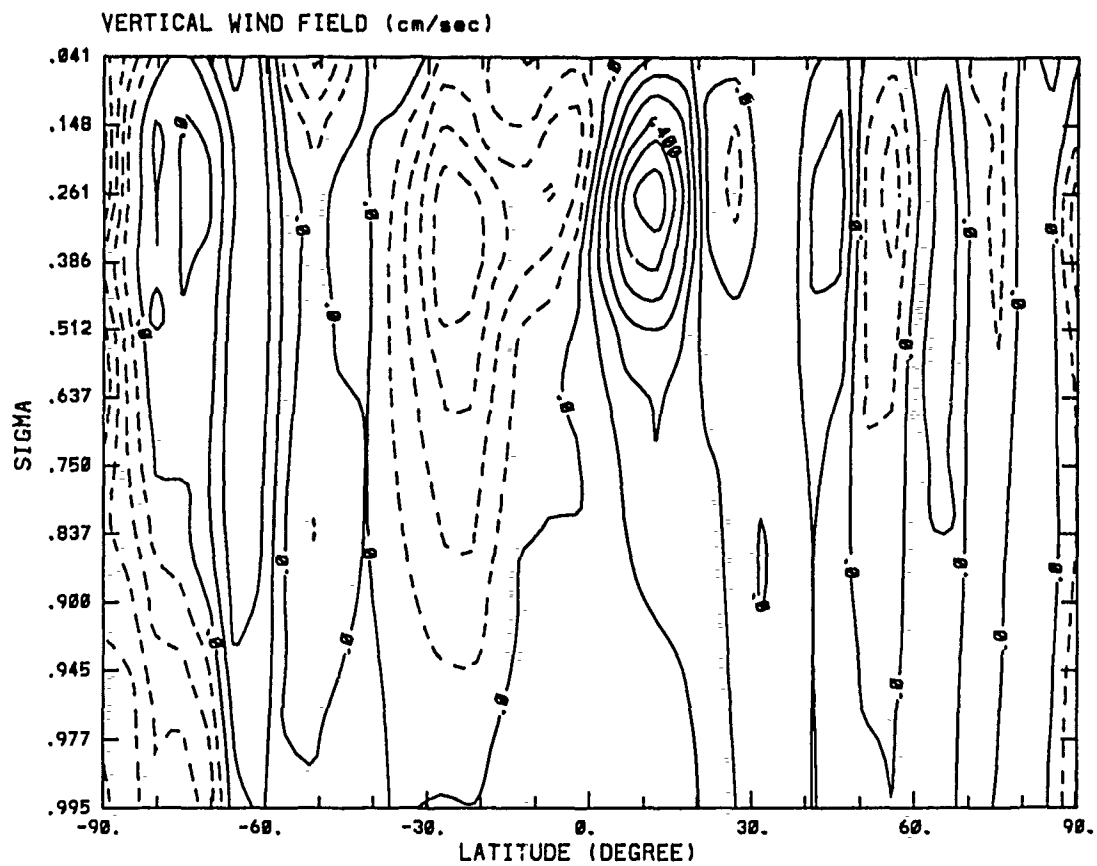


Figure 4.5. The analysis field of vertical velocity averaged over July 1-4, 1979.

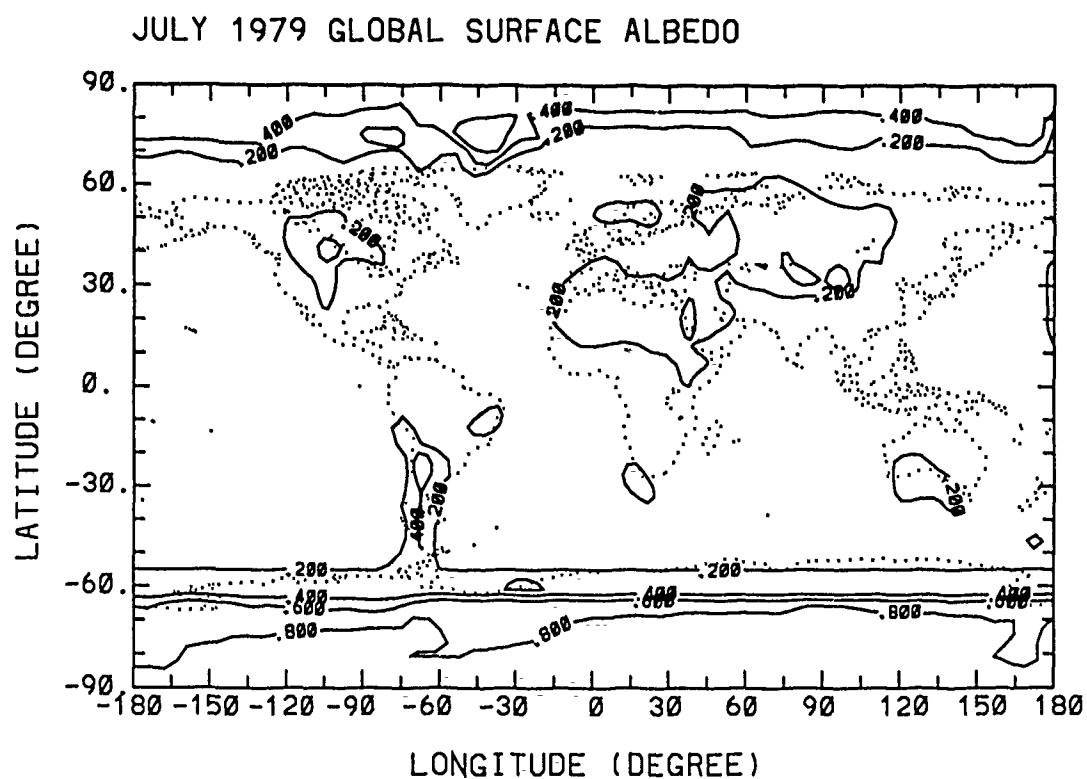


Figure 4.6. Monthly averaged surface albedo for July, 1979.

4.2 Verification datasets

It is one of the main objectives in this study to assess the model performance by verifying the predicted results against the verification datasets. Ideally, such datasets should provide simultaneous measurements of cloud cover, cloud LWC and IWC, and precipitation rates on a global basis.

Although ground-based cloud cover observations have been recorded for decades, the cloud amount obtained by a ground observer is subjective, tends to be overestimated (Hughes, 1984) and is less reliable at night. For multilayer cloud conditions, the cloud amounts associated with the upper cloud layers are frequently underestimated due to the lower clouds obscuring the upper clouds. It is the greatest intrinsic weakness of the ground-based cloud observations that most observational stations are unevenly gathered in high population areas and can provide only sparse observational data compared to satellite observations.

In contrast to surface-based observations, satellite observations are objective and the infrared sensors on board satellites can provide nighttime observations of as good a quality as those taken in daytime. Satellite observations tend to underestimate the cloud amounts associated with the lower cloud layers, which are obscured by the higher cloud layers. In addition, there is substantial error arising from the failure to distinguish between snow/ice surfaces and cloud tops, especially in the polar regions. Nevertheless, satellite observations provide an even global scope of cloud cover with resolution as high as 48 km by 48 km per pixel. This high resolution global coverage of satellite observed cloud cover makes satellite observations superior to other cloud observations.

4.2.1 3DNEPH cloud data

The Air Force Global Weather Central (AFGWC) high resolution three dimensional nephanalysis program, known as 3DNEPH, is the only operational cloud

analysis that combines both satellite and conventional reports. The 3DNEPH cloud information is derived from the DMSP (Defense Meteorological Satellite Program) satellites, which are sun-synchronous polar orbiting satellites with visual and infrared sensors.

3DNEPH generates high resolution global cloud information every 3 and 6 hours for the entire Northern and Southern Hemispheres, respectively. Each hemisphere is divided into 64 3DNEPH boxes as illustrated in Figure 4.7, with each box containing 4096 (64x64) grid points. The horizontal resolution of 3DNEPH is approximately 48 km at 60° latitude. The vertical grid consists of 15 layers of variable thickness which extend from the surface up to 17 km. 3DNEPH cloud analysis consists of cloud amount, cloud base, cloud top, and low, middle, high cloud types.

Based on 3DNEPH analysis, the global cloud climatologies for January and July 1979 were processed into appropriate formats for model verification. This work had been done mostly by Koenig (1985) and Griffin (1987), and partly by Mitchell (1990). The global distribution of cloud amount on July 1-4, 1979 is derived from the above cloud climatologies and used as the verification dataset for the cloud cover simulated in the model. In this dataset, the original 3DNEPH 15-layer cloud amount is combined to produce low, middle, high, and total (LMHT) cloud data bases. The low/middle cloud boundary is defined as terrain height + 2 km, while the middle/high cloud boundary is terrain height + the height of the -20° C isotherm. In addition, the high resolution (48 km) 3DNEPH horizontal grid points were mapped to the coarser Nimbus 7 ERB sub-target area grid structure (160 km).

It is important to recognize the limitation of 3DNEPH cloud analysis. A threshold method is employed to process satellite images to obtain the 3DNEPH cloud information. The visual image is compared with background brightness; The infrared image is compared with a threshold temperature, which is largely determined by the surface temperature. If an observed brightness temperature of a pixel is colder

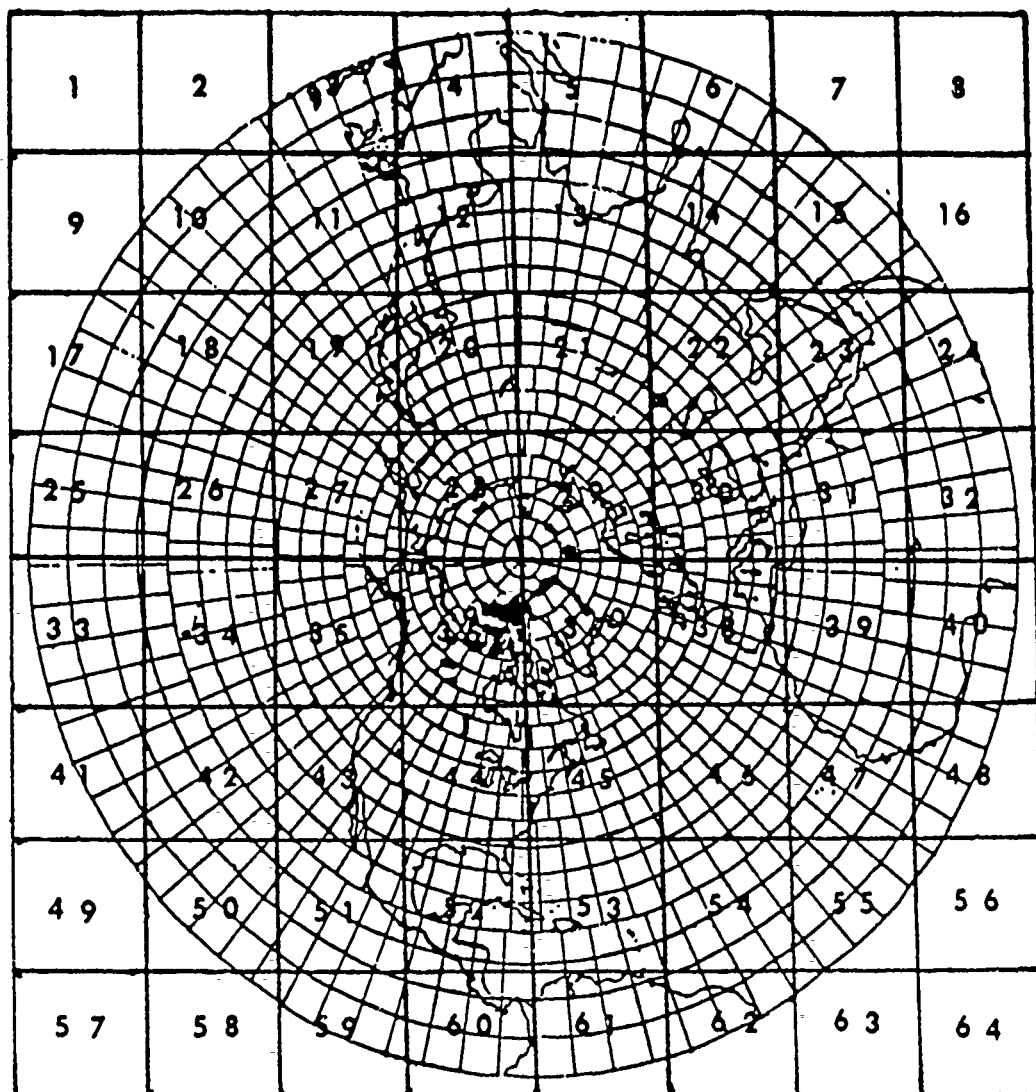


Figure 4.7. Configuration of the 3DNEPH grid over the Northern Hemisphere.

than the threshold temperature, then the cloudy condition is assigned to the pixel. Consequently, the cloud amount tends to be overestimated when the associated surface temperature is low, and underestimated when a temperature inversion is located in the region. This may be evident from the fact that 3DNEPH over- and underestimates cloud amounts in the wintertime and summertime polar regions, respectively (Henderson-Seller, 1986).

The high cloud amount is underestimated in both infrared and visual processes in 3DNEPH. Satellite infrared sensors tend to interpret high thin nonblack clouds as middle clouds and underestimates the high clouds amount. Since the transmissivity of these clouds is nonzero, infrared energy from below the cloud is transmitted by the cloud making it appears warmer than it actually is. The visual sensor also fails to detect small cloud amounts in the vicinity of areas of strong sun glint. Frequently, thin cirrus over a bright background (for example, over a desert) is not detected by the visual sensor.

The aforementioned problems become evident in attempts to use the 3DNEPH cloud data to verify the predicted cloud cover in Section 5. However, several intercomparisons of the cloud cover between 3DNEPH and other cloud retrieval techniques have been made (Koenig and Liou, 1983; Gordon et al., 1984; Hughes, 1984), and they indicated that the 3DNEPH total cloud cover appears to be reliable, except in the polar regions where all satellite retrieval methodologies tend to fail. Alternatively, the surface observational cloud climatology compiled by London (1957) is adopted in this study as a complementary verification data set for the polar regions.

4.2.2 Earth Radiation Budget (ERB) dataset

The Earth Radiation Budget (ERB) instrument aboard the Nimbus 7 satellite takes broadband measurements of the solar and terrestrial radiation reflected and

emitted by the earth-atmosphere system (Jacobowitz et al., 1978). The reflected solar radiation is referred as albedo, and the emitted infrared radiation is called outgoing longwave radiation (OLR). These OLR and albedo data have been examined and published in a number of articles (Jacobowitz et al., 1984 a,b; Arking and Vermury, 1984; Kyle and Vasanth, 1986), and appear to be an ideal earth radiation data base for use in the verification of large-scale cloud models. In this study, the observed albedo is converted to the net solar flux at TOA to be compared with the model-calculated net solar flux.

The archived ERB flux data tapes for the July, 1979 provided by the NASA ERB team was used in this study to validate the earth radiation budget, i.e., OLR and albedo, produced by the model. Since they are strongly modulated by the radiative effects of clouds, including cloud cover and cloud LWC/IWC, the ERB data have been widely used in large-scale cloud model verifications. (Slingo, 1986; Smith, 1990). In particular, when utilized together with 3DNEPH, the ERB data may provide valuable guidance on the cloud radiative properties of cloud LWC/IWC simulated in the model.

Nimbus 7 is a sun-synchronous polar orbiting satellite with equator crossings at local noon (ascending) and midnight (descending). Terrestrial radiation is measured by wide field-of-view (WFOV) and narrow field-of-view (NFOV) radiometers. The WFOV channels integrate the outgoing radiation over the entire earth's disc visible from the satellite; the NFOV channels measure the outgoing radiance from a number of directions with a mean resolution of 150 km by 150 km.

The NFOV radiance observations from Nimbus 7 are sorted into 2070 Target Areas (TAs), which cover the whole globe and are roughly of equal area. Each TA is approximately 500 km x 500 km and is bounded by latitude and longitude lines. There is a 4.5° interval between the latitude lines. For each latitude band, the longitudinal increments for a TA vary from 4.5° at the Equator to 120° near

the pole. Each TA is further divided into nine (3x3) Subtarget Areas (STAs). Each STA roughly corresponds to an area of 160x160 km². The exact boundaries for the 2070 TAs are shown in Table (4.1) and displayed on a Mercator projection in Figure 4.8.

To derive mean daily flux values of the earth radiation budget, angular dependence models and diurnal correction models are adopted. An angular dependence model converts the NFOV radiance measurement to a flux at TOA; the diurnal models are used to estimate the daily averaged albedo from a once a day observation. Errors involved in the angular model conversion are smaller than those in the diurnal models. Since the reflectivity is a function of the angle of incident radiation, the instant albedo measurement is not a good estimate of the mean daily albedo. Such errors were carefully examined and reduced in the NASA ERB data by Kyle et al., (1990).

4.2.3 Scanning Multichannel Microwave Radiometer (SMMR)

Monthly mean distributions of liquid water were derived from the Nimbus 7 SMMR observations over the oceans for the period November 1978 to November 1979 (Prabhakara and Short 1984). The liquid water estimate for the July, 1979 is applicable to the monthly average over an area approximately 400 km on a side ($3^{\circ} \times 5^{\circ}$, latitude/longitude). The liquid water derived includes vertically integrated amounts of liquid droplets in both clouds and rain. Since the ice-free sea surface emissivity is nearly constant, the liquid water verification data were limited to the oceans equatorward of 60° latitude. Over land, there is no climatological liquid water data on the global extent for comparison.

Liquid droplets in clouds and rain absorb and scatter microwave radiation. The microwave brightness temperatures, observed by the SMMR, are significantly modulated by liquid droplets in the atmosphere. These droplets produce a bright-

Table 4.1. Nimbus-7 ERB TA boundaries in longitudinal and latitudinal lines.

<u>Sequential Target No.</u>		<u>Latitude Limits</u>		<u>Longitude Interval*</u>
<u>Southern Hemisphere</u>	<u>Northern Hemisphere</u>	<u>Lower Limit</u>	<u>Upper Limit</u>	
956-1035	1036-1115	Equator	4.5	4.5
876-955	1116-1195	4.5	9.0	4.5
796-875	1196-1275	9.0	13.5	4.5
716-795	1276-1355	13.5	18.0	4.5
644-715	1356-1427	18.0	22.5	5.0
572-643	1428-1499	22.5	27.0	5.0
500-571	1500-1571	27.0	31.5	5.0
428-499	1572-1643	31.5	36.0	5.0
368-427	1644-1703	36.0	40.5	6.0
308-367	1704-1763	40.5	45.0	6.0
248-307	1764-1823	45.0	49.5	6.0
200-247	1824-1871	49.5	54.0	7.5
155-199	1872-1916	54.0	58.5	8.0
115-154	1917-1956	58.5	63.0	9.0
79-114	1957-1992	63.0	67.5	10.0
49-78	1993-2022	67.5	72.0	12.0
29-48	2023-2042	72.0	76.5	18.0
13-28	2043-2058	76.5	81.0	22.5
4-12	2059-2067	81.0	85.5	40.0
1-3	2068-2070	85.5	Pole	120.0

*For each latitude band, the longitude intervals start at the 0° meridian and progress west by the increments listed.

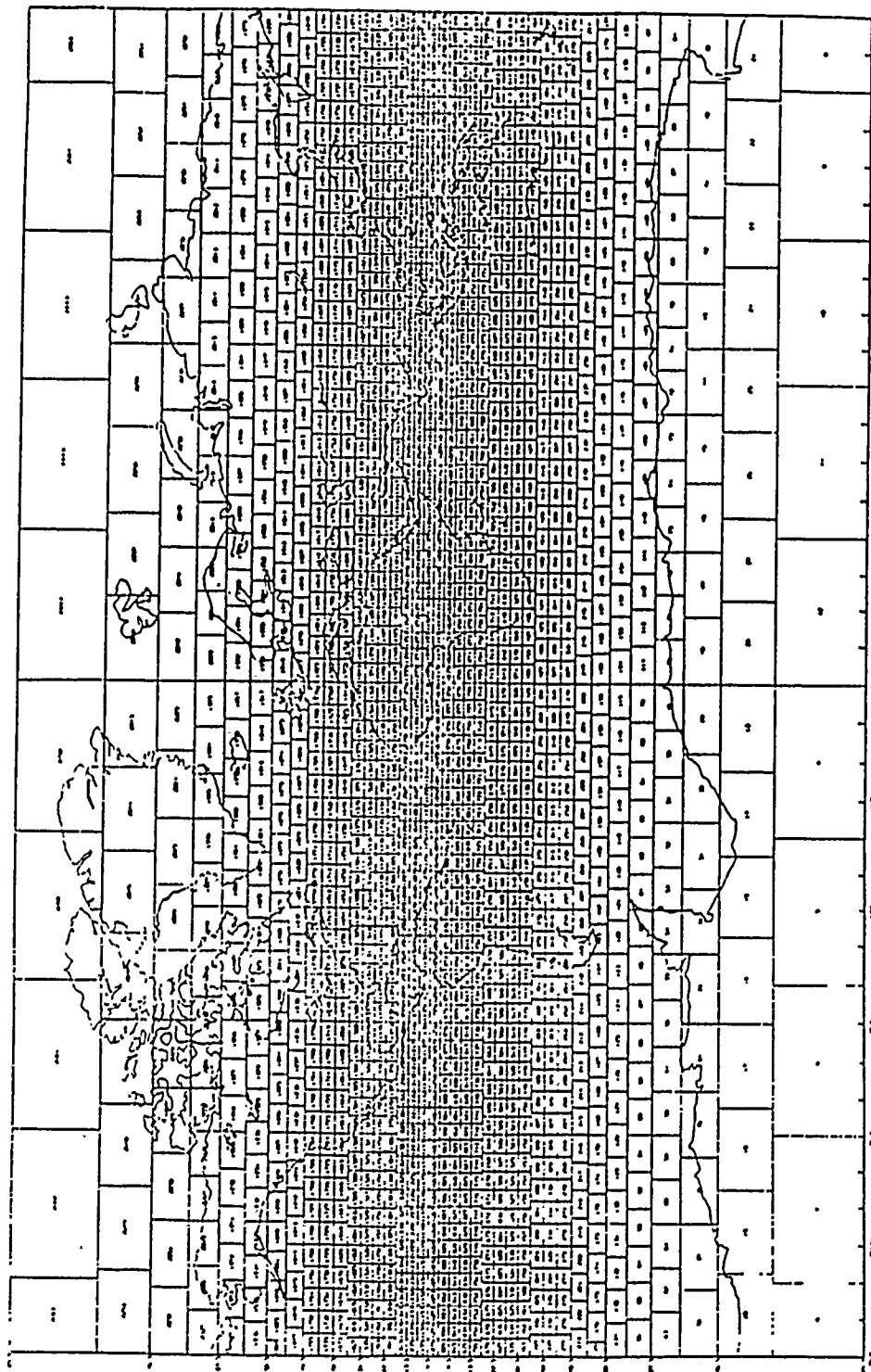


Figure 4.8. Nimbus-7 ERB global grid of 2070 target areas.

ness temperature change that increases significantly with increasing frequency. However, the Rayleigh approximation for rain drops breaks down as the frequency increases to some extent. As a result, SMMR brightness measurements at the high frequency channels, 18, 21 and 37 GHz, do not increase linearly with the LWC in the atmosphere. This can adversely affect the remote sensing of LWC. For this reason, only the lower frequency channels, 6.6 and 10.7 GHz, are used to derive the liquid content in the atmosphere.

Since there is no ground truth with which to compare, the accuracy of liquid water observations from SMMR is roughly estimated as $\sim 10 \text{ mg/cm}^2$ based on theoretical considerations (Prabhakara et al., 1983). However, by taking monthly averages, this accuracy may be improved to 5 mg/cm^2 (Prabhakara and Short, 1984). The temporal and spatial variation of liquid water is very great. For example, while instantaneous LWCs in deep precipitating clouds can be as high as 3000 mg/cm^2 , monthly average amounts over large areas rarely exceed 30 mg/cm^2 . This is a consequence of the relatively small spatial scales and short lifetimes of cloudiness. In addition, the SMMR observations seem to underestimate cloud LWC. Cloud IWC is transparent to microwaves at the SMMR frequencies.

The model input and verification datasets, including AFGL analysis data, ERB, 3DNEPH and SMMR, are summarized in Table (4.2).

Table 4.2. A summarized table for model input and verification datasets.

DATA SOURCES

Data Sets	Data Description	Comment
Analysis data on July 1, 12Z, 1979.	$\left. \begin{array}{l} \text{Temperature} \\ \text{Humidity} \\ \text{Wind field (u,v,w)} \end{array} \right\} \Rightarrow \left\{ \begin{array}{l} \text{Initial cloud cover} \end{array} \right.$	linear interpolation of analysis wind fields between July 1, 12Z and July 2, 12Z.
3DNEPH (Three-Dimensional Neph-analysis)	cloud amount (LMHT), cloud base, cloud height, and cloud types.	64 3DNEPH boxes box = 64 x 64 grid points grid reso. ~ 40 x 40 km**2
SMR (Scanning Multichannel Microwave Radiometer)	Vertically integrated liquid water contents over the oceans.	monthly average over an area approximately 400 x 400 Km**2
ERB (Earth Radiation Budget)	Outgoing Longwave Radiation and downward solar radiation at TOA observed by Nimbus-7.	sunsynchronous, polar orbiting, AN, DN. 2070 TA; T.A.=3x3 S.T.A. S.T.A. ~ 160 x 160 km**2

Section 5

MODEL PERFORMANCE AND VERIFICATION

5.1 Design of the Verification

In the development of any parameterization scheme, the prediction results must be carefully verified to assess the performance of the new scheme. A schematic illustration of the model verification is given in Figure 5.1. The large-scale cloud model was integrated for 96 hours with a time step of 30 minutes from the initial conditions taken at 12Z of July 1, 1979. The winds to circulate cloud-moisture are not predicted in the cloud model. Instead, they are prescribed as four sets of analysis wind fields on each 12Z of July 1 to 4, 1979. During the 96-hour model integration, each set of 12Z wind fields is employed at each time step for 24 hours. It is noted there is no cloud-radiation feedback to the dynamic structure in this study.

With input of the initial data and wind fields, the cloud model is capable of forecasting large-scale cloud cover and cloud LWC/IWC, which are interactively input into the radiation model. The radiation model calculates radiative heating/cooling rates based on the predicted cloud properties. The radiative heating/cooling rates, in turn, feed back to the cloud model through the thermodynamic equation, and ultimately modify the cloud fields. Therefore, cloud-radiation interaction through the medium of the cloud cover and cloud LWC and IWC is accomplished with the aid of the cloud model. In addition, the radiation model computes OLR and net solar flux at TOA to be compared with the ERB satellite observational data. In this study, the interactive radiation computations are undertaken every three hours,

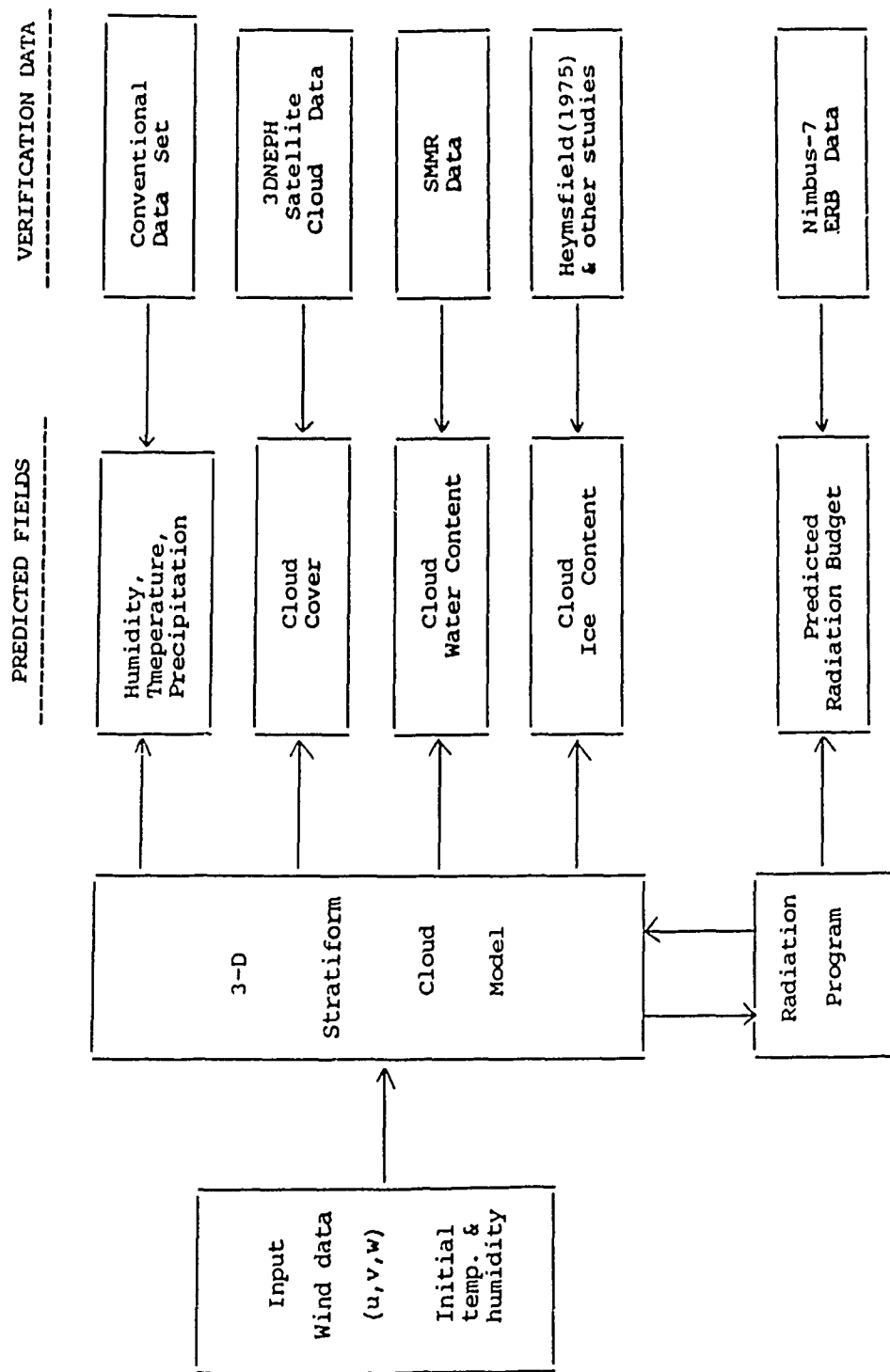


Figure 5.1. A schematic illustration of the model verification.

while the calculated heating/cooling rates are input in the cloud model at every time step during those three hours.

The simulated cloud cover, earth's radiation budget and cloud LWC and IWC are verified against 3DNEPH cloud cover, ERB and SMMR, as well as *in situ* observations and other model studies. However, there are some problems which make the use of satellite observations in model verification not entirely straightforward. For instance, verification datasets such as 3DNEPH and ERB are based on the daily average over local time, while the model simulation is evolved in Greenwich Mean Time (GMT). Allowing intercomparisons to be made between the satellite observations and model simulations, we have to average the model predicted fields over local time in order to obtain daily averaged model results. Unless specified, all of the results including satellite observations and model simulation are averaged over July 3-4, 1979. That is most of the results shown in this and latter section are presented as a 2-day average of July 3 and 4.

5.2 Initial Data

The analysis data on 12Z, July 1, 1979 for temperature, specific humidity, and winds ($\bar{u}, \bar{v}, \bar{w}$), shown in Figures 5.2 - 5.6, are used as initial values to perform a 96-hour model simulation. Data for the cloud LWC/IWC are not available for initial values and LWC/IWC are set as zero initially.

The initial cloud cover may be deduced from the initial temperature and specific humidity. The initial temperature is used to derive the saturation specific humidity, denoted by $\bar{q}_s(\bar{T})$, which is defined as follows:

$$\bar{q}_s(\bar{T}) \cong \frac{\epsilon e_s(\bar{T})}{P}$$

where $\epsilon = 0.622$ and $e_s(\bar{T})$ is a saturation vapor pressure, which is related to large-scale temperature by the Clausius-Clapeyron equation

$$e_s(\bar{T}) = 0.622 \times \exp\left(\frac{1}{\bar{T}} - \frac{1}{273}\right)$$

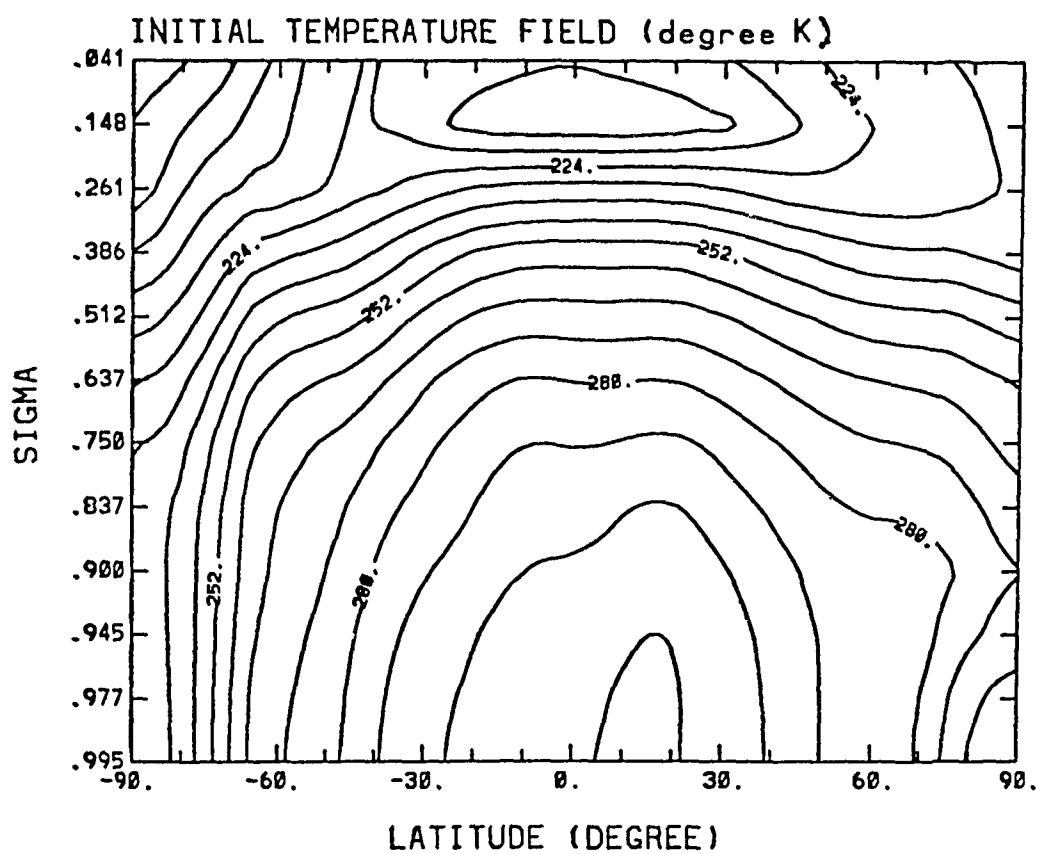


Figure 5.2. The zonal mean field of initial temperature.

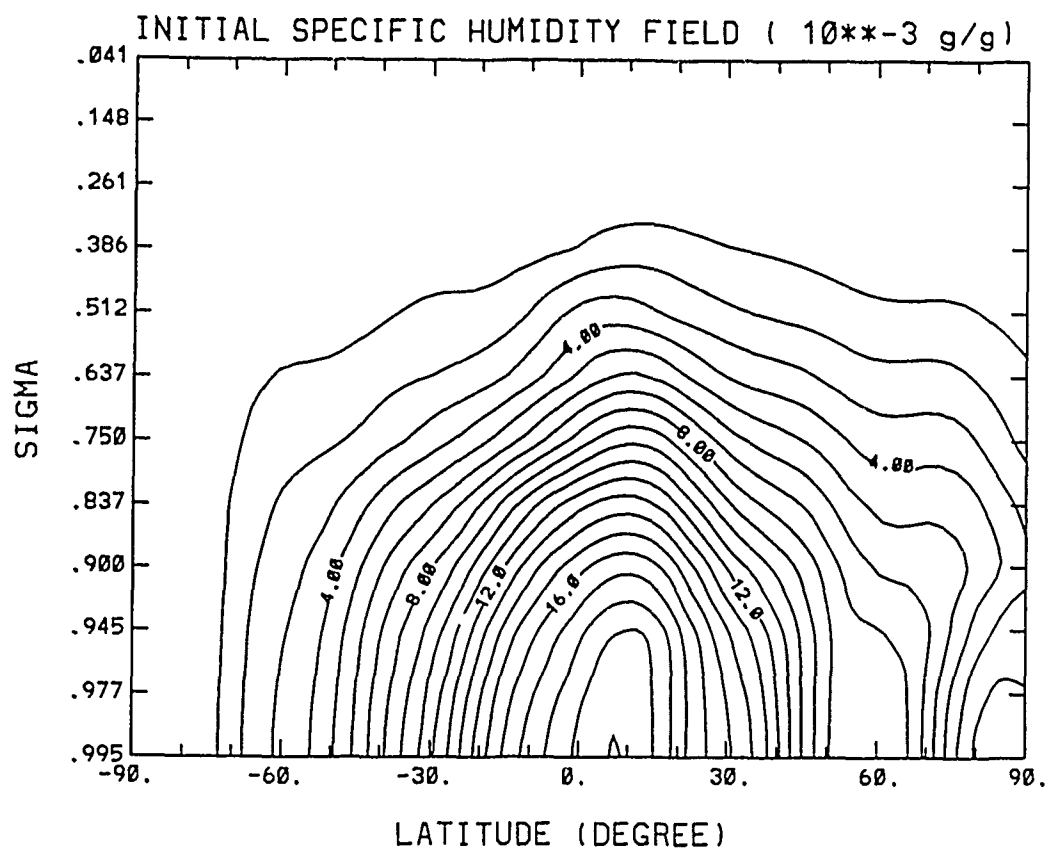


Figure 5.3. The zonal mean field of initial specific humidity.

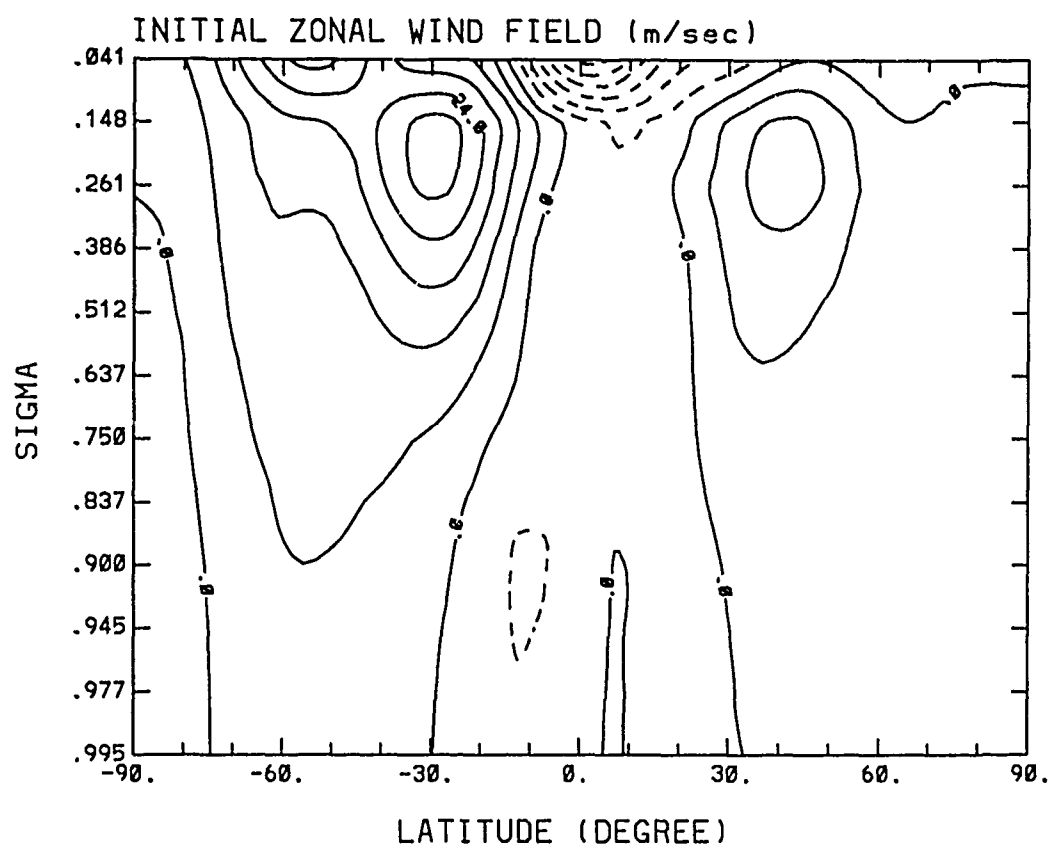


Figure 5.4. The zonal mean field of initial zonal wind.

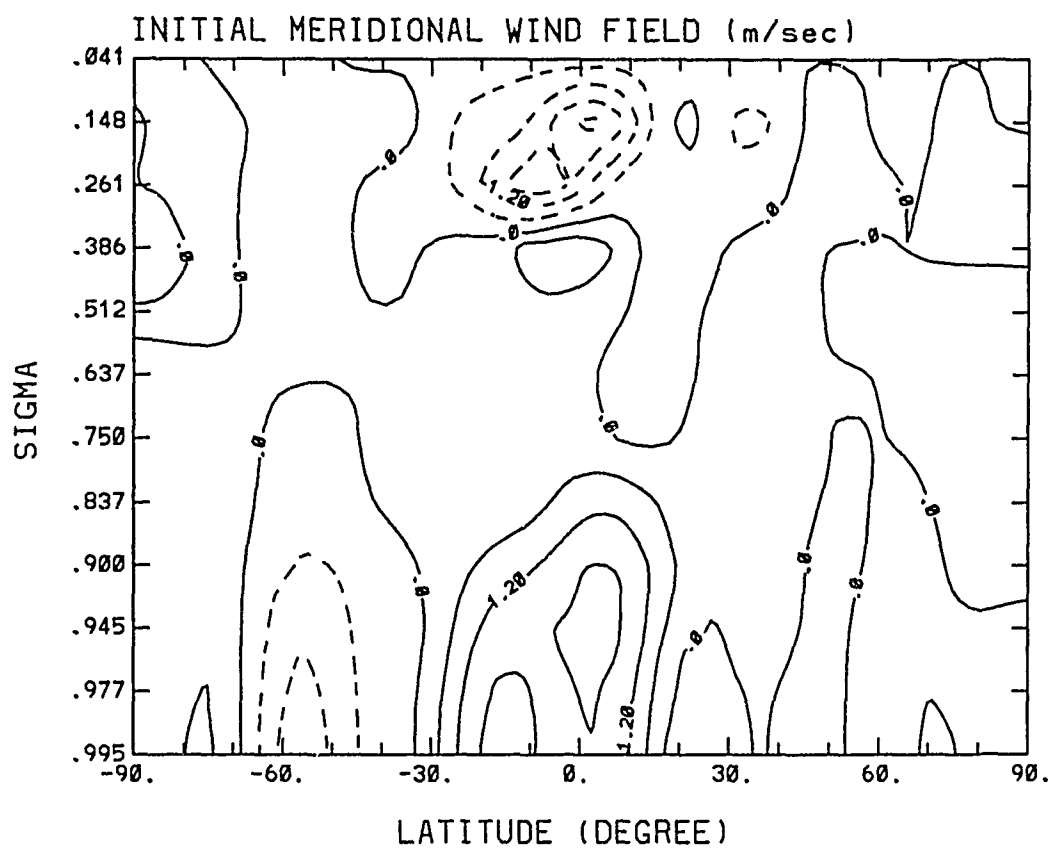


Figure 5.5. The zonal mean field of initial meridional wind.

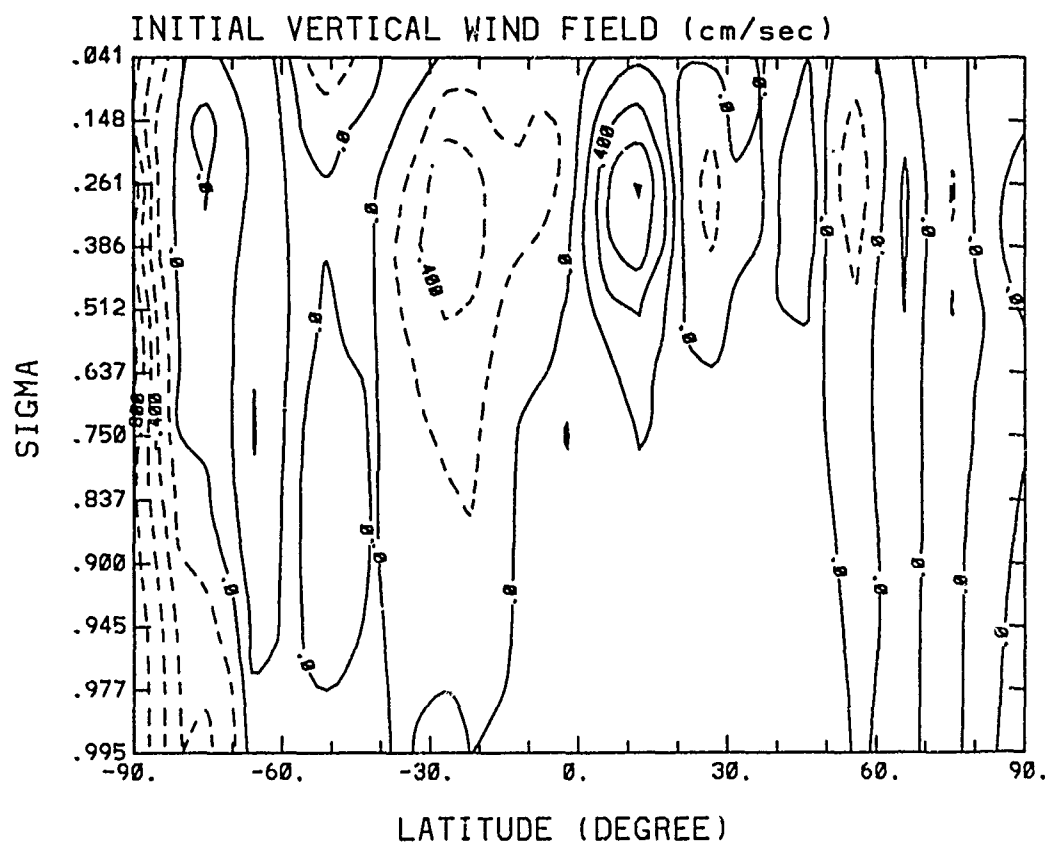


Figure 5.6. The zonal mean field of initial vertical velocity.

Since saturation vapor pressure is a function of temperature only, saturation specific humidity is determined by temperature and pressure. Initial relative humidity, the ratio of initial specific humidity to its saturation value, is determined. Therefore, the initial cloud cover is obtained through the definition in Equation (2.6) with the values of h_0 derived from the Smagorinsky's (1960) empirical expression shown in Fig. 2.1.

The zonal average of initial cloud cover is shown in Figure 5.7. It is noted that clouds may be formed in every model layer, except the lowest three and the top two layers. One of the distinctive features in the figure is the small cloudiness associated with the subtropic highs at 30° N and 20° S, where downward motions are dominant. Large cloudiness is found at the tropics, the middle latitudes in the both hemispheres, and the arctic regions. The large cloudiness is associated with upward motions in the intertropical convergence zone (ITCZ) and mid-latitude storm tracks. The fraction of high cloud is about 0.2; low and middle cloud covers are larger than high cloud cover. The cloudiness within the Antarctic Circle is less than that within the Arctic Circle.

5.3 Model Results and Verification

5.3.1 Zonal means

5.3.1.1 Zonal mean cloud cover

In Figure 5.8, the model-predicted zonal mean total cloudiness, averaged over July 3-4, is compared with the corresponding 3DNEPH cloud observations. Differences between the two curves are generally within 10% of the total cloud cover except in the tropics, arctic, and antarctic areas.

As was mentioned in the Section 4, 3DNEPH under- and over-estimates cloud covers in arctic and antarctic regions, respectively, for the summertime of the Northern Hemisphere. This observational bias is depicted in Figure 5.9 by the

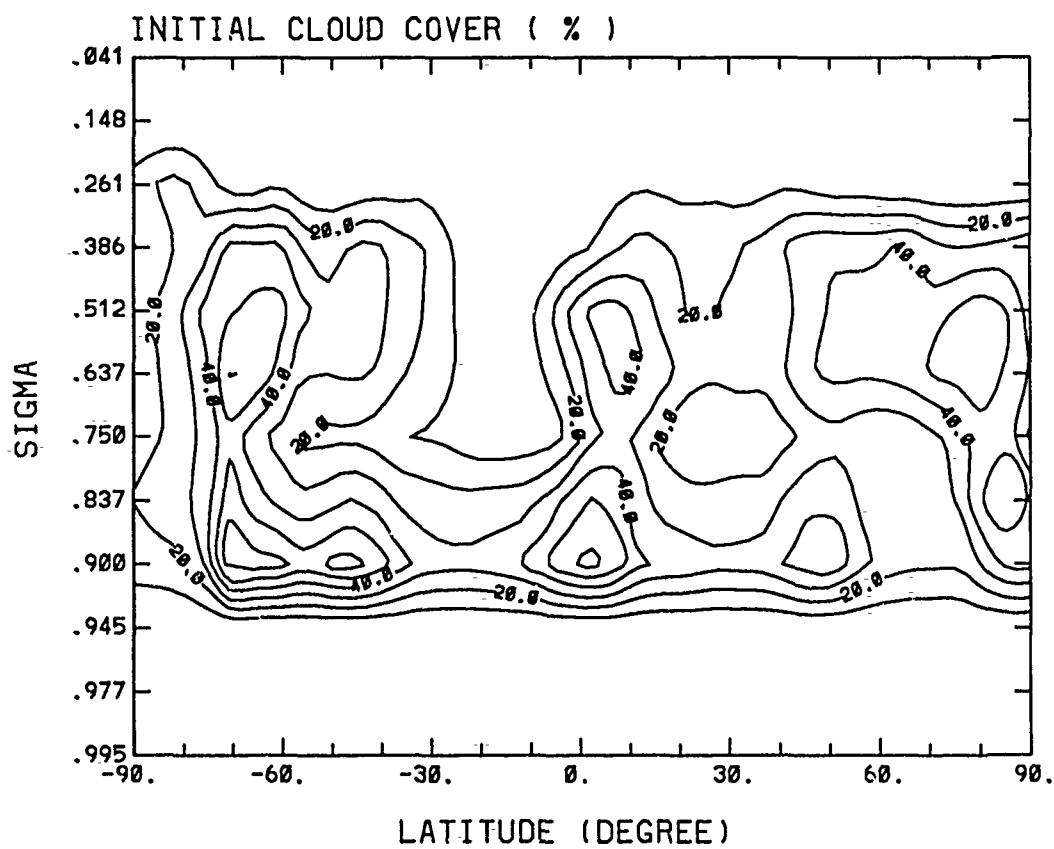


Figure 5.7. The zonal mean field of initial cloud cover.

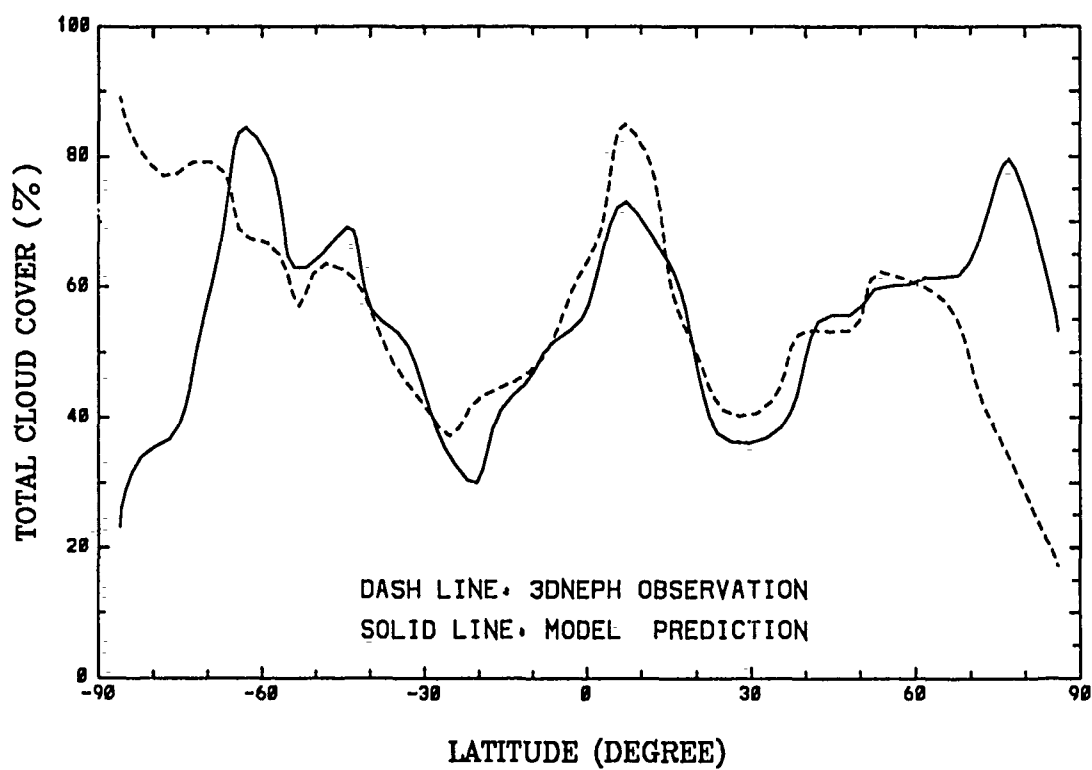


Figure 5.8. Comparisons of the zonal mean total cloudiness in the simulation and 3DNEPH.

comparison of 3DNEPH monthly mean data with London's cloud climatology based on surface cloud observations. Since London's cloud climatology was compiled only for the Northern Hemisphere, the comparison is confined to the Northern Hemisphere. As indicated in Figure 5.9, London's cloud climatology shows about 70% of total cloudiness in the summertime Arctic region and 40% in the wintertime. The 70% of total cloudiness in the Arctic is close to our model prediction in the area. This explains the differences between the predicted and 3DNEPH cloud cover in the arctic and antarctic regions.

The observed large cloudiness in the tropics is largely contributed by tropical anvils, which originate from convective clouds. Since the present large-scale cloud model is developed primarily for stratiform clouds, the simulated cloud cover in the tropics is underestimated, as is evident in Figure 5.8. Another shortcoming in the simulated cloud cover is the overestimation of cloud cover near the 60° S, where the incoming solar radiation is small. As a result, longwave radiation produces strong radiative cooling at the top of middle clouds and results in a large increase of total cloudiness in the region. It appears that improvement could be made if a dynamic instability feedback were allowed in the simulation. Nevertheless, the comparison of zonal mean cloud cover shows good agreement between the simulation and observation. The simulated small cloud cover located at the subtropic highs in both of the hemispheres are realistic. A large cloudiness in the tropics is also predicted, although the 3DNEPH data suggests that it is underestimated.

5.3.1.2 Zonal mean earth's radiation budget

Figures 5.10 and 5.11 are the same as Figure 5.8 except for OLR and net solar flux at TOA, respectively. Figure 5.10 indicates good agreement in OLR between the model simulation and ERB observation with differences being generally less than 10 W/m². Both curves indicate two maxima located in the subtropics in

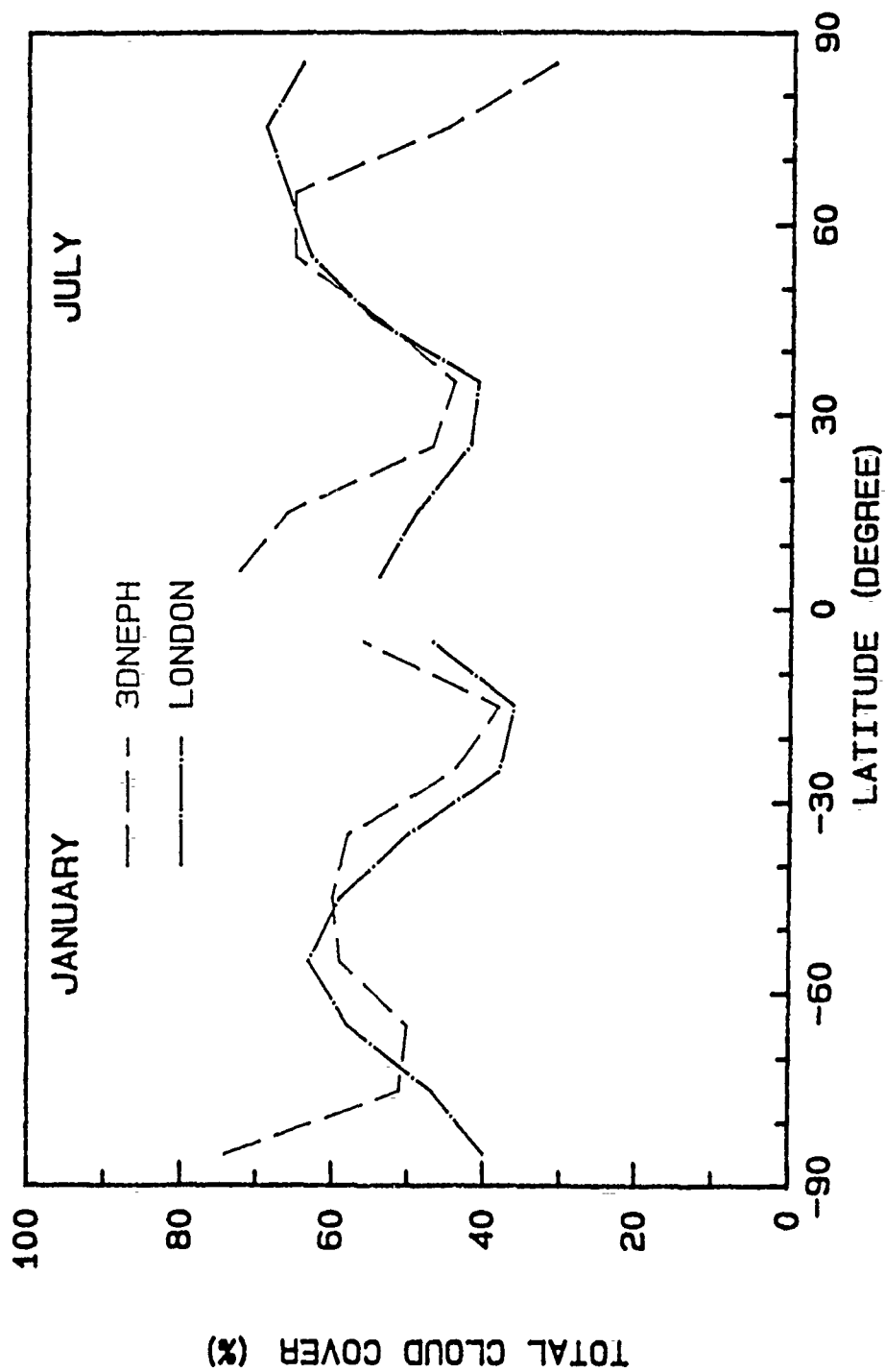


Figure 5.9. Comparisons of the 3DNEPH and London's cloud climatology.

both hemispheres with a minimum in the tropics. These two well-defined OLR maxima are associated with the subtropical highs, where small cloudiness and high temperature produce strong outgoing longwave flux. The OLR in the Southern Hemisphere is considerably smaller than in the Northern Hemisphere because of the low temperatures in the wintertime Southern Hemisphere.

The minimum OLR in the tropics is related to the ITCZ region, in which anvil cirrus originating from deep convective clouds occupy a large part of the sky at very high altitudes. These anvil clouds absorb the OLR emitted from the earth's surface and re-emit to space at much lower temperature than at the surface. As a consequence, the OLR in the ITCZ is greatly reduced. The minimum OLR in the tropics is reasonably well-predicted, although the simulated value is 30 W/m^2 higher than that in the ERB data. This overestimation of OLR may be explained by the following two reasons. First, the altitude of high clouds defined in the model is usually lower than the actual height of a tropical anvil cloud. Second, the simulated cloud covers in the tropics are underestimated.

Illustrated in Figure 5.11 is the zonal mean net solar downward flux at TOA for the model simulation and the ERB observations. The agreement between the two curves is promising with differences being generally within 20 W/m^2 . There are two points to note in this comparison. First, the maximum in the solar flux occurs at approximately 30° N for both cases. This peak of net solar flux is due to the combined effects of large insolation in the Northern Hemisphere and small cloudiness in the same regions. Second, a dip is found in each of the curves at 10° N , i.e., in the ITCZ, in which a maximum total cloudiness is located. It is also noted that solar flux is zero within the Antarctic Circle because the sun does not rise above the horizon at the region in July.

Comparing Figures 5.10 and 5.11, the model-simulated OLR and net solar flux at TOA are generally consistent. For instance, both the simulated OLR and net

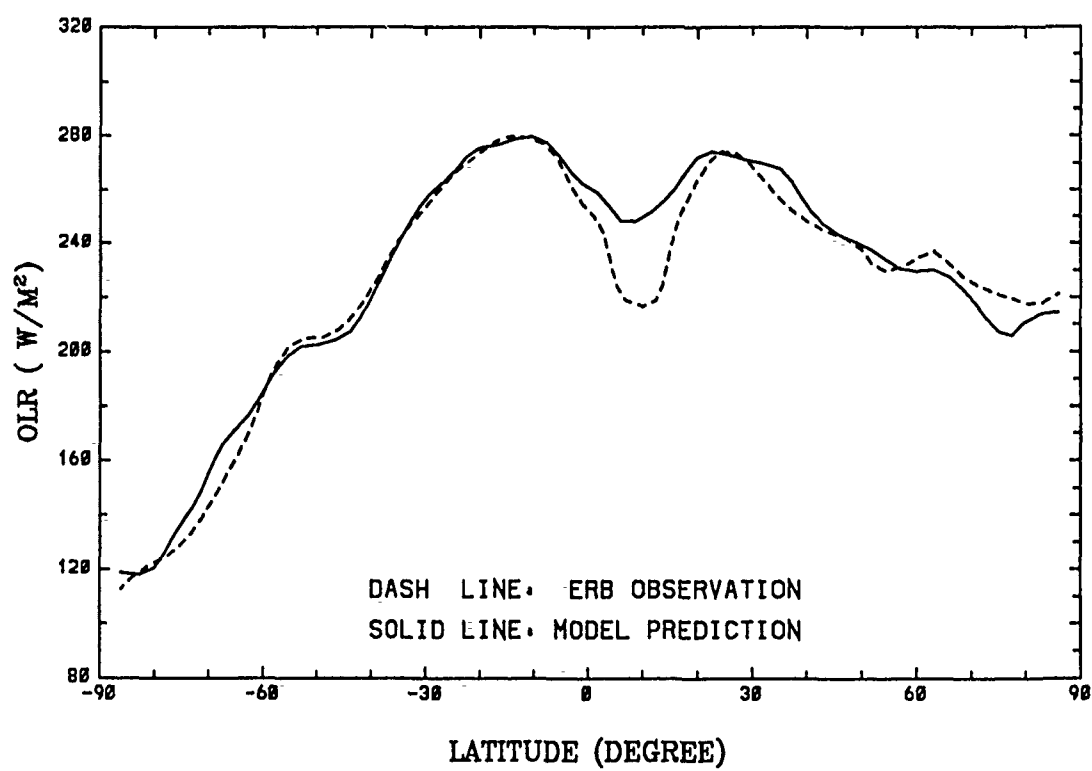


Figure 5.10. Comparisons of the zonal mean OLR in the simulation and from ERB data.

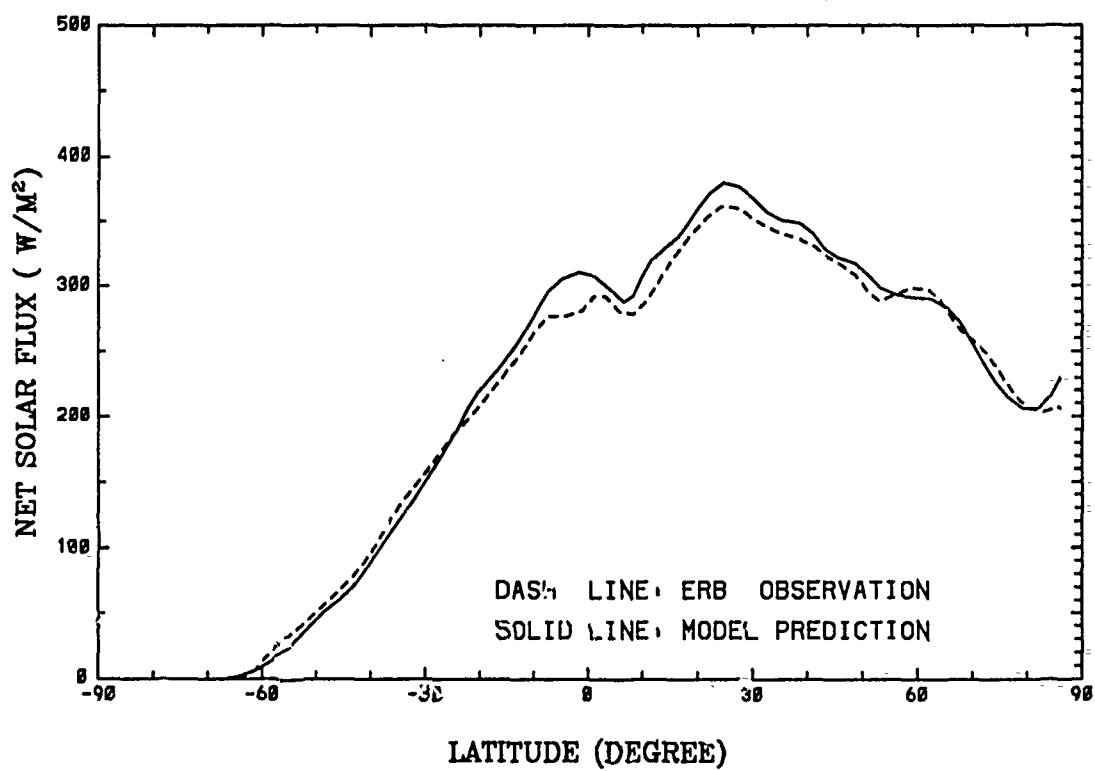


Figure 5.11. Comparisons of the zonal mean net solar flux at TOA in the simulation and from ERB data.

solar flux exceed those from the ERB observations in the tropics.

5.3.1.3 Zonal mean cloud LWP

Data on cloud LWP are very limited. There is no observational LWP data on a daily basis with which to compare, nor are the zonal averaged values of LWP available for July of 1979. Since the time domain in this study is the very beginning of July, we have compared the predicted zonal mean LWP with the monthly averaged zonal mean data from SMMR for June, 1979. Figure 5.12 shows the zonal mean LWP in the simulation and from SMMR measurements taken from Prabhakara and Short (1984). Only the LWPs zonally averaged over the oceans are shown in the figure for both simulation and observations. The zonal mean values of simulated cloud LWP compare quite well with SMMR observations. Differences between the two results are within 5 mg/cm^2 which is the accuracy of SMMR data suggested by Prabhakara and Short (1984).

The maximum LWP occurring in the tropics is related to the ITCZ. The two well-defined local maxima of LWP at the mid-latitudes in both hemispheres are associated with the mid-latitude storm tracks. Minimum of LWP are found in the regions of subtropical highs with prevailing downward motions. The SMMR data has maximum values of about 14, 4.7, and 4.0 mg/cm^2 in the tropics and mid-latitudes of Southern and Northern Hemispheres, respectively, while the corresponding values in the simulation are 13, 5.3, and 6.5 mg/cm^2 , respectively. The ratio of maximum LWP in the tropics to those in the middle latitudes is about 3 to 1. However, this ratio is only about 2 to 1 in the model simulation. This indicates that the ITCZ peak in LWP is less pronounced in the simulation than in observations. Obviously, the model underestimates the cloud LWP in the tropics, where a large portion of LWC observed by the SMMR is condensed in convective clouds which are not simulated in this model.

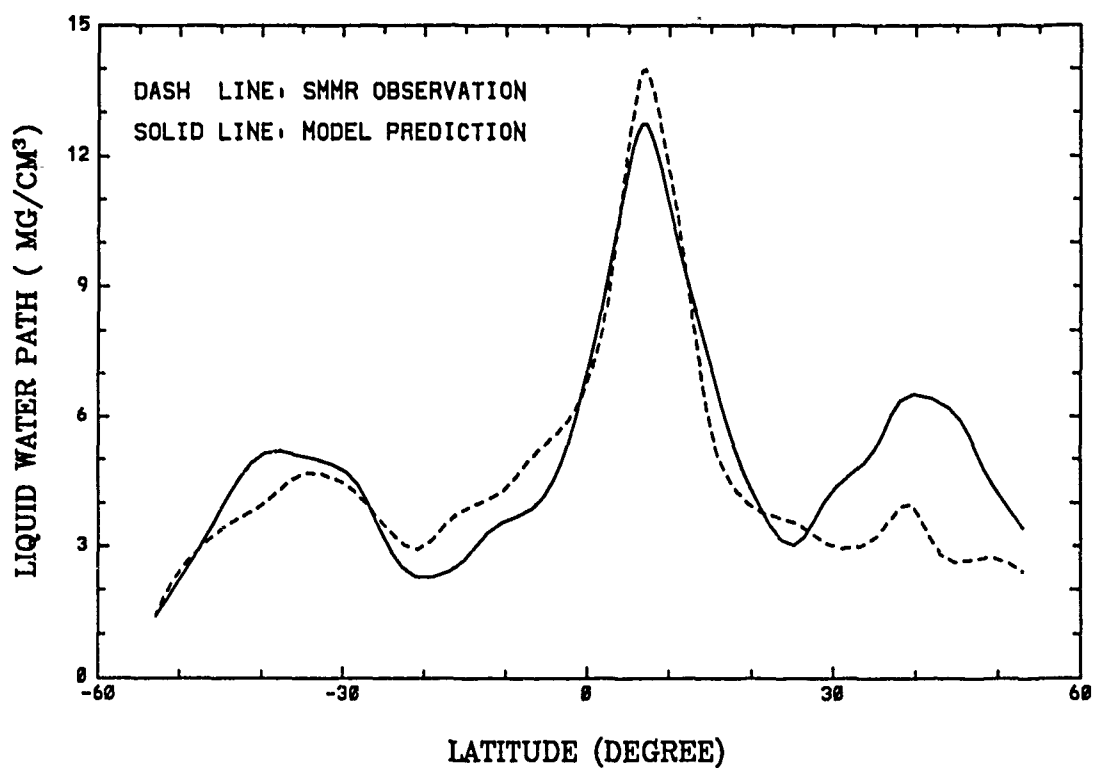


Figure 5.12. Comparisons of the zonal mean LWP in the simulation and from SMMR data.

5.3.2 Geographical distribution of cloud simulations

The predicted cloud cover, earth's radiation budget, LWP, and precipitation in the following figures are presented in horizontal cross-sections to demonstrate the geographical distribution of cloud fields. Cloud cover and earth's radiation budget are illustrated by the shades of gray with the intensity in the picture proportional to some ranges of data values.

5.3.2.1 Cloud cover

Figures 5.13 and 5.14 show, respectively, the geographical distribution of cloud cover in the observation and simulation, with the corresponding gray values given in the lower right-hand corner. The brighter the cloud picture, the larger the cloud cover is.

The major distinctive features of the geographical distribution of cloud cover depicted in the observation as well as simulation include:

1. A pronounced bright band of cloudiness extending along ITCZ from 150° W to 90° E, where the cloud band splits into two bands. The north cloud band spreads widely northeast into southern Asia and the northwestern Pacific; the south band expands southeast to the southwestern Pacific. The north band is associated with the seasonal monsoon and the south band is related to the Southern Pacific Convergence Zone (SPCZ). Although the ITCZ cloud band is less pronounced in the simulation, the model well predicts the bright cloud bands extending from the central Pacific to the central Atlantic, and in central Africa.
2. Areas of small cloudiness, i.e., a dark cloud picture, associated with subtropical highs occurring at both north and south of the ITCZ. For example, the small cloud covers over the southern Africa, Europe and Middle-East Asia,

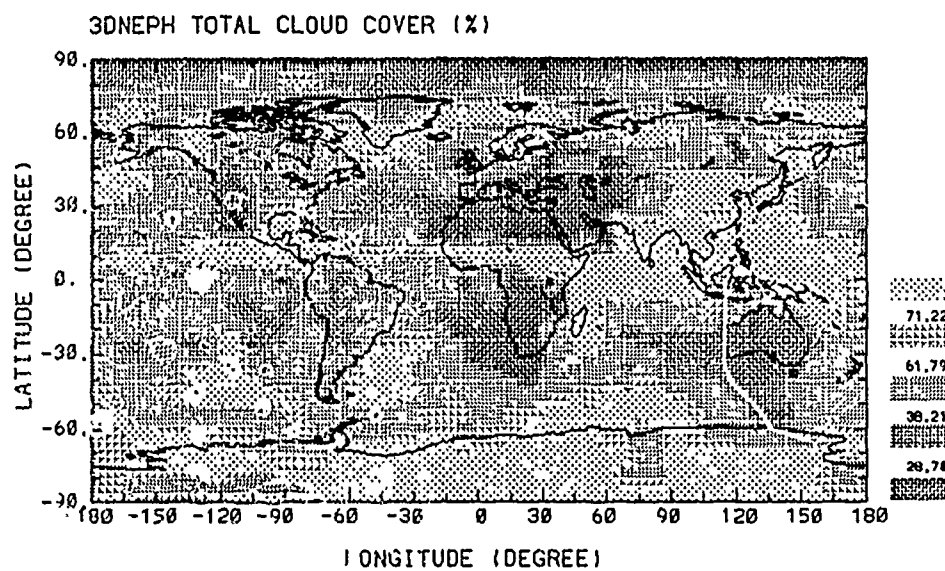


Figure 5.13. The geographical distribution of total cloud cover from 3DNEPH.

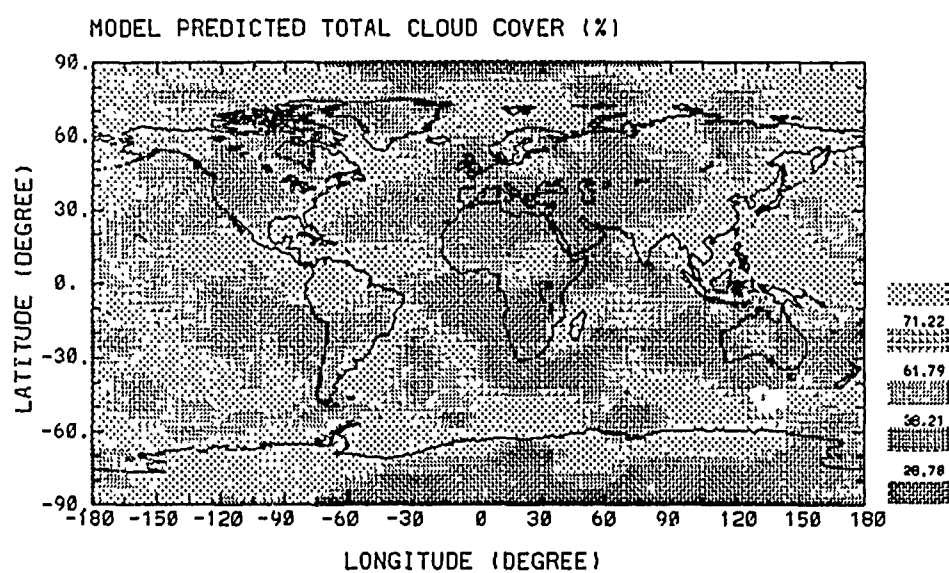


Figure 5.14. The geographical distribution of total cloud cover in the simulation.

and North and South America are clearly identified in both observation and simulation. The oceanic subtropical highs in the Atlantic and Pacific Oceans are also evident by the small cloudiness over the regions.

3. The large bright cloud bands in the mid-latitudes of both hemispheres associated with the mid-latitude storm tracks. In both the simulation and observation, bright cloud bands are found over the east coast of South America, southern and northern Pacific, and the Greenland Sea. The cloudiness over the east coast of North America is larger in the simulation than in the observation.
4. The under- and over-estimation of cloud cover by 3DNEPH in the arctic and antarctic regions, respectively, for the summer season of the Northern Hemisphere. Comparing Figures 5.13 and 5.14, it is obvious that the cloud picture over the antarctic area is brighter in the observation than in the simulation, and vice versa for the arctic region.

5.3.2.2 Earth's radiation budget

The earth's radiative flux at TOA reflects many of the features in the simulated cloudiness discussed in the previous section. It is the radiative effects of clouds rather than the cloud cover alone that ultimately determines the model's simulation of the radiation budget. Therefore, comparisons of the simulated earth's radiation budget with ERB data may provide valuable guidance on the cloud radiative properties of the LWC/IWC simulated in the model.

Figures 5.15 and 5.16 show the outgoing longwave radiation in the observation and simulation, respectively. Figures 5.17 and 5.18 are the same as Figures 5.15 and 5.16, respectively, except for net solar downward flux at TOA. The intensity of the gray shades, given in the lower right-hand corner of each figure, is defined such that the brighter the picture, the smaller the radiative flux.

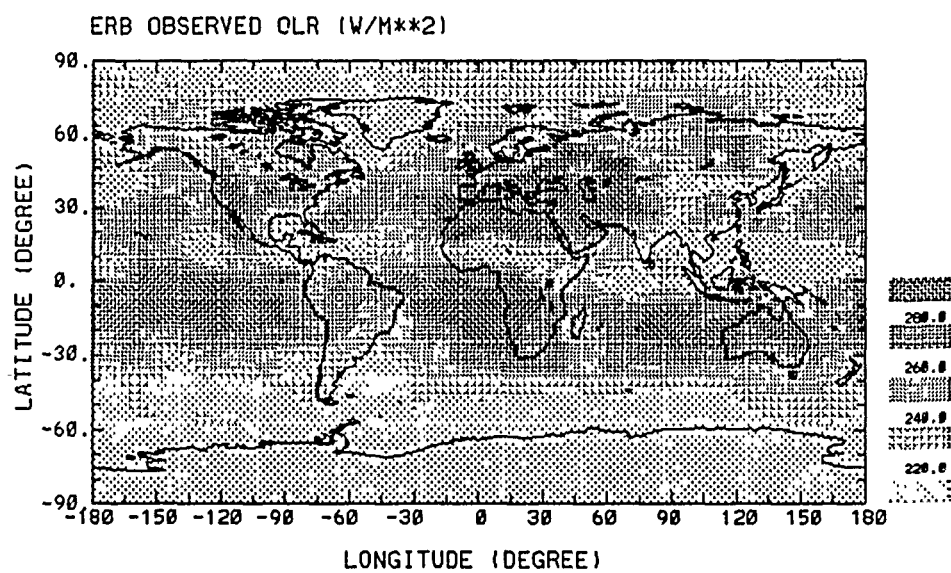


Figure 5.15. The geographical distribution of OLR from ERB data.

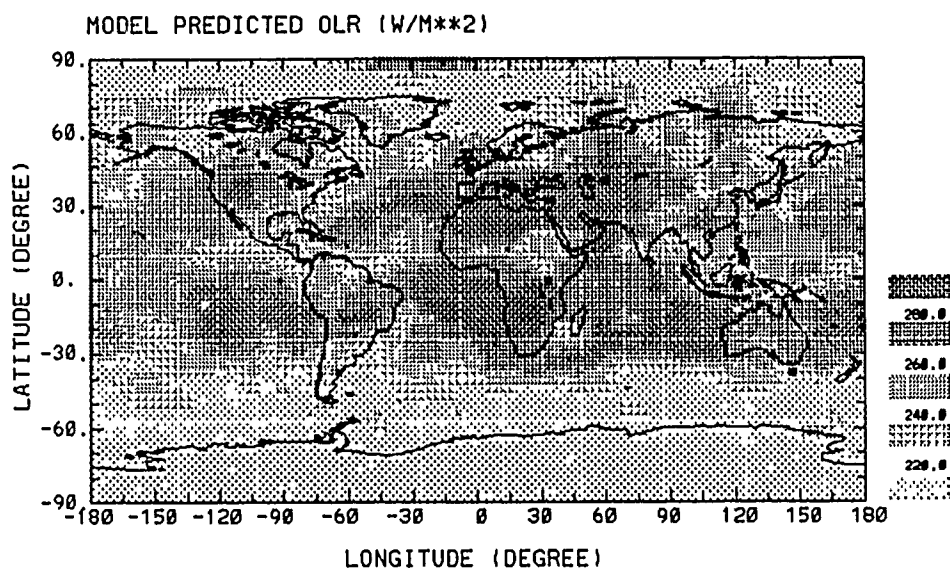


Figure 5.16. The geographical distribution of OLR in the model simulation.

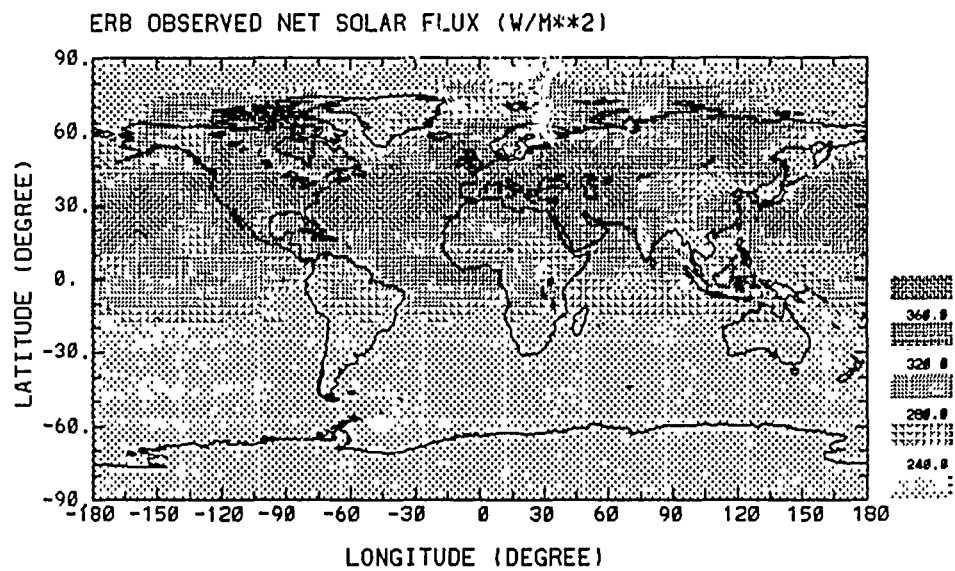


Figure 5.17. The geographical distribution of net solar flux at TOA from ERB data.

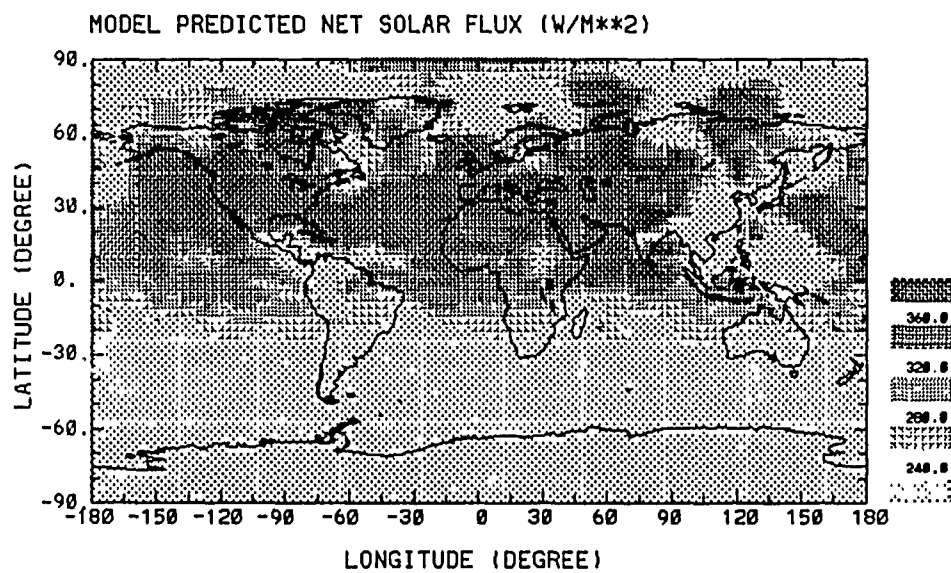


Figure 5.18. The geographical distribution of simulated net solar flux at TOA.

In all four figures, small flux values from the 90° S to about 40° S are due to relatively low solar radiation in the winter hemisphere. Therefore, very few flux features over these regions are evident in Figures 5.15 - 5.18. However, north of the 40° S, more flux features are evident in all of the figures because of relatively large solar zenith angle and more variability in cloud cover.

The earth's radiation budget in the simulation shows good agreement with that in the observation. There are two distinctive features on these maps. First, the well-defined ITCZ and monsoon circulation are characterized by a bright picture, i.e., small values of OLR and net solar flux. They are located over the equatorial western and eastern Pacific, the Atlantic, and central Africa, as well as the monsoon area over the India and Asia. As mentioned previously, the cloudiness in these regions is underestimated in the simulation. As would be expected, the flux values in these regions are overestimated by the model. Second, the almost continuous belts of dark picture are associated with the subtropical highs located to the south and north of the ITCZ. In these regions, large flux values for both OLR and net solar flux are due to the small cloudiness dominating the areas. Small flux values are also evident in the areas of the mid-latitude storm tracks in the Northern Hemisphere. However, the simulated values of OLR and net solar flux in the Greenland Sea, near 70° N and 0° E, appear to be too small compared with the observation.

5.3.2.3 Liquid water path

Figures 5.19 and 5.20 illustrate the geographical distribution of LWP in the observation and simulation, respectively. The observation, taken from Prabhakara and Short(1984), is a monthly averaged map for July, 1979. As was mentioned previously, the SMMR observations were limited to the oceans equatorward of 60° latitude because of a nearly constant emissivity over the ice-free sea surface. As

would be expected, Figure 5.19 shows no SMMR results on LWP over land and at high latitudes.

In both of the Figures, large amounts of liquid water placed in the ITCZ and Asian monsoon regions are clearly evident, while in the subtropical highs at both of hemispheres small amounts of liquid water are found. In the central and southern Pacific, the model simulates large values of LWP, which are also evident in the observation. In both the simulation and observation, an abundance of liquid water is found over the Indian Ocean, and southeast and northeast Asia. In addition, the well-defined observed local maxima of LWP near the east coasts of North, Central, and South America are clearly simulated by the model. Localized LWP minima observed west of Africa, and South and North America are also shown in the simulation. These minima are associated with large-scale atmospheric subsidences; a mechanism which acts to prevent water vapor from condensing, greatly reducing cloud LWC in these regions.

The large amounts of liquid water associated with the mid-latitude storm tracks near 50° S(N) - 60° S(N) are not shown in the SMMR observation because of high latitudes where sea surfaces are covered with ice. In addition, the model simulates large amounts of liquid water over land at Central America, central Africa, India and southeast China. These results are not reported by the SMMR observations due to the inhomogeneous emissivity over the land surface. From the above comparisons, it appears that the geographic distribution of LWP is well simulated.

5.3.2.4 Precipitation

Precipitation is initiated by cloud microphysical processes such as collision and coalescence, through which small cloud droplets merge into large raindrops. However, the model's large-scale precipitation distribution, when averaged over extended periods, is determined by the circulation in the model, rather than by

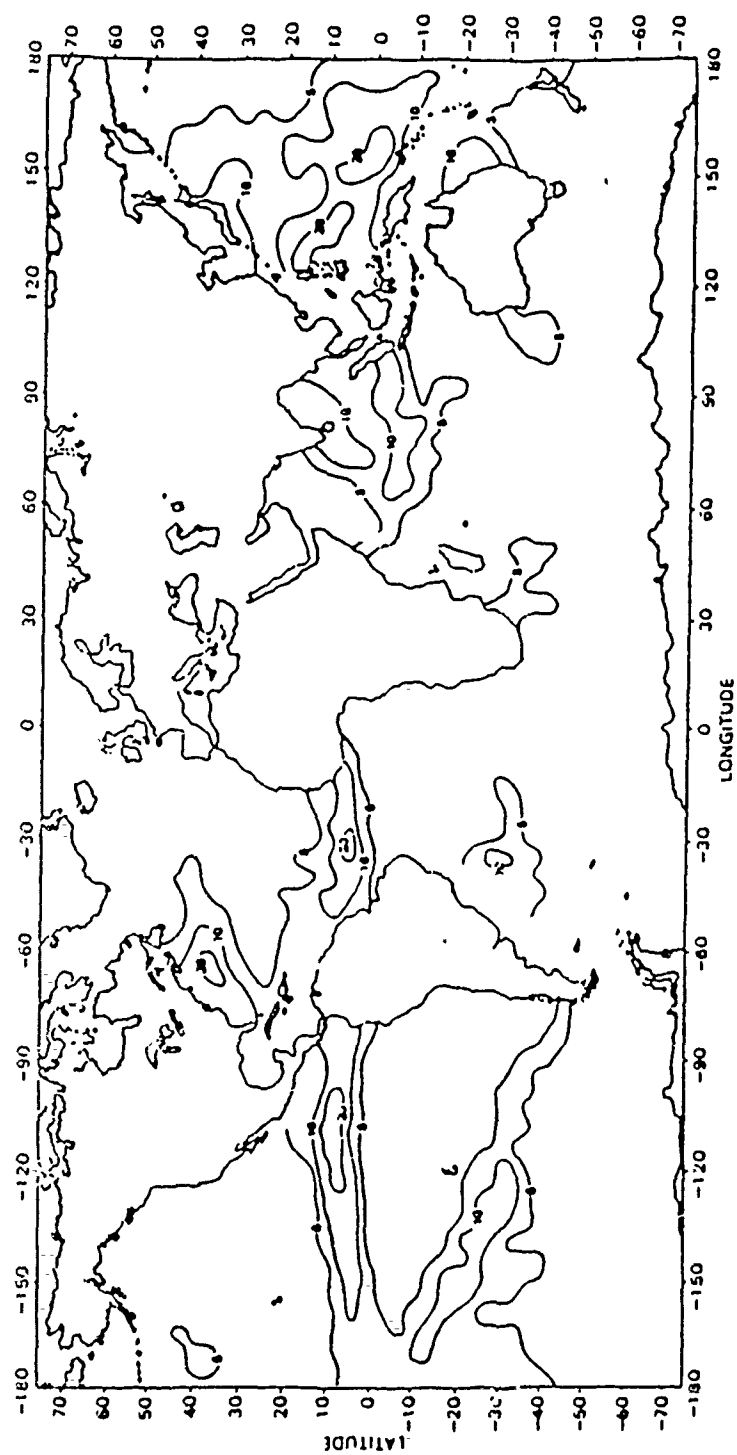


Figure 5.19. The geographical distribution of LWP from SMMR data.

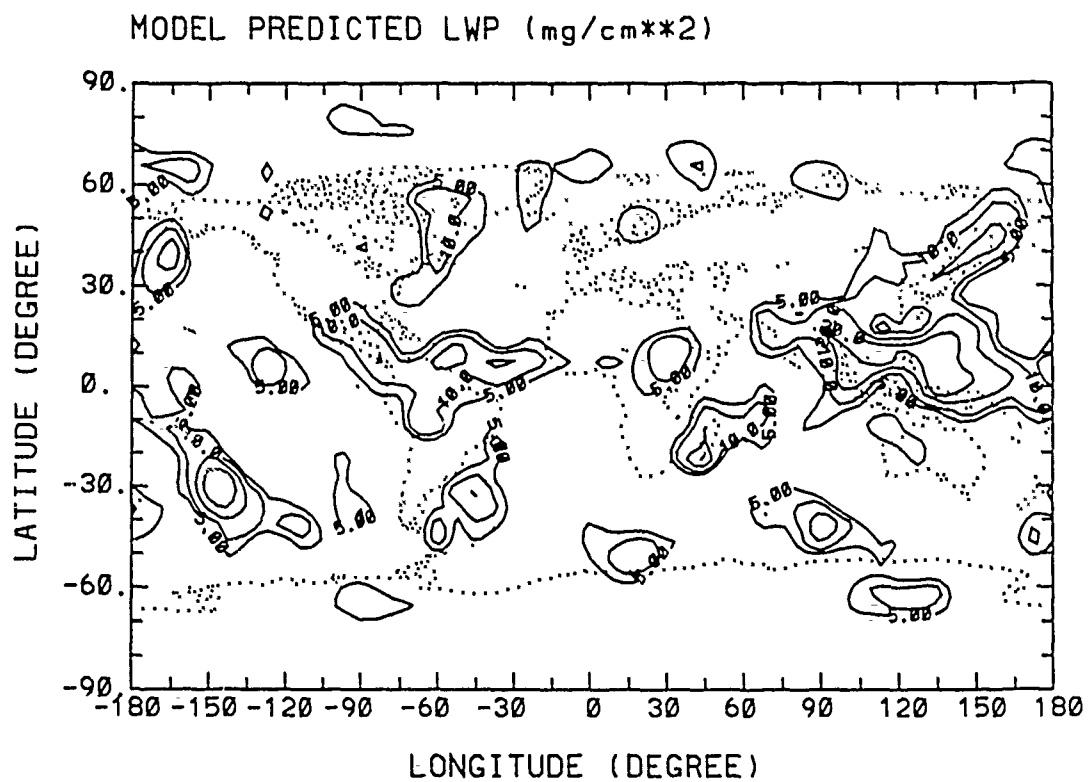


Figure 5.20. The geographical distribution of LWP in the simulation.

the cloud microphysical processes themselves (Smith's, 1990). Moreover, observed precipitation is largely generated by convective clouds, which are not included in the model simulation. Due to the simplicity of the prescribed wind fields and the exclusion of convective clouds in this study, it is not our intent to verify quantitatively the simulated precipitation at this stage. Instead, the geographical distribution of simulated precipitation is shown in this section.

Figure 5.21 shows the geographical distribution of simulated precipitation. In the figure, a noticeable rain belt is located along the ITCZ. The model well simulates the precipitation maxima of both the Atlantic and the Pacific branches of the ITCZ, as well as that in the South Pacific Convergence Zone. The precipitation minima are simulated in the regions of subtropical highs, located south and north of the ITCZ. Little precipitation is simulated over the deserts, such as the Sahara and the Gobi. The wide-spread rain bands associated with the mid-latitude storm tracks are shown in the simulation. Large amounts of simulated precipitation is shown on the east coast of America, in contrast to small amounts of precipitation on the west coast. A noticeable amount of precipitation is simulated over central Africa, while little precipitate can be found over west Africa.

5.3.3 Cloud ice content

Since observational data on cloud IWC is not available on the global basis, we qualitatively compare the model-predicted cloud IWC with aircraft measurements in cirrus, as well as with other model results. Based on the aircraft measurements in mid-latitude cirrus over the United States, Heymsfield and Platt (1984) derived the dependence of cirrus cloud properties, including cloud IWC, on the temperature. According to their report, averaged cloud IWC varied from a few milligrams per cubic meter at temperatures below -40°C to about 20 mg/m^3 above -40°C .

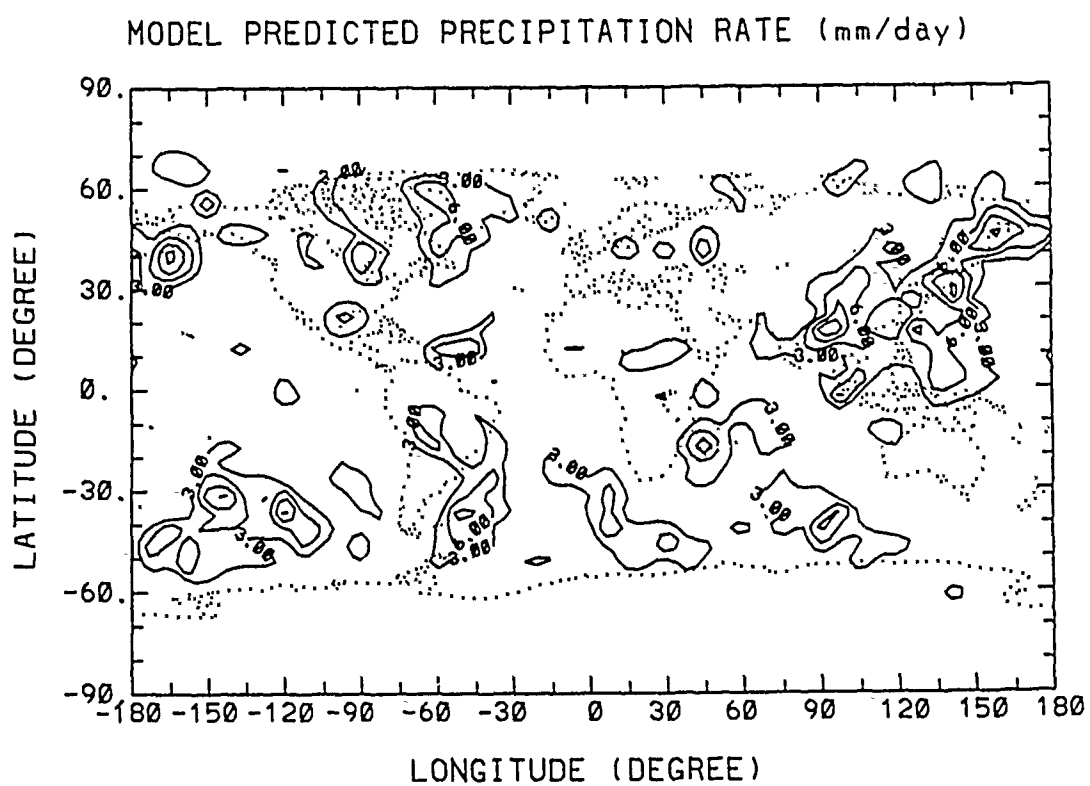


Figure 5.21. The geographical distribution of precipitation in the simulation.

Similar magnitudes of cloud IWC were also simulated in the cirrus cloud model by Starr and Cox (1985).

The zonal average of simulated cloud IWC, averaged over July 3-4, 1979, is shown in Figure 5.22. The magnitude of predicted cloud IWC is on the order of 10 mg/m^3 , which is consistent with the aforementioned model simulation and aircraft observational values in cirrus.

Comparisons between Figures 5.22 and 4.1 indicate the maxima of cloud IWC locate along -15°C , in which the maximum Bergeron-Findeison's processes occur. The simulated cloud IWC decreases from about 10 mg/m^3 near -15°C to a few milligrams per cubic meter at temperatures below -40°C . The variations of cloud IWC with respect to the temperature are similar to those suggested by Heymsfield and Platt (1984). It is noted that the simulated cloud ice disappears at temperatures warmer than the freezing point, since the melting process converts ice crystals into cloud liquid water. Ice crystals and liquid water may co-exist at the region above the freezing level.

The latitudinal distribution of cloud IWC appears realistic. In the antarctic area, Southern Hemisphere wintertime, all low, middle, and high clouds are ice clouds, while in the arctic region, Northern Hemisphere summertime, only the middle and high clouds are ice clouds. In the tropics, only high clouds are dominated by ice crystals.

Based on the above discussions, the simulated cloud IWC appears to depend more on temperature than on vertical velocity, which is important to the condensational process. The predicted cloud IWC appears to agree very well with that of the aircraft observations in cirrus clouds.

5.4 Discussion

The comparisons shown in the previous sections indicate the developed large-scale cloud model is able to simulate rather realistically zonal means and geo-

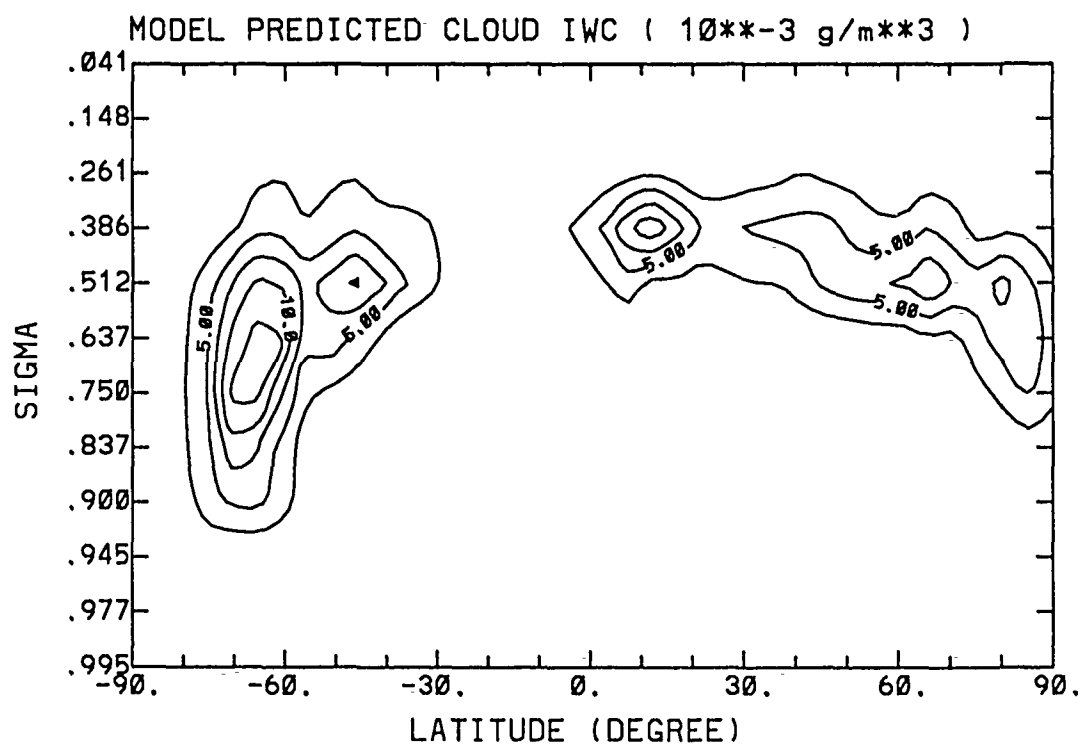


Figure 5.22. The zonal mean field of cloud IWC in the simulation.

graphical distributions of cloud fields, including cloud cover, cloud LWC/IWC and precipitation. By interactively providing the cloud cover, cloud LWC and IWC to the radiative transfer calculations, the earth's radiation budget, namely OLR and net solar flux at TOA, is also well simulated. More importantly, the previous comparisons demonstrate the consistency between the simulated OLR and net solar flux at the TOA. For instances, both of them are small over the regions of ITCZ and monsoon, and large at the subtropical highs.

While the comparisons between the simulations and observations attempt to verify the model prediction, intercomparisons among the simulated fields, including cloud cover (Fig. 5.14), OLR (Fig. 5.16), net solar flux (Fig. 5.18), LWP (Fig. 5.20) and precipitation (Fig. 5.21) may render us some physical insight into the relationship between the large-scale circulations and cloud formation.

The model simulation shows that clouds are strongly tied to the large-scale circulations. For instances, the influence of the Asian monsoon circulation and ITCZ on cloud formation are prominent. These regions are associated with convergences of low-level winds (i.e., upward motions), and deep moist tropospheres. The low-level wind convergences result in upward motions and cooling expansions of the air parcels. At the same time, the deep moist tropospheres provide the water vapor that allows condensation to occur in the air parcels. Consequently, large amounts of cloud form in these regions, as evident in Figures 5.14, 5.20 and 5.21. Observing the model-simulated results in these figures for the ITCZ and monsoon areas, we find model consistently simulates large amounts of cloud cover, LWP, and precipitation in these regions. Large amounts of cloud cover coincide with large amounts of cloud LWC, which generate large precipitation rates by virtue of autoconversion. Similarly, large amounts of cloud are simulated in the regions of the mid-latitude storm tracks, which are characterized by strong baroclinic instability in the atmosphere. These baroclinic disturbances are accompanied by

cloudiness maxima, abundance of liquid water, and noticeable rain bands in the middle latitudes of both hemisphere.

At the subtropical highs of both hemispheres, small amounts of cloud cover, LWP and precipitation in the simulation are associated with large-scale atmospheric subsidence, which is related to the branches of downward motion in the Hadley circulations. The downward motion tend to increase the atmospheric temperature and result in the decrease of relative humidity, which acts to prevent water vapor from condensing. As a result, small cloudiness, LWP minima, and little precipitation are simulated in these regions. It is also evident from the simulation that the east coast of America is favorable for cloud formation, while the west coast is not. Large amounts of cloud cover, liquid water, and precipitation are simulated on the east coast of America, but little cloud forms in the west coast.

One of the main problems in the verification of cloud simulation against satellite data is associated with the comparisons of vertically integrated liquid water (LWP). The LWP is given by the cloud LWC and model thickness as follow

$$LWP = LWC \times \Delta z$$

where LWC is the cloud LWC denoted earlier and Δz is the model vertical grid thickness. In the context of GCMs, clouds are sub-grid scale in the horizontal, and more seriously, in the vertical. However, in all of the GCM simulations, clouds are assumed to fill the entire vertical grid layer whenever clouds form. Consequently, the LWPs in the simulation are overestimated due to the exaggeration of cloud vertical extent in the model.

For example, low cloud base and middle cloud top in the model are defined at 925 mb and 450 mb, respectively. Thus the thickness of the low and middle clouds, in which most cloud LWCs are located, may be roughly estimated as 5 km. The magnitude of cloud LWC, based on the aircraft observations in stratus clouds

(Kriebel, 1989), may be estimated as 0.1 g/m^3 , i.e., 10^{-4} mg/cm^3 , which is on the order of the stratiform cloud LWC adopted in Liou and Wittman (1977). The LWP, given by the product of 10^{-4} mg/cm^3 and $5 \times 10^5 \text{ cm}$, is as large as 50 mg/cm^2 , which is about ten times larger than that derived from the SMMR observations in middle latitudes. Thus, in order to obtain reasonable LWP with the coarse model thickness, the cloud LWC has to be smaller than it is actually observed to be in the aircraft observations.

With the unavoidable overestimation of cloud thickness, the decision needs to be made whether the model attempts to simulate reasonable values in LWP or in cloud LWC. The motive of forecasting cloud LWC is to calculate interactively cloud radiative properties. Furthermore, since it is the effects of vertically-integrated cloud liquid water content (i.e., LWP), rather than cloud LWC alone that ultimately determines the cloud radiative properties, we have decided that the reasonable amount of LWP is more important than that of cloud LWC. In addition, there is no observational cloud LWC that can be utilized as verification data on the global basis. The model-simulated cloud LWCs are verified against SMMR observations in terms of LWP.

Having recognized the importance of LWP, we have adopted a large value for the autoconversion rate to reduce the amount of cloud LWC in the model, so that the model-simulated LWP may be comparable with the SMMR observations. Unless specified, the autoconversion rate is adopted as $C_0 = 5 \times 10^{-4} \text{ s}^{-1}$, which is 5 times larger than that used in Sundqvist (1978).

Section 6

SENSITIVITY STUDIES

In order to examine the interactions and feedbacks of radiative heating fields and ice phase cloud microphysics on the large-scale cloud simulations, a set of numerical experiments has been carried out with and without the inclusion of radiation and ice phase processes. A brief description of the experimental runs follows:

- CTRL: Control run which includes both radiation and ice-phase processes.
- EXP1: As in CTRL but without the radiation.
- EXP2: As in EXP1 but without the ice-phase processes.

All of these control and experimental runs have the same initial conditions, and wind fields, and their results are averaged over the same periods, allowing inter-comparisons to be made between the control run and the experimental runs.

6.1 Control Run

The control run is the same run as that described in the previous section. Its results were shown in the last section on the horizontal cross sections. In this section, these results are demonstrated in meridional cross section to show the vertical structure of cloud fields.

Figures 6.1 - 6.4 show the zonal average in temperature, cloud cover, cloud LWC and cloud IWC predicted and averaged over July 3-4, 1979, in the control run. The profiles of predicted cloud cover, shown in Figure 6.2, are related to those of vertical velocity depicted in Figure 4.5.

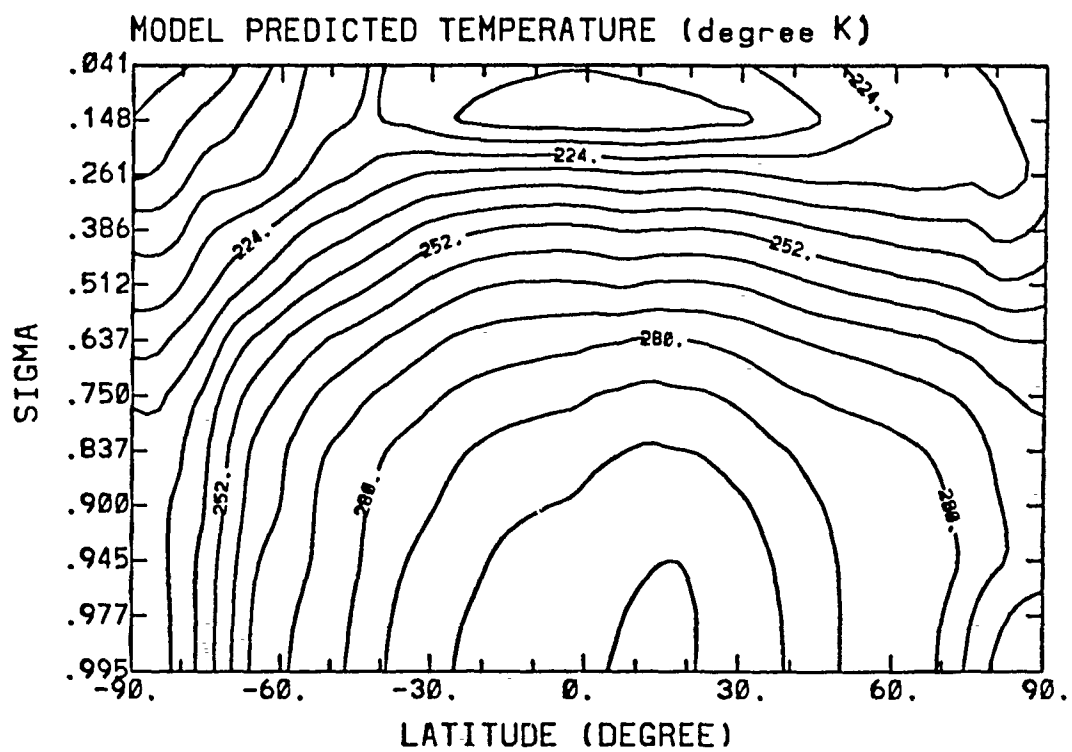


Figure 6.1. The zonal mean field of temperature in the control run.

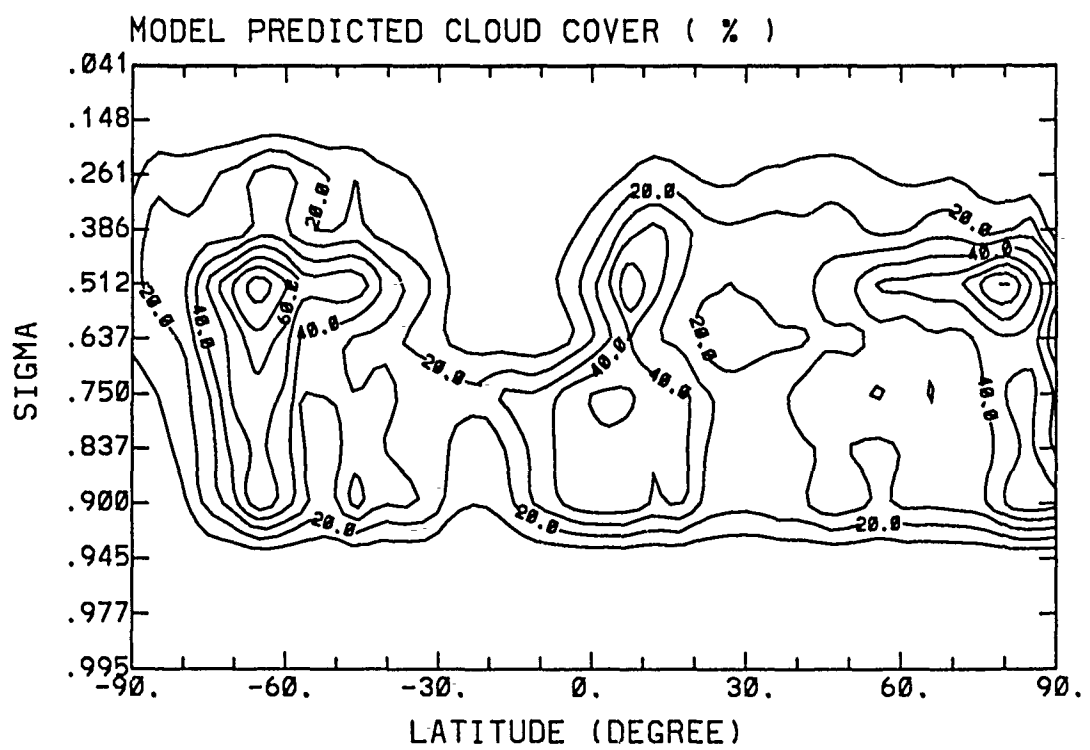


Figure 6.2. The zonal mean field of cloud cover in the control run.

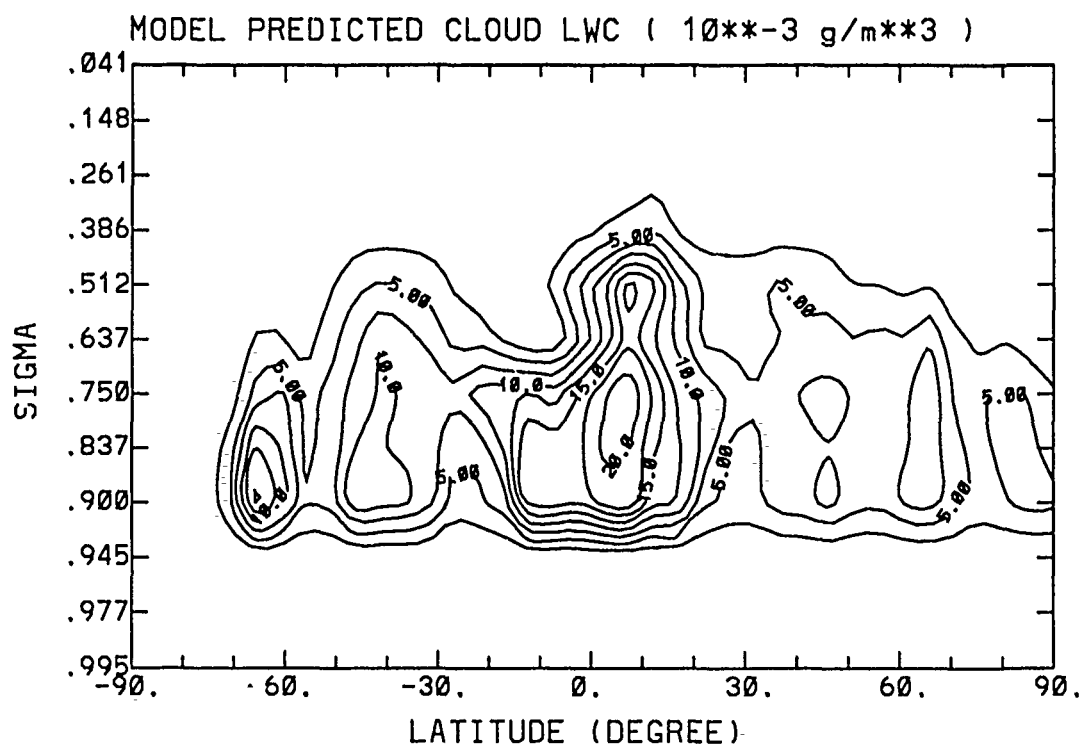


Figure 6.3. The zonal mean field of cloud LWC in the control run.

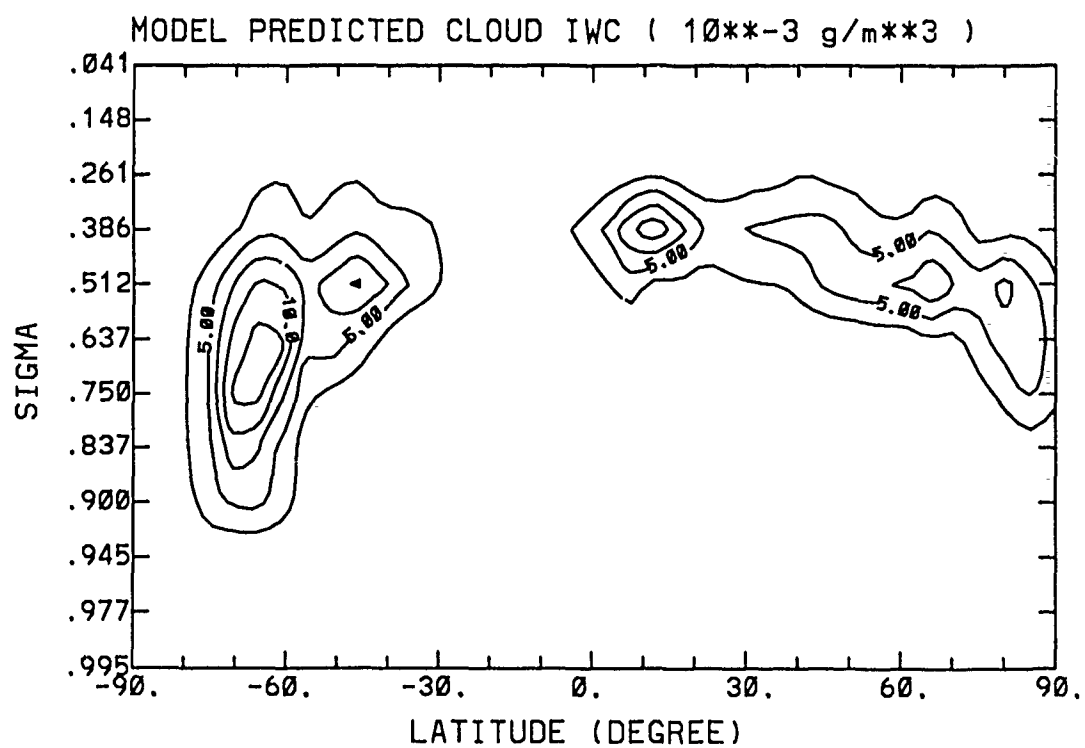


Figure 6.4. The zonal mean field of cloud IWC in the control run.

Three large amounts of cloud cover, located in the tropics and at the mid-high latitudes at both of hemispheres, are due to the large upward motions in these regions, while two relatively clear-sky areas at the subtropical highs in both hemispheres are related to the downward motions in the regions. In addition, cloud cover in the southern hemispheric subtropics is smaller than that in the Northern Hemisphere because of the branch of strong sinking motion of the Southern Hemisphere Hadley cell.

The pattern of simulated cloud LWC in Figure 6.3 is consistent with that of cloud cover in Figure 6.2; i.e., cloud LWC exists wherever there is cloud. The production of cloud LWC in the simulation depends on the vertical velocity and amount of moisture in the region. If the moisture supply is the same, the stronger the upward motion, the more cloud LWC is generated due to a large condensational rate resulting from a large vertical velocity. In the vertical, large amounts of cloud LWC are found in low and middle clouds because of abundant moisture available to condensation in low and middle atmosphere. Similarly, the maximum cloud LWC is located at the tropics and, two local maxima exist at the middle latitudes in both hemispheres.

The three large amounts of cloud LWC, located at the tropics and mid-latitude storm tracks in both hemispheres, correspond to the large cloudiness in these regions. The small amounts of cloud LWC associated with the subtropical highs are due to the prevailing downward motions in the regions. In the antarctic area, clouds contain small amounts of LWC because of the low temperatures in the area.

The zonal mean of cloud IWC, simulated in the control run, is shown in Figure 6.4, which is identical to Figure 5.22. Comparing of Figures 6.4 and 6.3, in the regions of high latitude or high altitude, where temperatures are low, clouds are dominated by the ice crystals, while in the tropics and low latitudes, where temperatures are higher, cloud LWC prevails in the clouds.

6.2 Experiment On Inclusion Of Radiation

Figures 6.5 - 6.12 show the results from the experiment with and without the inclusion of radiation. These figures indicate the differences obtained by subtracting the results in EXP1, i.e., without radiation, from those in CTRL, i.e., with radiation.

The differences in the solar radiative heating rates are illustrated in Figure 6.5, which show all the positive values. The results indicate that solar radiation basically heats the atmosphere. As would be expected, the solar heating rates in July in the Northern Hemisphere are much larger than in the Southern Hemisphere. Furthermore, there is no solar radiation within the Antarctic Circle because the sun does not rise above the horizon in the region in July.

There are three heating rate maxima with values of about 2°K/day located at the tops of middle cloud in the Northern Hemisphere. The large values of solar heating rates within the Arctic Circle are due to a longer solar day in the region in July, while large solar heating rates in the tropics are due to large solar zenith angles during the daytime. The large solar heating located in the upper atmosphere is associated with the strong O_3 absorption at high altitudes.

Figure 6.6 is the same as Figure 6.5, except for the IR radiative cooling rates. The most distinctive feature in the figure is the strong IR cooling rates occurring at the middle cloud tops. This is because high cloud is considered nonblack in the radiation calculations, while middle cloud is assumed to be a blackbody. As a result, the upward IR flux emitted by middle cloud is much stronger than the downward flux emitted by high cloud. Consequently, strong IR radiative cooling is generated at the top of middle cloud.

As evident from Figure 6.6, the inclusion of IR radiation basically cools the atmosphere. However, if low cloudiness is large enough to emit a strong downward IR flux out of the cloud base, weak IR heating may be produced beneath the cloud

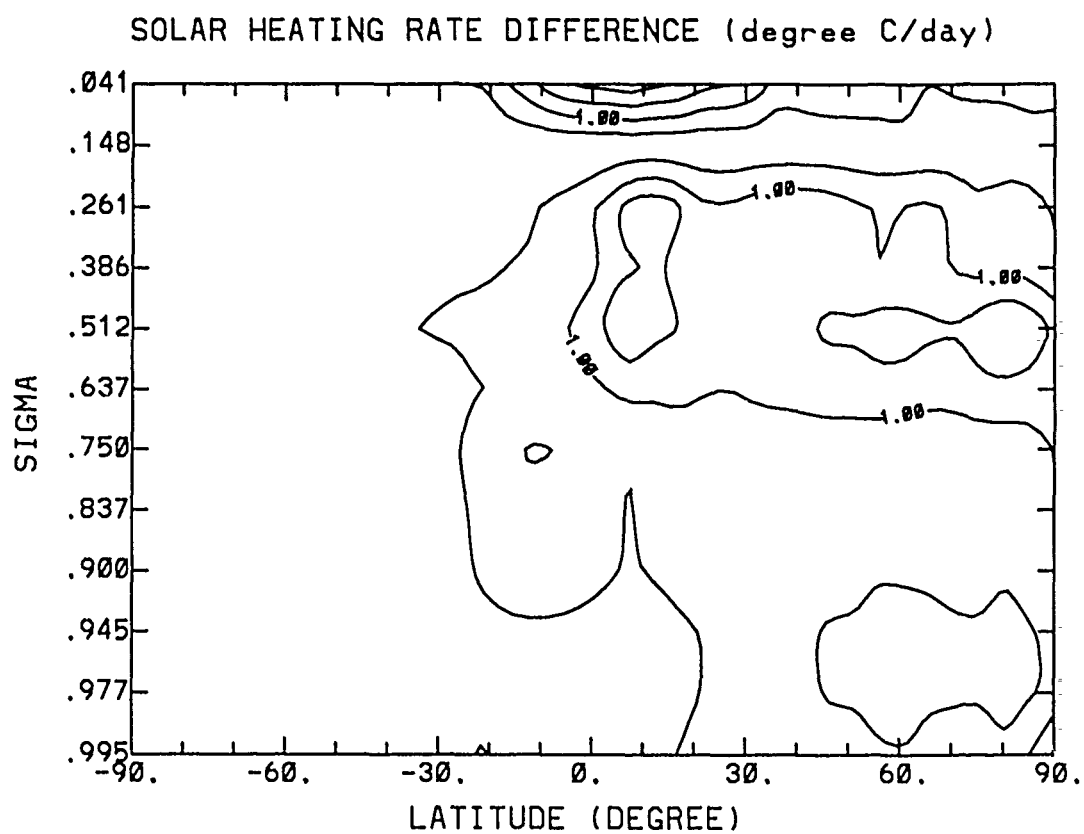


Figure 6.5. Zonally averaged differences in solar radiative heating rates. The differences are obtained by subtracting the results in EXP1 from those in CTRL.

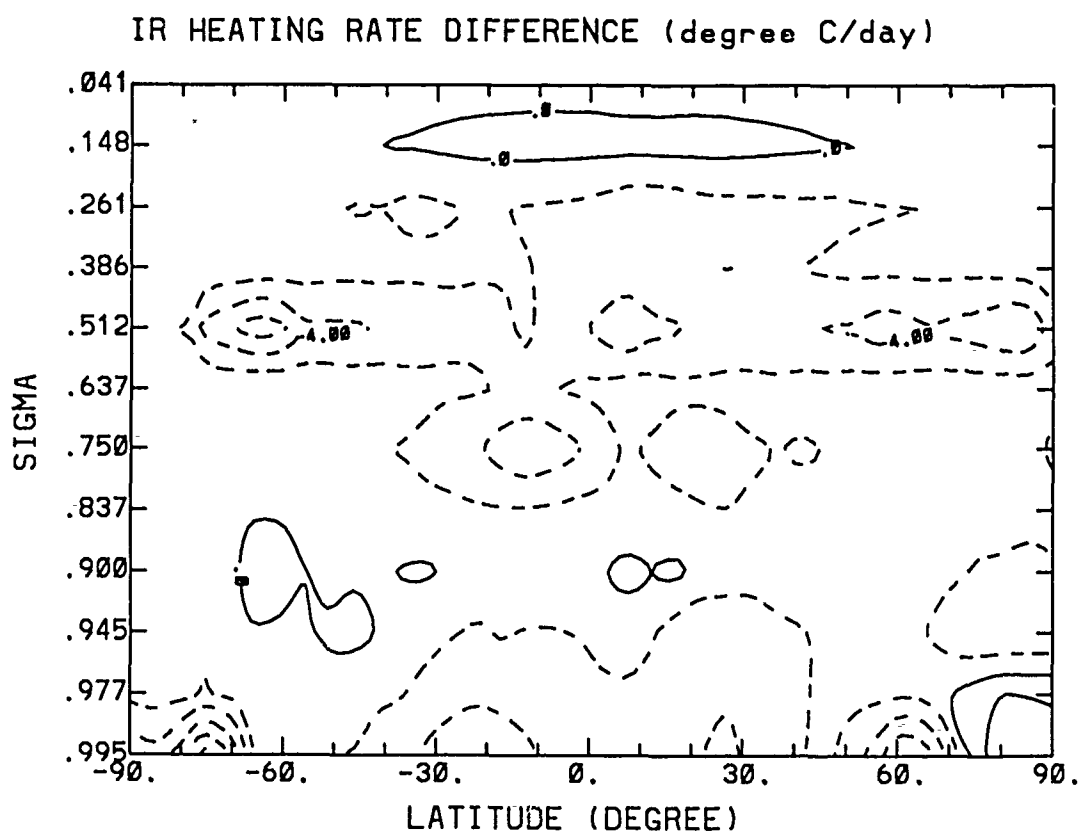


Figure 6.6. Zonally averaged differences in IR radiative heating rates. The differences are obtained by subtracting the results in EXP1 from those in CTRL.

base. This explains the two regions of weak IR heating at the low cloud bottoms at 60° S and in the tropics. Two other IR heating rates, located in the upper atmosphere in the tropics and in the lower atmosphere in the Arctic, are associated with the areas of high ozone concentration and temperature inversion in the regions, respectively.

Figure 6.7 is the same as Figure 6.5 except for the net radiative heating rates which are the combined effects of solar and IR radiation. The most important conclusion drawn from Figure 6.7 is that the inclusion of the radiative processes basically decreases the atmospheric temperature. As would be expected, the net radiation shows relatively large cooling at middle cloud tops and small cooling at cloud bottoms. However, there are weak heating rates in the low clouds in the tropics and Southern Hemisphere due to large low cloud cover over those regions. The net radiative cooling is larger in high clouds than in low clouds.

The strongest radiative cooling at the middle cloud top, located within the Antarctic Circle, is due to the absence of solar radiation in the winter season. Relatively large cooling at the low clouds within the arctic area is associated with the temperature inversion in the region, while the large cooling near the surface layers in the equatorial region is due to the contribution of water vapor continuum absorption.

It is noted that noticeable net radiative heating is located in the upper atmosphere in the Northern Hemisphere because of the ozone solar absorption in the region. The weak heating in middle clouds within the Arctic Circle is due to absorption of solar radiation during the long arctic solar day.

Figure 6.8 is the same as Figure 6.5 except for the temperature. In Figure 6.8, the major features are the strong temperature decreases at the middle cloud tops and the relatively small temperature reductions in the low clouds. This is because the radiative cooling is much stronger at a middle cloud top than a low cloud bottom.

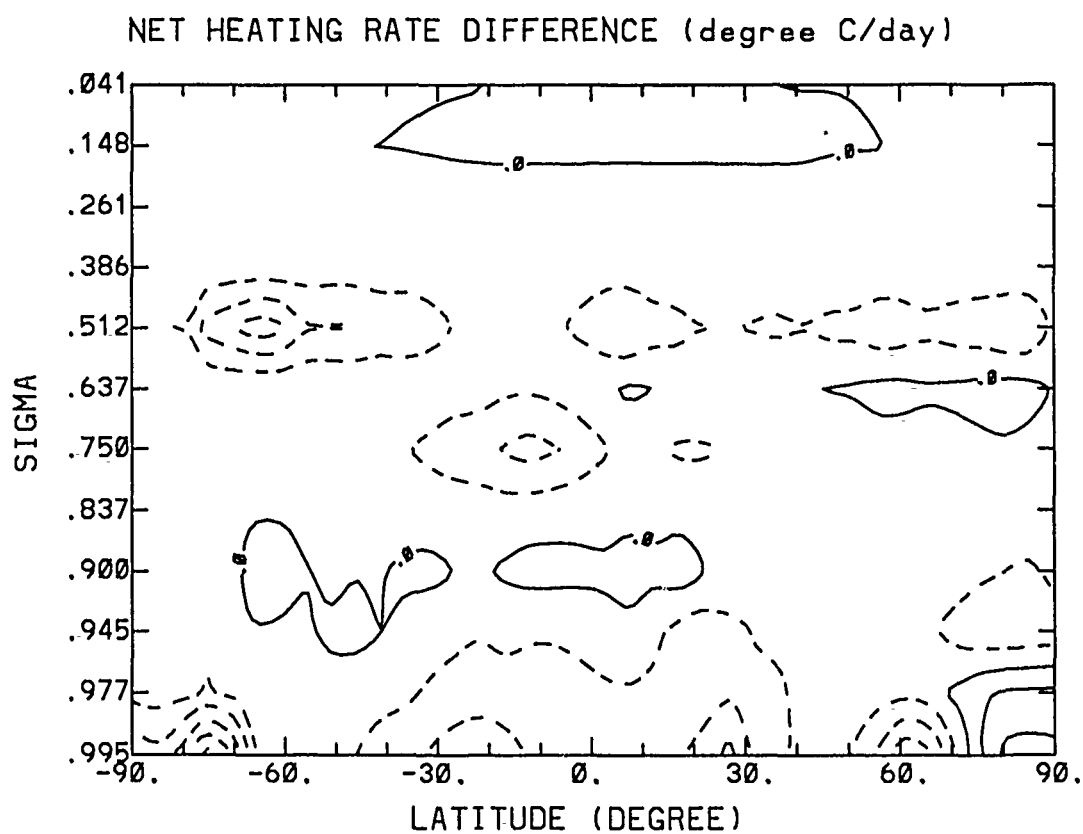


Figure 6.7. Zonally averaged differences in net radiative heating rates. The differences are obtained by subtracting the results in EXP1 from those in CTRL.

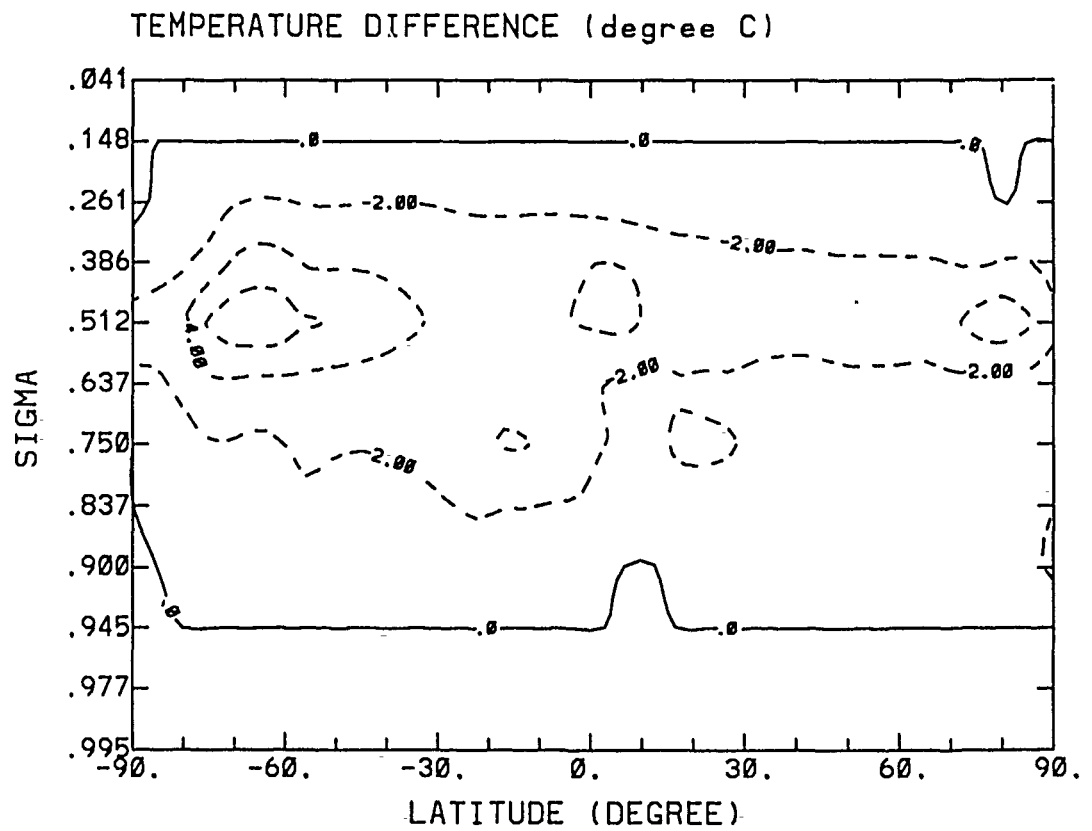


Figure 6.8. Zonally averaged differences in temperature. The differences are obtained by subtracting the results in EXP1 from those in CTRL.

The strongest temperature reduction occurs at the middle cloud top near 60° S, at which the sun does not rise above the horizon in the winter season. Temperature decreases are relatively small in the subtropical regions where small cloud amounts are located.

The inclusion of radiation decreases the atmospheric temperature; i.e., there is a cooling effect on the atmosphere. The temperature decrease is larger for cloudy sky than clear sky. These changes in temperature are contributed by the feedbacks of the net radiative cooling in Figure 6.7 through the thermodynamic equation. These temperature changes, in turn, initiate all of the changes in the cloud fields such as cloud cover, cloud LWC, and cloud IWC.

Figure 6.9 is the same as Figure 6.5 except for the differences in cloud cover. Comparisons between Figures 6.9 and 6.5 indicate that the patterns of differences in cloud cover and temperature are similar. They are related such that decreases in temperature result in increased cloud cover, and vice versa. A decrease in temperature initiates two competitive effects on the relative humidity, which ultimately determines the cloud fraction. One effect is the increase of condensation, which depletes more water vapor and results in reducing relative humidity. The other is the strong decrease of saturation vapor pressure, which greatly increases relative humidity. It is evident from the Figure 6.9 that clouds are dominated by the latter effect which results in the increase of cloud cover with decreasing temperature.

The inclusion of radiation increases cloud cover. The large increases in cloud cover occur at the middle cloud tops, in which large temperature decreases are located. The increases in low cloudiness is relatively small due to small radiative cooling associated with low clouds. However, there are two large increases of low cloud cover. One occurs in the tropics where a large amount of water vapor exists, while the other is in the arctic area where a strong inversion is located.

Figures 6.10, 6.11 and 6.12 are the same as Figure 6.5 except for the differences

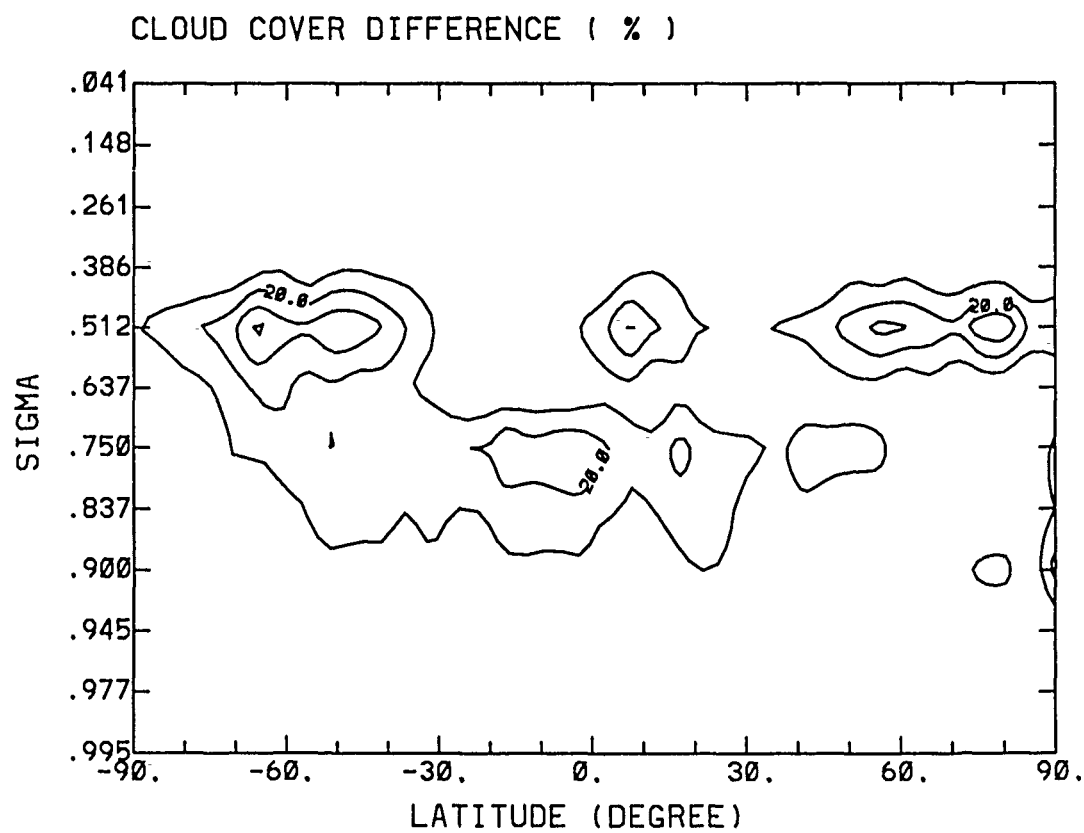


Figure 6.9. Zonally averaged differences in cloud cover. The differences are obtained by subtracting the results in EXP1 from those in CTRL.

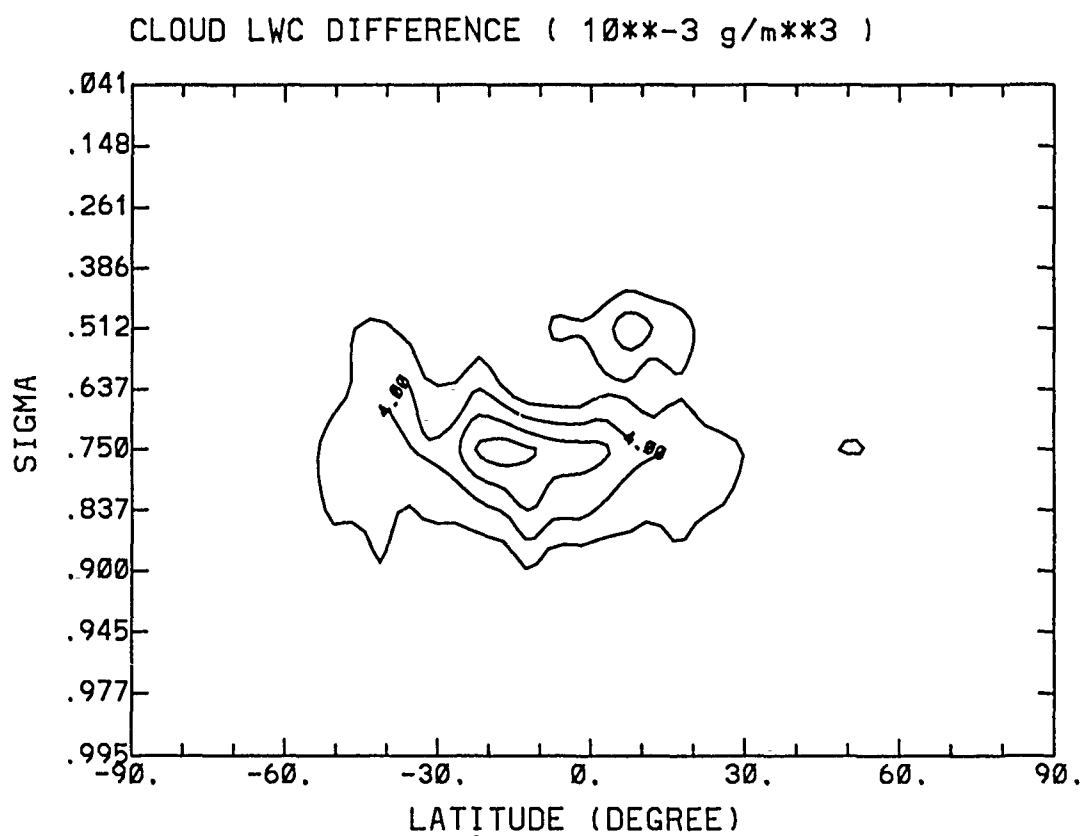


Figure 6.10. Zonally averaged differences in cloud LWC. The differences are obtained by subtracting the results in EXP1 from those in CTRL.

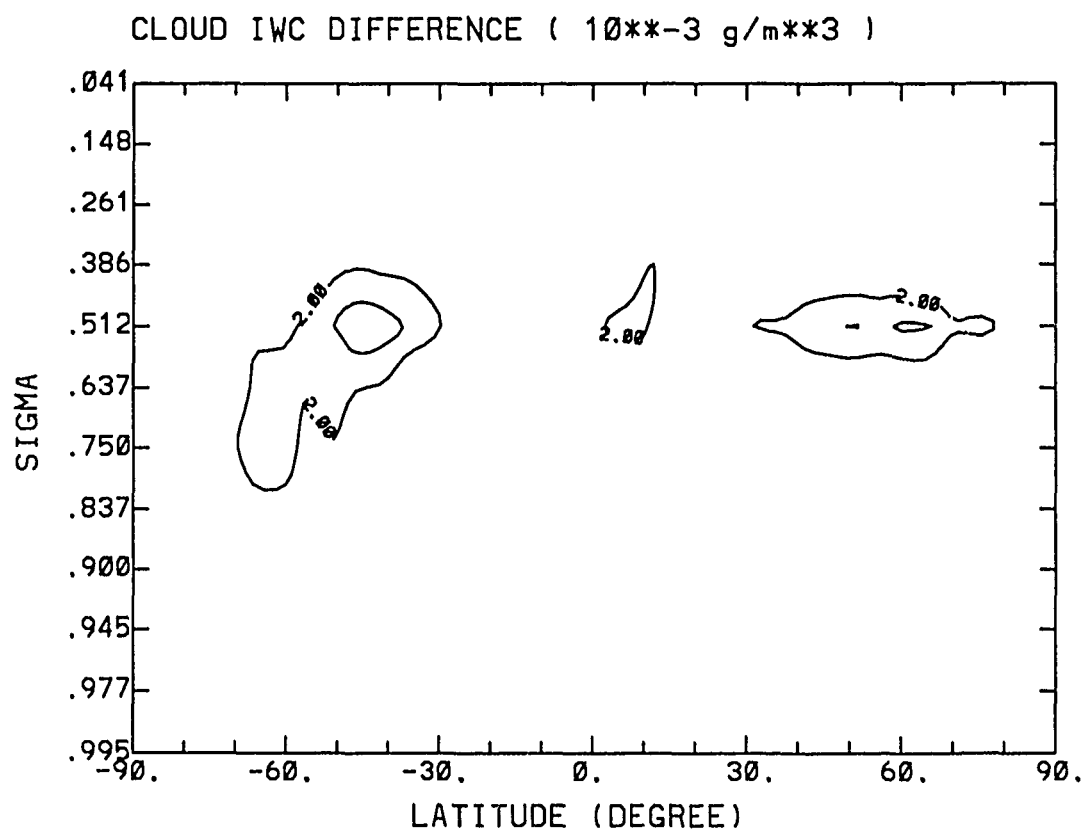


Figure 6.11. Zonally averaged differences in cloud IWC. The differences are obtained by subtracting the results in EXP1 from those in CTRL.

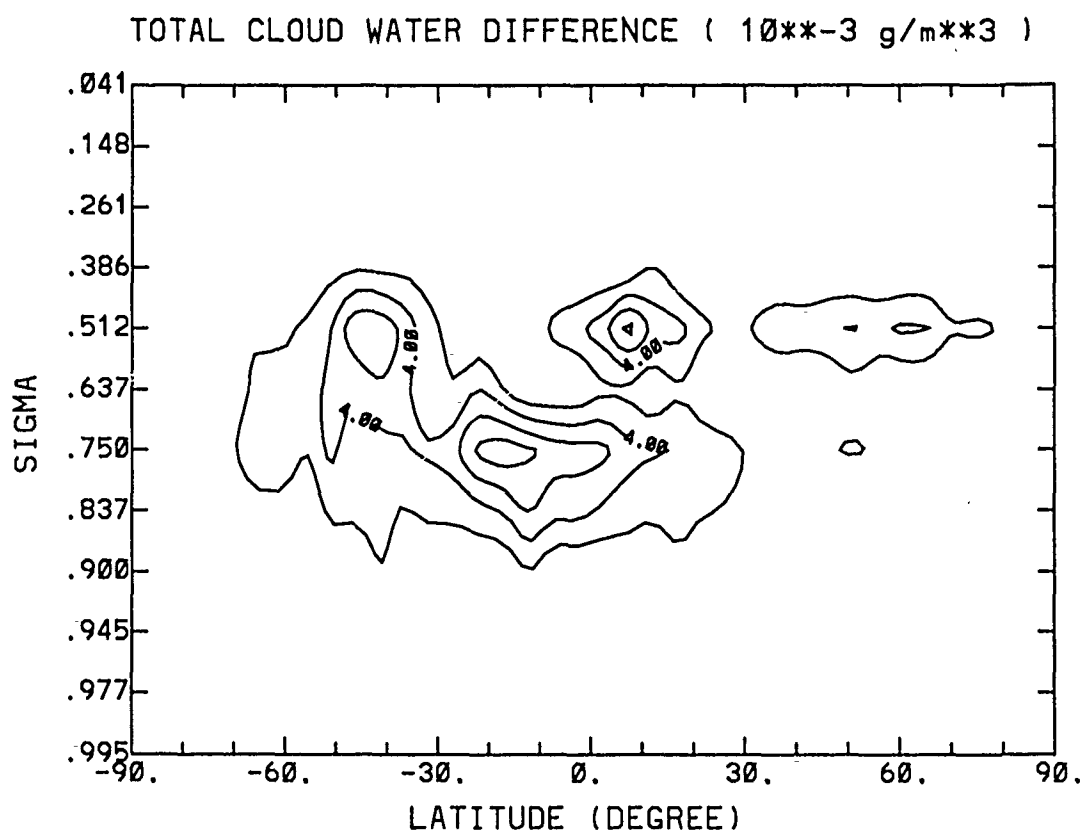


Figure 6.12. Zonally averaged differences in total cloud water. The differences are obtained by subtracting the results in EXP1 from those in CTRL.

in cloud LWC, IWC, and total cloud water content, respectively. As was mentioned, total cloud water is the combination of cloud LWC and IWC. Therefore, Figure 6.12 is the combined picture of Figures 6.10 and 6.11. Cloud water increases wherever cloud cover increases. As was mentioned previously, the decrease of cloud temperature by radiative cooling increases the condensational rate and results in the increase of total cloud water. The large increase of cloud water occurs at the tops of middle and low cloud in the tropics, where strong radiative cooling is located.

6.3 Experiment On Ice Phase Processes

Figures 6.13 - 6.17 show the results from the experiment with and without the inclusion of ice-phase processes. These figures depict the differences obtained by subtracting the results in the EXP2, i.e., without ice-phase processes, from those in the EXP1, i.e., with ice-phase processes. It is noted that radiative processes are not included in these experimental runs.

The differences in temperature and cloud cover due to the inclusion of ice-phase processes, shown in Figures 6.13 and 6.14, are insignificant. Figure 6.15 illustrates the differences in the cloud LWC between the cases with and without the inclusion of ice-phase processes. The figure shows little change in cloud LWC in the tropical low and middle clouds, in which ice clouds are less dominant. The marked reductions of cloud LWC occur in low, middle, high clouds within the Antarctic Circle, high clouds in the tropics, and middle, and high clouds within the Arctic Circle. In these regions clouds are dominated by ice crystals, which deplete the cloud LWC by the virtue of Bergeron-Findeison's processes. Figure 6.16 is the same as Figure 6.15 except for the differences in cloud IWC. Since there is no cloud IWC when ice phase processes are excluded, the differences in cloud IWC shown in Figure 6.16 are identical to the cloud IWCs shown in the control run (see, Figure 6.4).

Figure 6.17 is the same as Figure 6.15 except for the differences in total cloud water content, i.e., cloud LWC plus IWC. The differences in the total cloud water

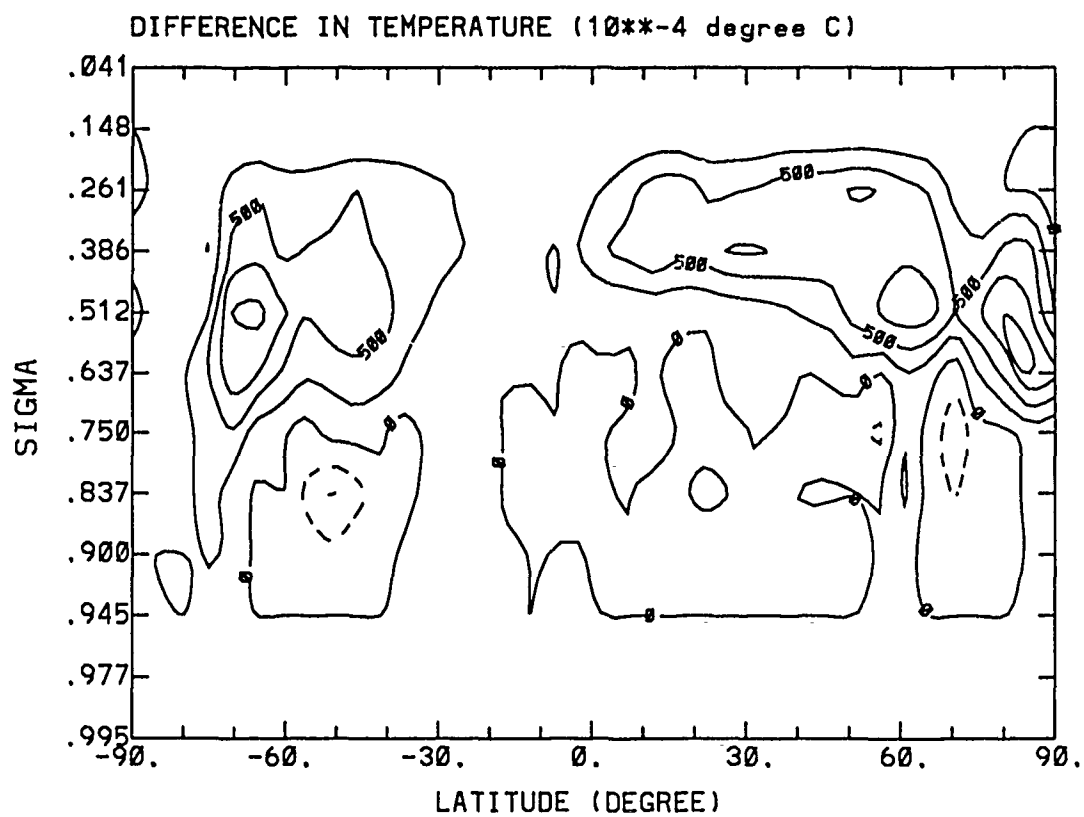


Figure 6.13. Zonally averaged differences in temperature. The differences are obtained by subtracting the results in EXP2 from those in EXP1.

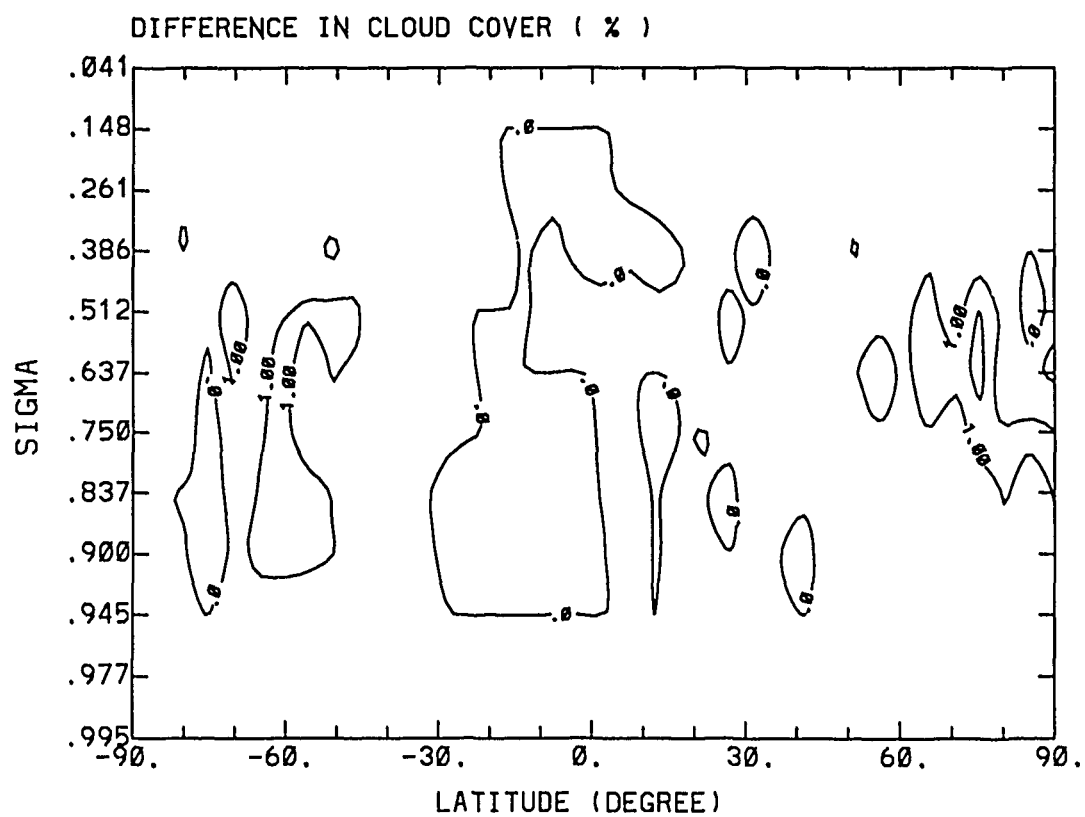


Figure 6.14. Zonally averaged differences in cloud cover. The differences are obtained by subtracting the results in EXP2 from those in EXP1.

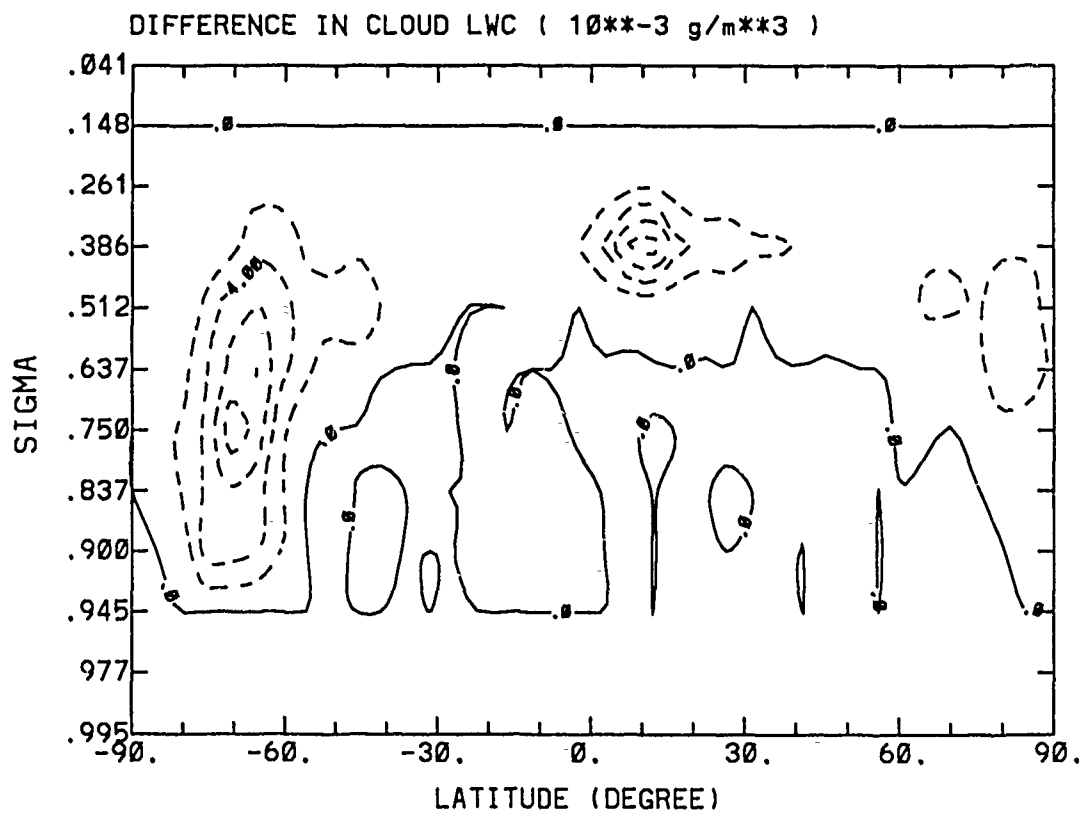


Figure 6.15. Zonally averaged differences in cloud LWC. The differences are obtained by subtracting the results in EXP2 from those in EXP1.

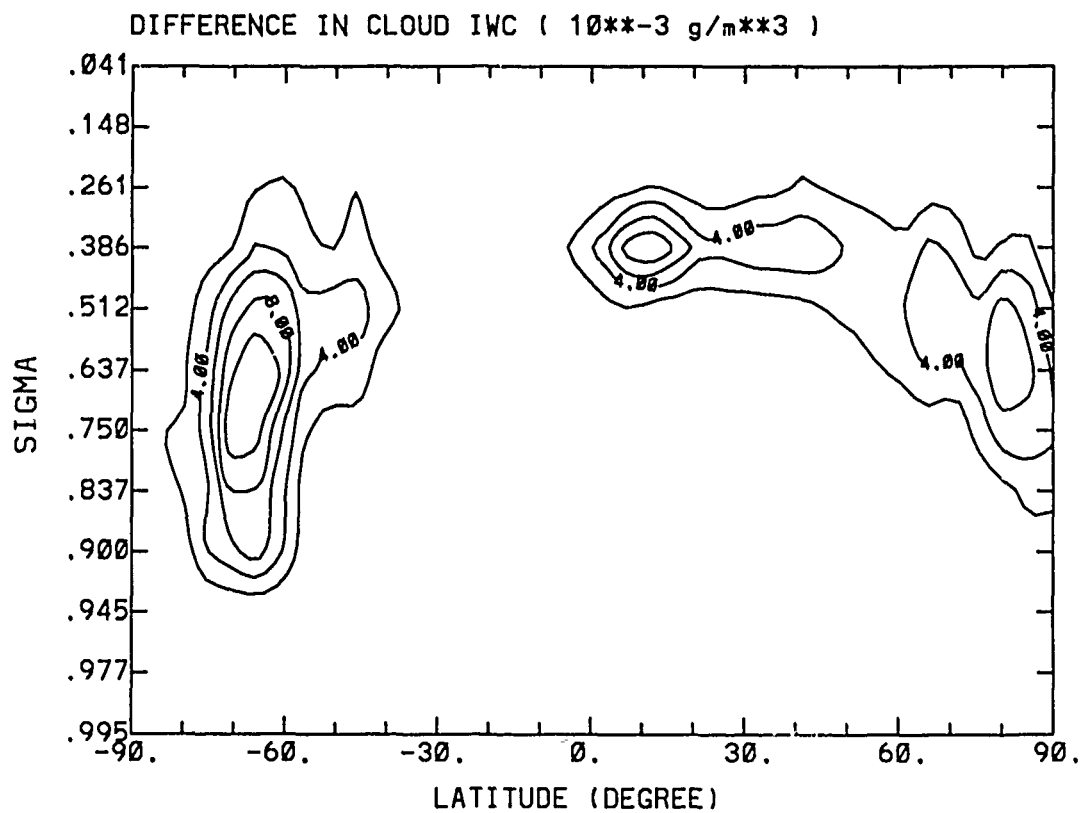


Figure 6.16. Zonally averaged differences in cloud IWC. The differences are obtained by subtracting the results in EXP2 from those in EXP1.

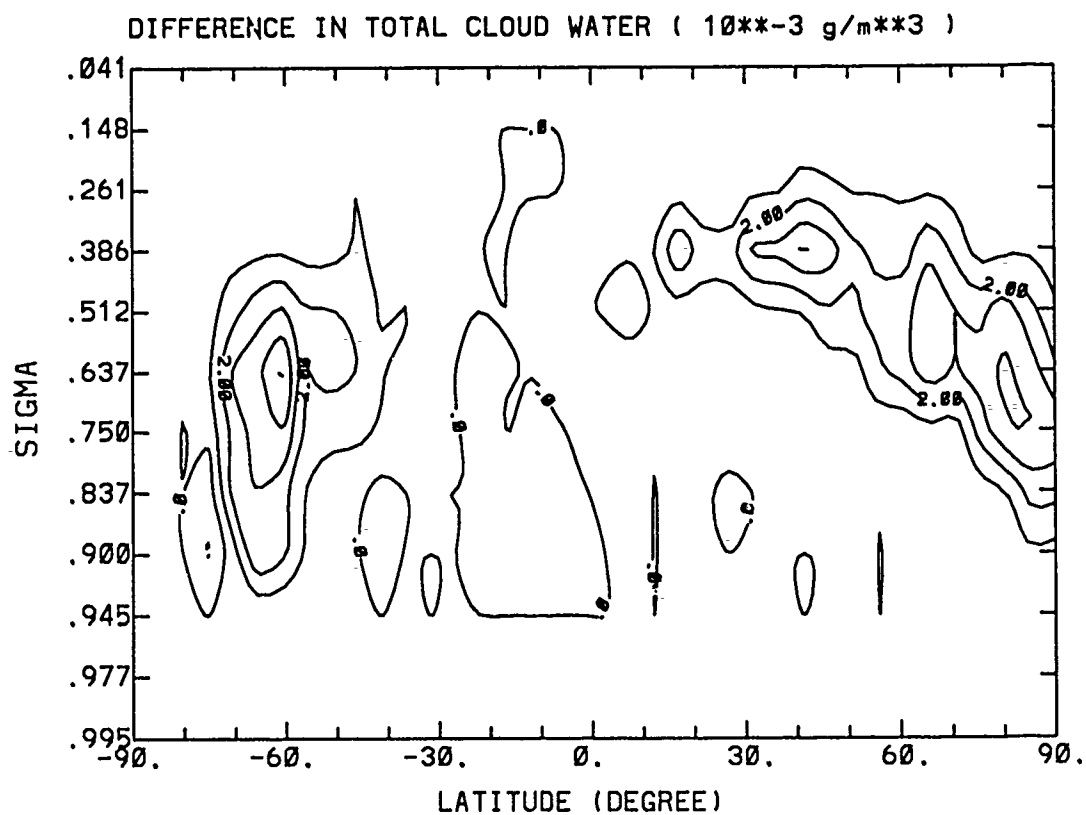


Figure 6.17. Zonally averaged differences in total cloud water. The differences are obtained by subtracting the results in EXP2 from those in EXP1.

content is expected to be smaller than in the cloud LWC, since the existence of cloud IWC compensates for the decreased cloud LWC. However, Figure 6.17 shows that the amounts of cloud IWC not only partially offset the loss of cloud LWC, but overcompensate the depleted cloud LWC in the regions where ice cloud prevails.

The maximum increases in total cloud water content occur near 60° S, 40° N, and $60^\circ - 85^\circ$ N. The increases of total cloud water when the ice phase is included indicate the existing ice crystals in these regions are not generated by the Bergeron-Findeison's processes alone. In fact, large amounts of the increased cloud IWC are due to advection. For examples, comparisons of Figures 6.17 and 6.4 indicate the maximum increase of total cloud water at 40° N corresponds to the minimum cloud IWC in the region, where the Bergeron-Findeison's processes are relatively weak. In addition, comparisons between Figures 6.17 and 4.5 suggest the maximum increases of total cloud water are associated with upward motions, i.e., convergence, near 60° S, 40° N, 65° N and 80° N.

From the above discussions, it is evident that the reduction of cloud LWC by the Bergeron-Findeison's processes is less effective than the increase of cloud IWC due to advection. This is because the simulated cloud LWC is too small to provide effective Bergeron-Findeison's processes to overcome the advection effect. For the reasons described in Section 5.4, the autoconversion rate adopted in EXP1 and EXP2 are five times larger than that used in Sundqvist (1978). The large autoconversion rate ($C_0 = 5 \times 10^{-4}$) adopted in this study is responsible for the small cloud LWC in the simulation. As was mentioned previously, the simulated cloud LWC is subject to the adopted value of the autoconversion rate; the smaller the autoconversion rate, the larger the simulated cloud LWC.

In order to further examine the effects of Bergeron-Findeison's processes on cloud formation, we have undertaken two more experimental runs with the same autoconversion rate as that used in Sundqvist (1978), i.e., $C_0 = 10^{-4}$. Thus

the simulated cloud LWC is large enough to provide strong Bergeron-Findeison's processes. In the following two experimental runs, the first run is the same as EXP1 with the smaller value of the autoconversion rate, i.e., $C_0 = 10^{-4}$; the second run is the same as the first run but without the ice phase processes.

Figures 6.18 - 6.22 are the same as Figures 6.13 - 6.17, except for the smaller value of the autoconversion rate. The temperature changes in Figure 6.18 are similar to those in Figure 6.13. However the temperature changes in the former are larger than in the latter. This indicates that the Bergeron-Findeison's processes are stronger with a smaller autoconversion rate than they are with larger rate. The differences in cloud cover, shown in Figure 6.19, are insignificant. Figure 6.20 shows a very similar pattern as Figure 6.15. Due to a smaller value of the autoconversion rate in Figure 6.20, the values of the differences for cloud LWC are about 5 times larger in Figure 6.20 than they are in Figure 6.15. The large differences in cloud LWC in Figure 6.20 indicate strong Bergeron-Findeison's processes happen when there is more cloud LWC. However, the values of cloud IWC in Figure 6.21 are close to those in Figure 6.16, even though the Bergeron-Findeison's processes are much stronger in the former than in the latter. This indicates the downward ice flux is larger in the former than in the latter.

Figure 6.22 is the same as Figure 6.20 except for the differences in total cloud water content. Figure 6.22 shows a very similar pattern as Figure 6.20. It is worth noting that in the corresponding experiments with small LWC, Figure 6.17 showed less resemblance to Figure 6.15. The only difference between Figures 6.22 and 6.17 is that there is more cloud LWC to support the Bergeron-Findeison's processes in the former than in the latter case. As a result, more cloud LWC in Figure 6.22 is converted to cloud IWC, which precipitates onto the ground by virtue of gravitational settling. Consequently, total cloud water is reduced wherever the cloud LWC is large enough to support strong Bergeron-Findeison's processes. This

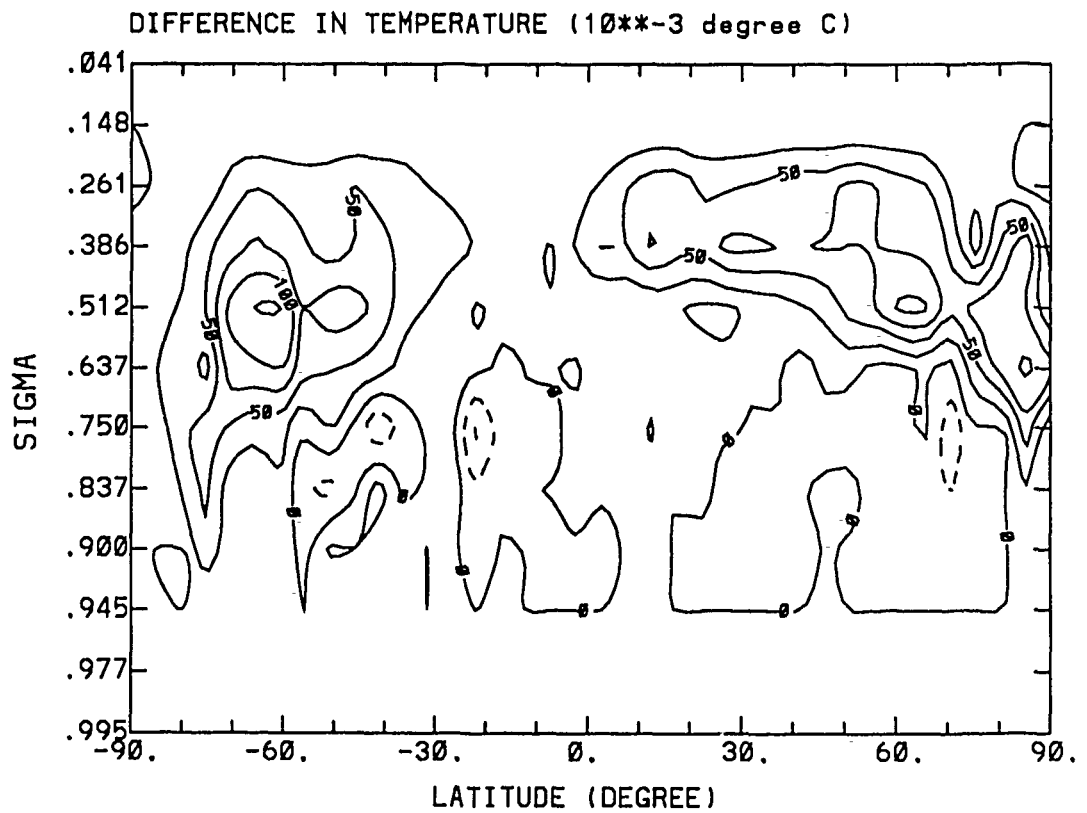


Figure 6.18. Zonally averaged differences in temperature with a small autoconversion rate ($C_0 = 10^{-4} \text{sec}^{-1}$).

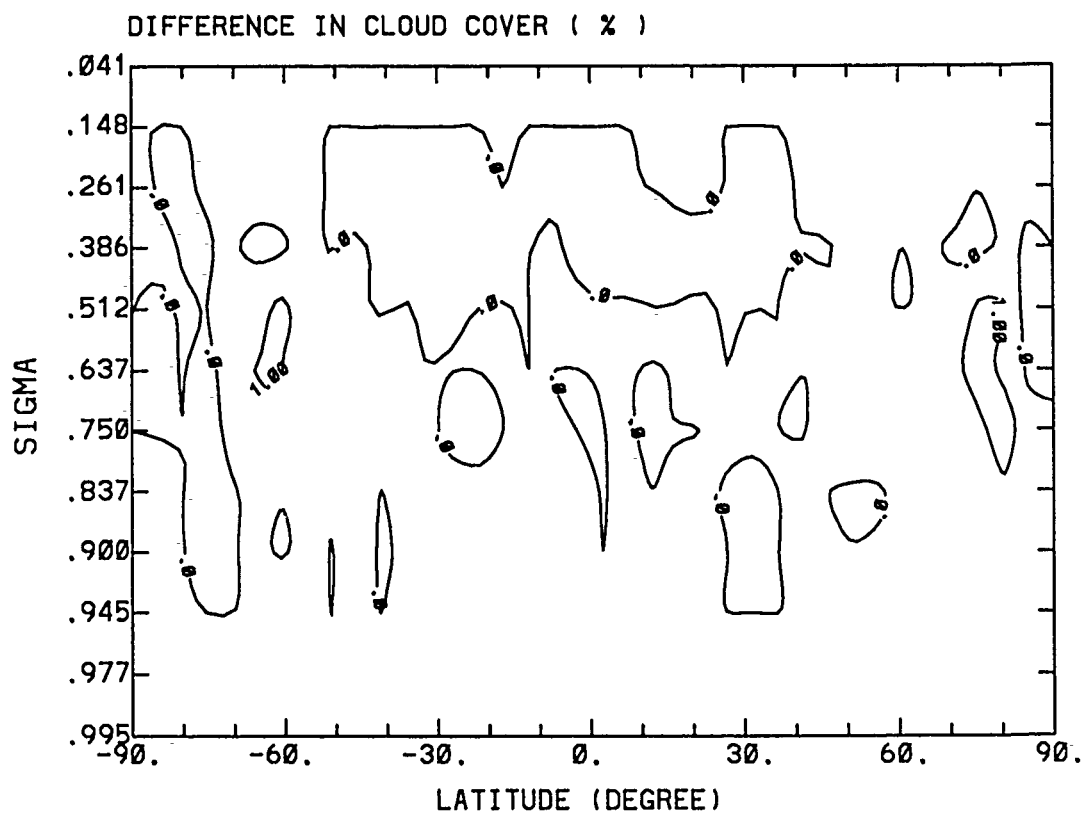


Figure 6.19. Zonally averaged differences in cloud cover with a small autoconversion rate ($C_0 = 10^{-4} \text{sec}^{-1}$).

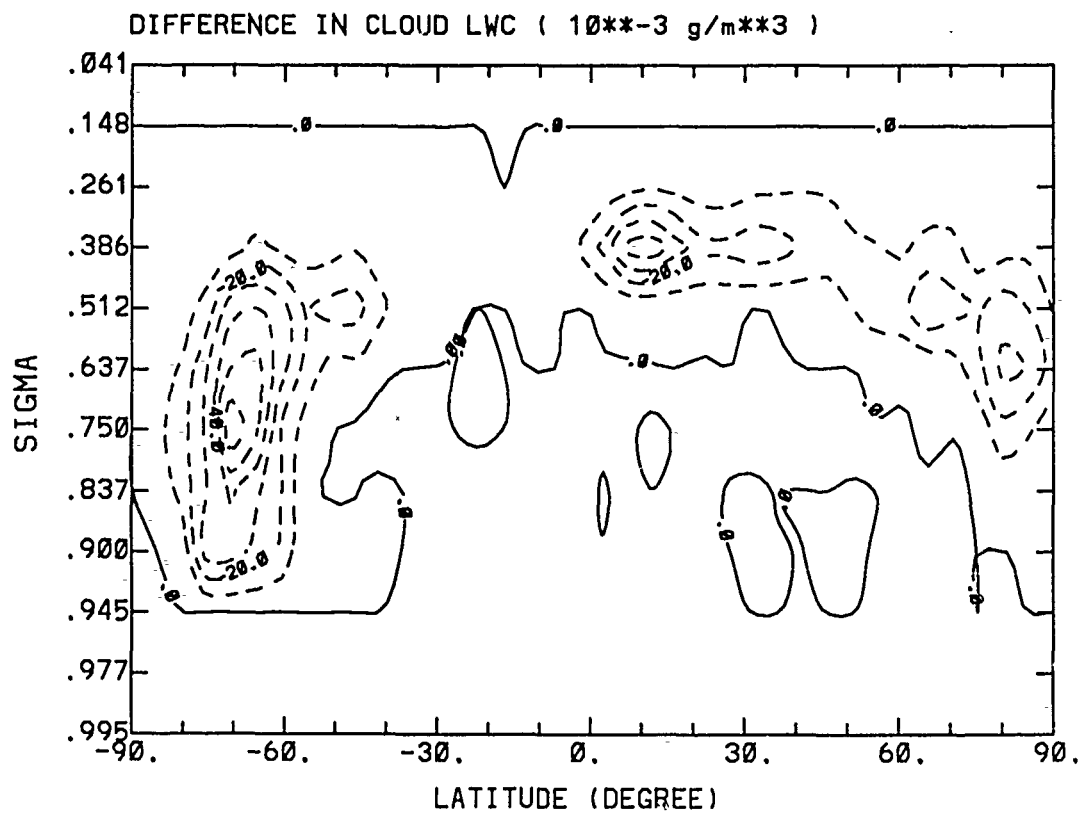


Figure 6.20. Zonally averaged differences in cloud LWC with a small autoconversion rate ($C_0 = 10^{-4} \text{sec}^{-1}$).

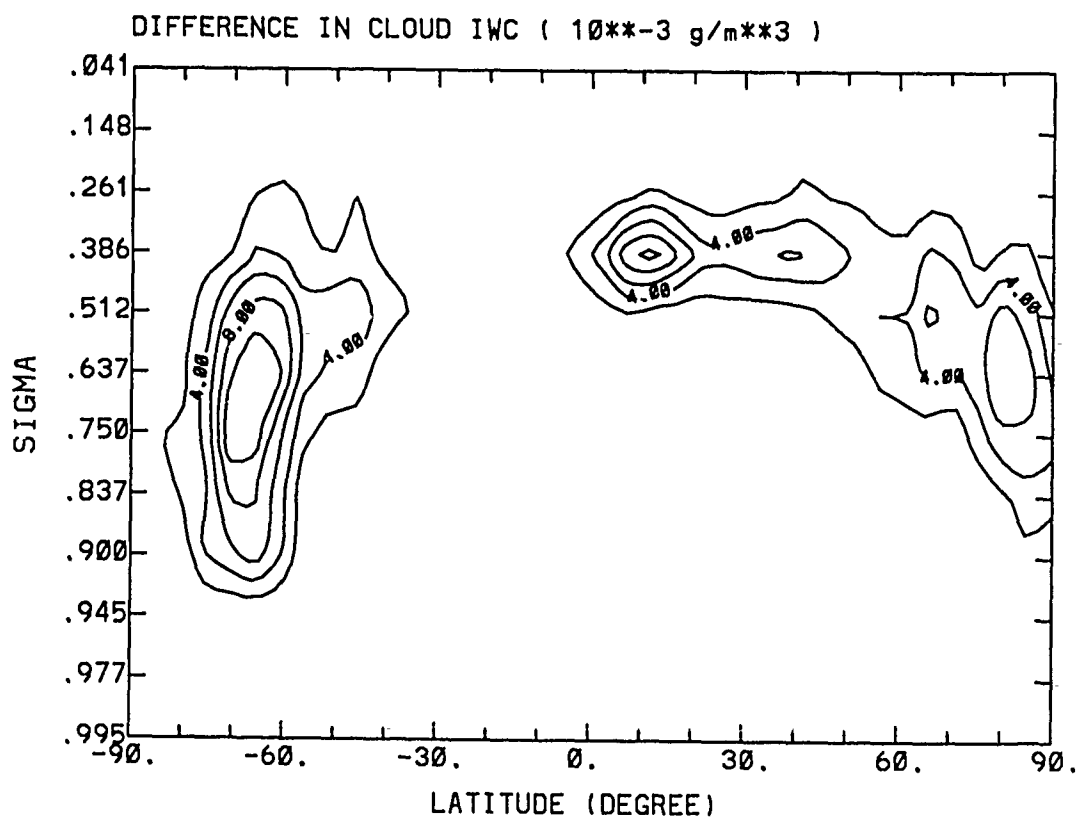


Figure 6.21. Zonally averaged differences in cloud IWC with a small autoconversion rate ($C_0 = 10^{-4} \text{ sec}^{-1}$).

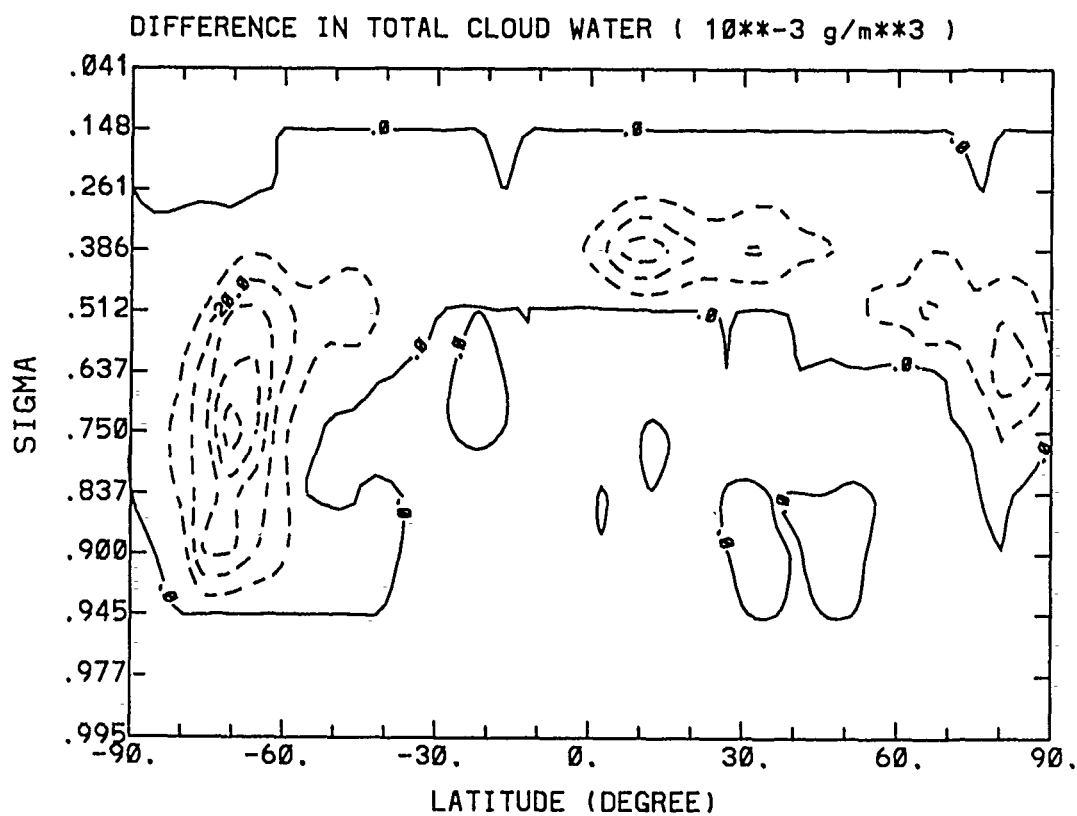


Figure 6.22. Zonally averaged differences in total cloud water with a small auto-conversion rate ($C_0 = 10^{-4} \text{ sec}^{-1}$).

may explain the increase of total cloud water in Figure 6.17 due to the small cloud LWC in the simulation.

Comparisons between Figures 6.22 and 6.20 indicate the differences in the total cloud water content are smaller than those in the cloud LWC, since the existence of cloud ice content represents part of the depleted cloud LWC. The total cloud water content decreases in the region where ice clouds are present. The reduction of the total cloud water content is mainly controlled either by autoconversion that converts cloud LWC into precipitation or by gravitational settling that removes ice crystals from the cloud layer. The decrease of total cloud water content when the ice phase processes are included indicates that gravitational settling is an efficient mechanism for reducing the cloud IWC.

Section 7

SUMMARY AND CONCLUSION

A time-dependent, three-dimensional, large-scale cloud-moisture model was developed for the prediction of water vapor, cloud LWC, cloud IWC, precipitation and temperature. The first four variables are governed by the law of mass conservation. The latent heat exchanges during the phase transitions of the water substances are ruled by the first law of thermodynamics through the temperature field. The large-scale cloud cover is diagnostic based on the model-predicted relative humidity. Partial cloudiness is allowed to form when large-scale relative humidity is less than 100%. In the vertical, a 16-layer z-coordinate is adopted. The horizontal resolution is described by 48 equally-spaced longitudinal points and 38 Gaussian latitudes.

The cloud microphysical processes simulated in the model include liquid phase as well as ice phase, which is physically included for the first time in a large-scale cloud model in order to simulate cirrus clouds. The liquid phase processes consist of evaporation, condensation, autoconversion, and precipitation. The ice-phase processes include heterogeneous nucleation to generate ice crystals, depositional growth to simulate Bergeron-Findeison's processes, sublimation to deplete ice crystals, and gravitational settling to remove ice crystals from clouds. The Bergeron-Findeison's processes occur primarily at temperatures between 0°C and -40°C , while homogeneous nucleation dominates below -40°C . Gravitational settling is established by mean volume-weighted downward ice flux, which is obtained by integrating the falling velocity and mass of an individual ice crystal over the whole spectrum of ice crystals.

The radiative transfer program is based on a broadband method and involves the transfer of IR and solar radiation in clear and cloudy regions. In a cloudy atmosphere, low and middle clouds are treated as blackbodies in the infrared radiative transfer calculations. The broadband IR emissivity, reflectivity, and transmissivity for cirrus clouds as well as the broadband solar absorption, reflection, and transmission values for various cloud types are computed based on the parameterizations developed by Liou and Wittman(1979). To perform radiative transfer calculations and to compare with observed cloudiness, the model-predicted cloud covers are strapped into low, middle and high clouds, which overlap each other in a statistically random manner.

Large amounts of satellite data, including the cloud climatology (3DNEPH) and the Earth Radiation Budget (ERB) data, have been processed into formats appropriate for verification. The SMMR data consisting of vertically integrated liquid water content are used to verify model-predicted cloud LWC. In addition, the cloud cover climatology compiled by London (1957) based on surface observations is adopted as a complementary verification dataset to assess the model-predicted cloud cover in the arctic and antarctic regions, where the satellite observational cloud covers are very inaccurate because 3DNEPH has not been able to distinguished cold surfaces from clouds aloft.

A 96-hour model simulation, with the initial conditions taken at 12Z on July 1, 1979, has been carried out to assess the performance of the large-scale cloud model. The wind field is prescribed using the results from the AFGL GCM. Thus, there is no cloud-radiation feedback to the dynamic structure. In the simulation, the cloud model forecasts cloud cover, cloud LWC and IWC, which are interactively input into the radiation model. The radiation model calculates radiative heating/cooling rates based on the prediction cloud properties. The radiative heating/cooling rates, in turn, feed back to the cloud model through the thermodynamic equation, and

modify the cloud fields. Thus, cloud-radiation interaction through the medium of the cloud cover, cloud LWC and IWC is accomplished with the aid of the large-scale cloud model. In addition, the radiation model computes OLR and net solar flux at TOA to be compared with the ERB products.

The comparisons between the model simulation and the satellite observations indicate the large-scale cloud model is capable of realistically simulating zonal means and geographical distributions of cloud fields, including cloud cover, OLR and net solar flux at TOA, and cloud LWC. Differences in the zonal mean total cloud cover between the simulation and the 3DNEPII data are generally within 10% of total cloudiness. Generally, the simulated OLR and net solar flux at TOA are within 10 and 20 W/m² of the ERB results, respectively. The zonal mean values of simulated cloud LWP compare quite well with the SMMR observations, with differences being less than 5 mg/cm², which is the accuracy of the SMMR data. However, it is clearly indicated that the model underestimates cloud cover and cloud LWC and overestimates the OLR in the tropics, where clouds are predominantly convective clouds, which are not simulated in this model.

In the geographical distributions of cloud fields, the large-scale cloud model has successfully simulated the large cloud bands in the ITCZ, monsoon areas, SPCZ, and the mid-latitude storm tracks, although the ITCZ cloud band is less pronounced in the simulation. At the subtropical highs, areas of small cloudiness over southern Africa and northern Africa, and North and South America are clearly identified in both of the observations and the model simulation. The simulated precipitation on the east coast of America is in contrast to that on the west coast; i.e., the model produces large amounts of precipitation on the east coast but little precipitation on the west coast.

The model-simulated cloud fields are strongly tied to large-scale circulations. Strong low-level wind convergences and deep moist tropospheres in the ITCZ and

monsoon areas assist in the formation of large cloud amounts in these regions. Great baroclinic instability in the mid-latitude storm tracks aids in the formation of large amounts of cloud in these areas. The clear-sky conditions at the subtropical highs are associated with the large-scale subsidence in the branches of downward motion in the Hadley cell. The downward motion acts to prevent water vapor from condensing and greatly reduces the possibility of the cloud formation. In brief, upward motion supports cloud formation, while downward motion favors cloud depletion.

Observing the model-predicted cloud fields, such as cloud cover, OLR and net solar flux at TOA, cloud LWC and precipitation, we find these cloud properties are closely related one another. Large amounts of cloud cover coincide with abundant cloud LWC, which generates large precipitation rates by virtue of the autoconversion process simulated in the model. In addition, the model simulation demonstrates the consistency between the simulated OLR and net solar flux at TOA. For instance, both of them are small over the ITCZ and monsoon areas, and large in the regions of the subtropical highs. In summary, the atmospheric moisture and cloud fields are linked together by the cloud microphysical processes simulated in the cloud model. More importantly, the moisture, cloud fields and earth's radiation budget are physically related to large-scale thermal and dynamical structures, such as temperature and vertical velocity.

The magnitude of the cloud IWC in the simulation is about 0.01 g/m^3 , which is consistent with the aircraft measurements in cirrus clouds as well as with other model results. The maxima of cloud IWC occurs along the -15° C temperature line, where the Bergeron-Findeison's processes dominate. This result agrees well with the cloud-microphysics laboratory experiment which indicated the maximum ice crystal depositional rate occurred at -15° C due to a large vapor pressure difference and a large capacitance value at this temperature. Because of the strong

temperature dependence of the ice crystal growth rate, the simulated cloud IWC appears to depend more on temperature than on vertical velocity, which is essential to the condensational process.

The latitudinal distribution of cloud IWC appears to be realistic. In the antarctic area, all of the low, middle and high clouds are ice clouds. However, in the Arctic, only middle and high clouds are ice clouds. In the tropics, only high clouds contain ice crystals. The simulated cloud LWCs prevail in low and middle clouds at the middle-low latitudes where the temperature is warm and abundant moisture is available for condensation.

Sensitivity studies have been performed to examine the effects of radiative heating fields and ice-phase cloud microphysics on large-scale cloud formation. Numerical experiments have been carried out with and without the inclusion of radiation and ice-phase processes. The inclusion of radiative processes in cloud formation overwhelmingly decreases the cloud temperature, with the strongest cooling occurring at the middle cloud top. However, there may be weak heating located in a low cloud if cloud cover is large enough to produce a strong downward flux. The decrease of temperature by radiative cooling increases the atmospheric relative humidity and condensation in clouds. As a result, cloud cover and total cloud water, including cloud LWC and IWC, increase due to the inclusion of radiative processes.

The inclusion of ice-phase processes has a greater effect on the cloud LWC and IWC than on the temperature field. The differences in cloud cover due to the inclusion of ice phase are insignificant. Due to the release of latent heat in the Bergeron-Findeison's processes, temperature increases occur in the regions where the cloud IWCs prevail.

The changes of the total cloud water due to the inclusion of the ice phase is complicated by the dependence of depositional growth on the amount of cloud LWC. An ice crystal's growth is stopped if there is no cloud water to supply water

vapor. If the cloud LWC is large enough to support effective Bergeron-Findeison's processes, the total cloud water content decreases in the regions where ice clouds dominate. The reduction of the total cloud water content is mainly controlled either by autoconversion which converts cloud LWC into precipitation, or by gravitational settling, which removes ice crystals from the cloud layer. The decrease of total cloud water content when the ice-phase processes are included indicates that gravitational settling is an efficient mechanism for reducing the cloud IWC.

APPENDIX A

DERIVATION OF PRECIPITATION EQUATION IN (2.5)

The mass conservation equation for rain water, \bar{q}_r , may be written as follow:

$$\begin{aligned} \frac{\partial}{\partial t}(\bar{\rho}\bar{q}_r) + \frac{1}{a\cos\phi} \left[\frac{\partial}{\partial \lambda}(\bar{\rho}\bar{q}_r\bar{u}) + \frac{\partial}{\partial \phi}(\bar{\rho}\bar{q}_r\bar{v}\cos\phi) \right] + \frac{\partial}{\partial z}[\bar{\rho}\bar{q}_r(\bar{w} - \bar{w}_r)] \\ = -\bar{\rho}\eta\bar{P} - (1 - \eta)\bar{\rho}\bar{E}_r \end{aligned} \quad (\text{A.1})$$

The symbols in this equation are defined in Chapter 2. The raindrop terminal velocity is denoted as \bar{w}_r , which is govern by the gravitational force and drag force exerted on the raindrop. This equation may be further simplified based on the following scale arguments consideration.

The magnitude of the raindrop terminal velocity, \bar{w}_r , may be estimated by assuming a balance between the gravitational force and drag force exerted on the raindrop. Rogers (1979) derived the following terminal velocity for raindrops.

$$\bar{w}_r = 2.2 \times 10^3 (\rho_0/\rho)^{1/2} (r)^{1/2} , \quad (\text{A.2})$$

where ρ is the air density and ρ_0 is the reference air density of 1.2×10^{-3} g/cm³, and r the radius of a raindrop. At 700 mb, ρ is roughly estimated as 0.9×10^{-3} g/cm³. Based on Equation (A.2), the terminal velocity for a raindrop with 0.6 mm radius is about 6 m/s, i.e., on the order of 10^0 m/s.

Scale analysis is a suitable method for evaluating the magnitudes of various terms in the governing equations for a particular space-time domain. In the scale analysis,

a large-scale motion is defined by the following characteristic length, depth, and time scales.

$$\begin{aligned} L &\sim 10^6 \text{ m} , \\ V &\sim 10^1 \text{ ms}^{-1} , \\ D &\sim 10^4 \text{ m} , \\ W &\sim 10^{-2} \text{ ms}^{-1} , \\ T = L/V &\sim 10^5 \text{ s}^{-1} , \\ W_r &\sim 10^0 \text{ ms}^{-1} , \end{aligned}$$

where L and D denote the horizontal and vertical geometry scale, respectively. V , W , and T are the typical scale values of horizontal velocity, vertical velocity, and the life span of large-scale motions, and W_r is the order of raindrop terminal velocity.

We can now estimate the magnitudes of the following terms in Equation (A.1) as follows:

$$\begin{aligned} \frac{\partial}{\partial z}[\bar{\rho}\bar{q}_r(\bar{w} - \bar{w}_r)] &\sim \frac{\partial}{\partial z}[\bar{\rho}\bar{q}_r(-\bar{w}_r)] \\ \frac{\partial(\quad)}{\partial t} &\sim \frac{V}{L} \sim 10^{-5} \text{ s}^{-1} \\ \frac{1}{a \cos \phi} \left[\frac{\partial}{\partial \lambda}((\quad)\bar{u}) + \frac{\partial}{\partial \phi}((\quad)\bar{v} \cos \phi) \right] &\sim \frac{V}{L} \sim 10^{-5} \text{ s}^{-1} \\ \frac{\partial}{\partial z}[(\quad)\bar{w}_r] &\sim W_r/D \sim 10^{-4} \text{ s}^{-1} . \end{aligned}$$

The above scale analysis shows that the time tendency and horizontal advection terms in Equation (A.1) are about an order of magnitude smaller than the downward flux of precipitated rain water, i.e., $-\bar{\rho}\bar{q}_r\bar{w}_r$. To a good approximation, the horizontal advection and time tendency of rain water may be neglected due to the large falling velocity of rain water. Therefore, the rain water budget equation may be rewritten as follows:

$$-\frac{\partial}{\partial z}(\tilde{P}) = \bar{\rho}\eta\bar{P} - (1 - \eta)\bar{\rho}\bar{E}_r ; \text{ where } \tilde{P} \equiv \bar{\rho}\bar{q}_r\bar{w}_r .$$

APPENDIX B

DERIVATION OF LARGE-SCALE CONDENSATION

The large-scale condensation, \bar{Q} , is related to the time rate of change of the saturation vapor pressure as follows:

$$\bar{Q} = -\frac{d\bar{q}_s}{dt} ,$$

where the saturation specific humidity, \bar{q}_s , is given by

$$\bar{q}_s(\bar{T}) \cong \frac{\varepsilon e_s(\bar{T})}{P} , \quad (\text{B.1})$$

here $\varepsilon = 0.622$ and $e_s(\bar{T})$ is a saturation vapor pressure, which is related to a large-scale temperature by the Clausius-Clapeyron equation

$$\frac{de_s}{e_s} = L d\bar{T} / R_v \bar{T}^2 . \quad (\text{B.2})$$

Differentiation of Equation (B.1) and substitution from Equation (B.2) leads to

$$\frac{1}{q_s} \frac{d\bar{q}_s}{dt} = \frac{L}{R_v \bar{T}^2} \frac{d\bar{T}}{dt} - \frac{1}{P} \frac{dP}{dt} . \quad (\text{B.3})$$

Furthermore, the thermodynamic equation gives

$$-\frac{d\bar{q}_s}{dt} = \frac{C_p}{L} \frac{d\bar{T}}{dt} - \frac{R_a}{L} \frac{\bar{T}}{P} \frac{dP}{dt} . \quad (\text{B.4})$$

Eliminating $d\bar{T}/dt$ between Equations (B.3) and (B.4), we obtain

$$\frac{d\bar{q}_s}{dt} = \bar{q}_s \bar{T} \left[\frac{LR_a - C_p R_v \bar{T}}{C_p R_v \bar{T}^2 + \bar{q}_s L^2} \right] \frac{\omega}{P} ,$$

where ω is the vertical velocity in the pressure coordinate, i.e., $\omega \equiv \frac{dP}{dt}$. In large scale motions, it is assumed $\omega \sim -\rho g \bar{w}$, based on the hydrostatic equation.

Therefore, the large-scale condensation in our model is given by

$$Q = -\frac{d\bar{q}_s}{dt} = \Gamma_d \frac{\bar{q}_s(\bar{T})}{R_a} \left[\frac{LR_a - C_p R_v \bar{T}}{C_p R_v \bar{T}^2 + \bar{q}_s L^2} \right] \bar{w} ,$$

where Γ_d is the dry adiabatic lapse rate, i.e., g/C_p .

APPENDIX C

PARAMETERIZATION OF RAINDROPS EVAPORATION

For a unit volume of air, the rate of evaporation of raindrops can be obtained by integrating the evaporation of an individual raindrop over the whole spectrum of raindrops. This is expressed by

$$E_r = f \int_0^{\infty} \left[\frac{1}{\rho} \frac{dm_r}{dt} \right] n dD , \quad (C.1)$$

where f , m_r , n and D are the ventilation factor, the mass of the individual raindrop, the number of raindrops per unit volume of air per unit diameter range δD , and the raindrop diameter, respectively.

The rate of change in the mass of an individual spherical raindrop may be derived from Fick's law and formulated as follows:

$$\frac{dm_r}{dt} = 2\pi\rho D D_d (q_s - q_0) , \quad (C.2)$$

where D_d is the mass diffusivity of water vapor in air.

It is assumed that the distribution of raindrops, n , follows the Marshall-Palmer (1948) distribution throughout the whole process of evaporation. This distribution is given by

$$n = n_0 e^{-\lambda D} , \quad (C.3)$$

where n_0 and λ are constants which are determined empirically. Substituting Equations (C.2) and (C.3) into Equation (C.1), we obtain

$$E_r = 2\pi D_d (q_s - q_0) n_0 \lambda^{-2} f . \quad (C.4)$$

To relate E_r with the total precipitation flux, \tilde{P} , we adopt the following relation:

$$\tilde{P} = \int_0^\infty w_r \frac{\pi}{6} D^3 \rho_w n_0 e^{-\lambda D} dD , \quad (\text{C.5})$$

where w_r is the raindrop terminal velocity, which can be approximated by the following equation (Rogers, 1977),

$$\bar{w}_r = 2.2 \times 10^3 (\rho_0/\rho)^{1/2} (D/2)^{1/2} , \quad (\text{C.6})$$

where ρ is the air density and ρ_0 is the reference air density of 1.2×10^{-3} g/cm³. Using the Marshall-Palmer size distribution, we obtain the following:

$$\lambda = 4.529 \tilde{P}^{-0.21} . \quad (\text{C.7})$$

Substituting Equation (C.7) into Equation (C.4), leads to

$$E_r = 5.54 \times 10^{-3} q_s (1 - r_0) \tilde{P}^{0.42} f ,$$

where we have used a value of 0.226 cm²/sec, for the water vapor diffusion in air, D_d , at 0° C. Let $K_E = 5.54 \times 10^{-3} q_s f$; then we have

$$E_r = K_E (1 - r_0) \tilde{P}^{0.42} .$$

REFERENCES

- Arking, A., and S. Vemury, 1984: The Nimbus 7 ERB data set: A critical analysis. J. Geophys. Res., **89**, 5089-5097.
- Beard, K.V., and H.R. Pruppacher, 1969: A determination of the terminal velocity and drag of small water drops by means of a wind tunnel. J. Atmos. Sci., **26**, 1066-1072.
- Byers, H.R., 1965: Elements of cloud physics. University of Chicago Press, 191 pp.
- Cess, R.D., 1976 : Climate change : An appraisal of atmospheric feedback mechanisms employing zonal climatology. J. Atmos. Sci., **33**, 1831-1843.
- Cess, R.D., B.P. Briegleb, and M.S. Lian, 1982: Low-latitude cloud amount and climate feedback: Comparative estimates from satellite data. J. Atmos. Sci., **39**, 53-59.
- Cess, R.D., G.L. Potter, J.P. Blanchet, G.J. Boer, S.J. Ghan, J.T. Kiehl, H. Le Treut, Z.-X. Li, X.-Z. Liang, J.F.B. Mitchell, J.-J. Morcrette, D.A. Randall, M.R. Riches, E. Roeckner, U. Schlese, A. Slingo, K.E. Taylor, W.M. Washington, R.T. Wetherald, and I. Yagai, 1989: Interpretation of cloud-climate feedback as produced by 14 atmospheric general circulation model. Science, **245**, 513-516.
- Del Genio, A.D., and M.S. Yao, 1990: Predicting cloud water variations in the GISS GCM. Preprint, The Seventh Atmospheric Radiation Conference, San Francisco, July 23-27.
- Geleyn, J.F., 1981: Some diagnostics of the cloud/radiation interaction in ECMWF forecast model. In Proceedings of Workshop on Radiation and Cloud-Radiation Interaction in Numerical Modeling, ECMWF, Reading, England, 135-162.
- Gordon, C.T., R.D. Hovaneć and W.F. Stern, 1984: Analysis of monthly mean cloudiness and their influence upon model diagnosed radiative fluxes. J. Geophys. Res., **89**, 4713-4738.
- Griffin, M.K., 1987: The role of clouds in surface radiation budgets. Ph.D. Dissertation, 326 pp., University of Utah, Salt Lake City.
- Hallett, J., 1965: Field and laboratory observations of ice crystal growth from the vapor. J. Atmos. Sci., **22**, 64-69.
- Hansen, J., G. Russell, D. Rind, P. Stone, A. Lacis, S. Lebedeff, R. Ruedy and L. Travis, 1983: Efficient three-dimensional global models for climate studies: Models I and II. Mon. Wea. Rev., **111**, 609-662.

Hartmann, D.L., and D.A. Short, 1980: On the use of earth radiation budget statistics for studies of clouds and climate. J. Atmos. Sci., 37, 1233-1250.

Henderson-Sellers, A., 1986: Layered cloud amounts for January and July, 1979 from 3-D Nephanalysis. J. Clim. Appl. Meteor., 25, 118-132.

Heymsfield, A.J., 1972: Ice crystal terminal velocities. J. Atmos. Sci., 29, 1348-1357.

Heymsfield, A.J., 1975a: Cirrus uncinus generating cells and the evolution of cirriform clouds. Part I: Aircraft observations of the growth of the ice phase. J. Atmos. Sci., 32, 798-808.

Heymsfield, A.J., 1975b: Cirrus uncinus generating cells and the evolution of cirriform clouds. Part II: The structure and circulations of the cirrus uncinus generating head. J. Atmos. Sci., 32, 809-819.

Heymsfield, A.J., 1975c: Cirrus uncinus generating cells and the evolution of cirriform clouds. Part III: Numerical computations of the growth of the ice phase. J. Atmos. Sci., 32, 820-830.

Heymsfield, A.J., 1977: Precipitation development in stratiform ice clouds: A microphysical and dynamical study. J. Atmos. Sci., 34, 367-381.

Heymsfield, A.J. and C.M.R. Platt, 1984: A parameterization of the particle size spectrum of ice clouds in terms of the ambient temperature and the ice water content. J. Atmos. Sci., 41, 846-856.

Hughes, N.A., 1984: Global cloud climatologies: A historical review. J. Clim. Appl. Meteor., 23, 724-751.

Heymsfield, A.J. and L.J. Donner, 1990: A scheme for parameterizing ice-cloud water content in general circulation models. J. Atmos. Sci., 47, 1865-1877.

Jacobowitz, H., L.L. Stowe, and J.R. Hickey, 1978: The Earth Radiation Budget (ERB) experiment, the Nimbus 7 user's guide, pp. 33-69. NASA Goddard Space Flight Center, Greenbelt, MD.

Jacobowitz, H., R.J. Tighe, and the Nimbus 7 ERB Experiment Team, 1984a: The earth radiation budget derived from the Nimbus 7 ERB experiment. J. Geophys. Res., 89, 4997-5010.

Jacobowitz, H., H.V. Soule, H.L. Kyle, F.B. House, and the Nimbus 7 ERB Experiment Team, 1984b: The earth radiation budget (ERB) experiment: An overview. J. Geophys. Res., 89, 5021-5038.

Jaeger, L., 1983: Monthly and areal patterns of mean global precipitation. In Variations in the global water budget, 129-140. A. Street-Perrott *et al.* (eds.), D. Reidel Publishing Company.

Kasahara, A., 1974: Various vertical coordinate systems used for numerical weather prediction. Mon. Wea. Rev., **102**, 509-522.

Kessler, E., 1969: On the distribution and continuity of water substance in atmospheric circulation. Meteor. Mongtr., No. 10, Amer. Meteor. Soc., 84 pp.

Koenig, J., and K.N. Liou, 1983: Cloud climatology and radiative budget studies from Air Force 3DNEPH data base. Preprint, The Fifth Conference on Atmospheric Radiation, Baltimore, Amer. Meteor. Soc.

Koenig, G.G., 1985: Cloud and radiation budget studies. Ph.D. Dissertation, 308 pp., University of Utah, Salt Lake City.

Koenig, G., K.N. Liou and M. Griffin, 1987: An investigation of cloud/radiation interactions using three-dimensional nephelanalysis and earth radiation budget data bases. J. Geophys. Res., **92**, 5540-5554.

Koenig, L.R., 1971: Numerical modeling of ice deposition. J. Atmos. Sci., **28**, 226-237.

Koenig, L.R. and F. Murray, 1976: Ice-bearing cumulus cloud evolution: Numerical simulation and general comparison against observations. J. Appl. Meteor., **15**, 747-762.

Krueger, S.K., K.M. Xu, and A. Arakawa, 1989 : Using a numerical cumulus ensemble model as a tool for studying cloud processes. Symposium on the Role of Clouds in Atmospheric Chmistry and Global Climate.

Kyle, H.L., P.E. Ardanuy and E.J. Hurley, 1985: The status of the Nimbus 7 Earth-Radiation-Budget data set. Bull. Amer. Meteor. Soc., **66**, 1378-1388.

Kyle, H.L., K.L. Vasanth, and the Nimbus 7 ERB Experiment Team, 1986: Some characteristic differences in the earth's radiation budget over land and ocean derived from the Nimbus 7 ERB experiment. J. Clim. Appl. Meteor., **25**, 958-981.

Kyle, H.L., R.R. Hucek, B. Groveman, and R. Frey, 1990: User's guide Nimbus 7 ERB narrow field of view: Earth radiation budget products.

Lee, J.L., S.C. Ou, and K.N. Liou, 1990: The effects of ice processes and infrared cooling on the formation of high clouds in a 3-D global cloud model. Preprint, The Seventh Atmospheric Radiation Conference, San Francisco, July 23-27.

Liou, K.N., and G.D. Wittman, 1979: Parameterization of the radiative properties of clouds. J. Atmos. Sci., **36**, 1261-1273.

Liou, K.N. and S.C. Ou, 1981: Parameterization of infrared radiative transfer in cloudy atmospheres. J. Atmos. Sci., **38**, 2707-2716.

Liou, K.N., S.C. Ou, S. Kinne and G. Koenig, 1984: Radiation parameterization programs for use in general circulation models. Scientific Report, Air Force Geophysics Laboratory, AFGL-TR-84-0217, 53 pp.

Liou, K.N., and Q. Zheng, 1984: A numerical experiment on the interactions of radiation, clouds and dynamic processes in a general circulation model. J. Atmos. Sci., 41, 1513-1535.

Liou, K.N., 1986: Influence of cirrus clouds on weather and climate processes: A global perspective. Mon. Wea. Rev., 114, 1167-1199.

Liou, K.N., J.L. Lee, S.C. Ou, Q. Fu and Y. Takano, 1990: Cloud microphysics, radiative transfer and large-scale cloud processes. Preprint, The Seventh Atmospheric Radiation Conference, San Francisco, July 23-27.

London, J., 1957: A study of the atmospheric heat balance. AFCRC-TR-57-287, College of Engineering, New York University, N.Y.

Marshall, J.S., and W.M. Palmer, 1948: The distribution of raindrops with size. J. Meteorol., 5, 165-166.

Mason, B.J., and A.P. van der Heuvel, 1959: The properties and behavior of some artificial ice nuclei. Proc. Phys. Soc. London, 74, 744-755.

Mason, B.J., 1971: The physics of clouds. 2nd Edition, Clarendon Press, 671 pp.

Mitchell, B., 1989: Analysis of global radiation budgets and cloud forcing using 3DNEPH cloud data bases. M.S. Thesis, 105 pp., University of Utah, Salt Lake City.

Mitchell, J.F.B., C.A. Senior and W.J. Ingram, 1989: CO_2 and climate: A missing feedback ? Nature, 341, 132-134.

Ohring, G., and P.F. Clapp, 1980: The effect of changes in cloud amount on the net radiation at the top of the atmosphere. J. Atmos. Sci., 37, 447-454.

Ohring, G., P.F. Clapp, T.R. Heddinghaus, and A.F. Krueger, 1981: The quasi-global distribution of the sensitivity of the earth-atmosphere radiation budget to clouds. J. Atmos. Sci., 38, 2539-2541.

Ou, S.C. and K.N. Liou, 1983: Parameterization of carbon dioxide $15\ \mu m$ absorption and emission. J. Geophys. Res., 88, 5203-5207.

Ou, S.C. and K.N. Liou, 1988: Development of radiation and cloud parameterization programs for AFGL global models. Scientific Report, Air Force Geophysics Laboratory, AFGL-TR-88-0018, 88 pp.

- Prabhakara, C., I. Wang, A.T.C. Chang, and P. Gloersen, 1983: A statistical examination of Nimbus 7 SMMR data and remote sensing of sea surface temperature, liquid water content in the atmosphere and surface wind speed. J. Clim. Appl. Meteor., 22, 2023-2037.
- Prabhakara, C. and Short, D.A., 1984: Nimbus-7 SMMR derived seasonal variations in the water vapor, liquid water and surface winds over the global oceans. NASA Technical Memorandum 86080, Goddard Space Flight Center, Greenbelt, Maryland, U.S.A.
- Ramanathan, V., E.J. Pitcher, R.C. Malone and M.L. Blackmon, 1983: The response of a spectral general circulation model to refinements in radiative processes. J. Atmos. Sci., 40, 605-630.
- Ramanathan, V., R.D. Cess, E.F. Harrison, P. Minnis, B.R. Barkstrom, E. Ahmad, and D. Hartmann, 1989 : Cloud-radiative forcing and climate: Results from the earth radiation budget experiment. Science, 243, 57-63.
- Roads, J.O., 1978: Numerical experiments on the sensitivity of an atmospheric hydrologic cycle to the equilibrium temperature. J. Atmos. Sci., 35, 753-773.
- Roeckner, E., 1988 : Cloud-radiation feedbacks in a climate model. Atmos. Res., 21, 293-303.
- Rogers, R.R., 1979: A Short Course in Cloud Physics. Pergamon Press, Oxford, 235 pp.
- Schneider, S.H., W.M. Washington and R.M. Chervin, 1978: Cloudiness as a climate feedback mechanism: Effects on cloud amounts of prescribed global and regional surface temperature changes in the NCAR GCM. J. Atmos. Sci., 35, 2207-2221.
- Shukla, J., and Y. Sud, 1981: Effect of cloud-radiation feedback on the climate of a general circulation model. J. Atmos. Sci., 38, 2337-2353.
- Slingo, J.M., 1980: A cloud parameterization scheme derived from GATE data for use with a numerical model. Quart. J. Roy. Meteor. Soc., 106, 747-770.
- Slingo, J.M. , 1987: The development and verification of a cloud prediction scheme for the ECMWF model. ibid., 113, 899-927.
- Slingo, A., and J.M. Slingo, 1988: The response of a general circulation model to cloud longwave radiative forcing, I: Introduction and initial experiments. Quart. J. Roy. Meteor. Soc., 114, 1027-1062.
- Smagorinsky, J., 1960: On the dynamical prediction of large-scale condensation by numerical methods. Monograph No. 5, Amer. Geophys. Union, 71-78.

Smagorinsky, J. , 1978 : Modeling and predictability. Studies in geophysics: Energy and climate, Nat. Acad. Sci., Washington, DC, 133-139.

Smith, R.N.B., 1990: A scheme for predicting layer clouds and their water content in a general circulation model. Quart. J. Roy. Meteor. Soc., 116, 435-460.

Smolarkiewicz, P.K., 1983: A simple positive definite advection scheme with small implicit diffusion. Mon. Wea. Rev., 111, 479-486.

Smolarkiewicz, P.K., 1984: A fully multidimensional positive definite advection transport algorithm with small implicit diffusion. J. Comput. Phys., 54, 325-362.

Somerville, R.C.J., and L.A. Remer, 1984: Cloud optical thickness feedbacks in the CO_2 climate problem. J. Geophys. Res., 89, 9668-9672.

Starr, D.O., and S.K. Cox, 1985a: Cirrus clouds. Part I: A cirrus cloud model. J. Atmos. Sci., 42, 2663-2681.

Starr, D.O., and S.K. Cox, 1985b: Cirrus clouds. Part II: Numerical experiments on the formation and maintenance of cirrus. J. Atmos. Sci., 42, 2682-2694.

Stephens, G.L., 1978: Radiative properties of extended water clouds. Parts I and II. J. Atmos. Sci., 35, 2111-2132.

Sundqvist, H., 1978: A parameterization scheme for non-convective condensation including prediction of cloud water content. Quart. J. Roy. Meteor. Soc., 104, 677-690.

Sundqvist, H., 1981: Prediction of stratiform clouds: Results from a 5-day forecast with a global model. Tellus, 33, 242-253.

Sundqvist, H., 1988 : Parameterization of condensation and associated clouds in models for weather prediction and general circulation simulation. In Physically based modelling and simulation of climate and climatic change, M.E. Schlesinger (ed.), Reidel, Dordrecht, Part 1, 433-461.

Washington, W.M., and D.L. Williamson, 1977: A description of the NCAR global circulation models, in Methods in Computational Physics, vol. 17, General Circulation Models of the Atmosphere, edited by J. Chang, pp. 111-172, Academic, New York.

Washington, W.M., and G.A. Meehl, 1984: Seasonal cycle experiment on the climate sensitivity due to a doubling of CO_2 with an atmospheric general circulation model coupled to a simple mixed-layer ocean model. J. Geophys. Res., 89, 9475-9503.

Wetherald, R.T., and S. Manabe, 1980: Cloud cover and climate sensitivity. J. Atmos. Sci., 37, 1485-1510.

Wetherald, R.T., and S. Manabe, 1986: An investigation of cloud cover change in response to thermal forcing. Clim. Change., 8, 5-23.

Wetherald, R.T., and S. Manabe, 1988: Cloud feedback processes in a general circulation model. J. Atmos. Sci., 45, 1397-1415.

Zheng, Q., and K.N. Liou, 1986: Dynamical and thermodynamic influences of the Tibetan Plateau on the atmosphere in a general circulation model. J. Atmos. Sci., 43, 1340-1354.